ACOUSTIC AND ELASTIC WAVES IN METAMATERIALS FOR UNDERWATER APPLICATIONS

by

ALEXEY S. TITOVICH

A dissertation submitted to the

Graduate School—New Brunswick

Rutgers, The State University of New Jersey

In partial fulfillment of the requirements

For the degree of

Doctor of Philosophy

Graduate Program in Mecahnical and Aerospace Engineering

Written under the direction of

Professor Andrew N. Norris

And approved by

_____

_____

_____

_____

New Brunswick, New Jersey

MAY, 2015

ABSTRACT OF THE DISSERTATION

Acoustic and Elastic Waves in Metamaterials for Underwater Applications

by **ALEXEY S. TITOVICH**

Dissertation Director:

Professor Andrew N. Norris

Elastic effects in acoustic metamaterials are investigated. Water-based periodic arrays of elastic scatterers, sonic crystals, suffer from low transmission due to the impedance and index mismatch of typical engineering materials with water. A new type of acoustic metamaterial element is proposed that can be tuned to match the acoustic properties of water in the quasi-static regime. The element comprises a hollow elastic cylindrical shell fitted with an optimized internal substructure consisting of a central mass supported by an axisymmetric distribution of elastic stiffeners, which dictate the shell's effective bulk modulus and density. The derived closed form scattering solution for this system shows that the subsonic flexural waves excited in the shell by the attachment of stiffeners are suppressed by including a sufficiently large number of such stiffeners. As an example of refraction-based wave steering, a cylindrical-to-plane wave lens is designed by varying the bulk modulus in the array according to the conformal mapping of a unit circle to a square.

Elastic shells provide rich scattering properties, mainly due to their ability to support highly dispersive flexural waves. Analysis of flexural-borne waves on a pair of shells yields an analytical expression for the width of a flexural resonance, which is then used

with the theory of multiple scattering to accurately predict the splitting of the resonance frequency. This analysis leads to the discovery of the *acoustic Poisson-like effect* in a periodic wave medium. This effect redirects an incident acoustic wave by 90° in an otherwise acoustically transparent sonic crystal. An unresponsive "deaf" antisymmetric mode locked to band gap boundaries is unlocked by matching Bragg scattering with a quadrupole flexural resonance of the shell. The dynamic effect causes normal unidirectional wave motion to strongly couple to perpendicular motion, analogous to the quasi-static Poisson effect in solids. The Poisson-like effect is demonstrated using the first flexural resonance of an acrylic shell. This represent a new type of material which cannot be accurately described as an effective acoustic medium. The study concludes with an analysis of a non-zero shear modulus in a pentamode cloak via the two-scale method with the shear modulus as the perturbation parameter.

Acknowledgements

My path towards earning my Ph.D. at Rutgers University has been a collection of experiences which came together perfectly to make me the scholar I am today. It would not be possible without numerous wonderful people who have helped me along the way. First and foremost, I would like to thank my advisor, Dr. Andrew Norris for his motivation, guidance and support. I would also like to thank my Navy mentor, Dr. Stephen O'Regan, for hosting and advising me at the Naval Surface Warfare Center Carderock Division and most importantly for promoting acoustic metamaterials for defence. This project would not be funded without the generous support of Dr. Maria Medieros of ONR code 333 via the Naval Undersea Research Program. Also, I am thankful to my Dissertation committee members, Dr. William Bottega and Dr. Lipping Liu, for reviewing this manuscript, which I admit at times is dry but ultimately satisfying.

Naturally, without the endless support of my family none of this would be possible. My parents, Sergey and Natalia, have raised my brother and I in a household where education was the number one priority. Now, after many years have passed, it is clear to me that what started then lead to me earning a Doctorate. It is now a dream of my wife, Galina, and I to be able to provide the same learning environment for our son, Alex. I am eternally grateful to her for the love and happiness we share. My brother Alexander and his wife Oksana also deserve to be mentioned for their support of my intellectual endeavours. In addition, my grandmother Vasilisa played an important role in shaping me into the person I have become. But, it was my grandfather, Michael, who was certainly the most outspoken and proud grandfather of me as a Ph.D. student, although, he did not live long enough to see me graduate.

Many other friends and colleagues deserve an acknowledgement. The fellow students

in our research group at Rutgers, Adam Nagy, Feruza Amirkulova, and Xiaoshi Su have always been available to lend a helping hand in time of need. Eugene Spikaloff is a great friend and always there when I need his help. I have also had the please of spending a summer as an intern at the Schlumberger-Doll Research center. It was a unique experience for which I thank Dr. Bikash Sinha and Dr. Ting Lei. Also, I want to thank all of the people that make the Physical Acoustics Summer School possible. To this day I meet students from our PASS class, now doctors and professors, who all agree what a worthwhile experience PASS was. I would also like to thank Alfonso Climente from the University of Valencia in Spain, who spent a summer at Rutgers and shared with us his knowledge of sonic crystals.

Thank you, and everyone not mentioned for you help.

Dedication

To my parents Sergey and Natalia,

my wife Galina and our son Alex.

Table of Contents

List of Tables

List of Figures

List of Abbreviations

$[\mathcal{L}]$	Differential operator on the displacement vector of the shell
α	Parameter relating the mass of the shell to that of the displaced fluid
$\bar{\mu}$	Scaled shear modulus
β	Small bending parameter
$\mathbf{T}$	T-matrix relating incident and scattered fields
$\boldsymbol{I}$	Intensity vector
$\boldsymbol{n}$	Normal vector
$\boldsymbol{\sigma}$	Stress tensor
$\boldsymbol{\varepsilon}$	Strain tensor
$\boldsymbol{C}$	Elasticity tensor
$\boldsymbol{F}$	Deformation gradient
$\boldsymbol{R}$	Rotation tensor
$\boldsymbol{V}$	Left stretch tensor
δ	Dirac delta function
δ_{ij}	Kronecker delta
ϵ	Infinitesimal factor
ϵ_n	Half-width of the n^{th} flexural resonance
ϵ_{ij}	Components of the strain tensor
ΓM	[1,1] direction in a square unit cell.
ΓX	[1,0] direction in a square unit cell.
$\Gamma(n)$	Gamma function of n
$\hat{\rho}$	Contribution to the effective density by the central rod
$\hat{K}$	Stiffness of a rib relative to the elastic modulus of the material
$\hat{k}$	Reduced wave vector
κ	Stiffness of an individual spring

Λ	Determinant of the deformation gradient, dilitation
λ	Wavelength
λ_j	Eigenvalues
μ	Shear modulus
μ_s	Shear modulus of the shell
ν_s	Poisson ratio of the shell
Ω	Non-dimensional frequency normalized by the shell properties
ω	Angular frequency
Ω_1	Radial resonance frequency of the fluid-loaded shell
Ω_2	Circumferential resonance frequency of the fluid-loaded shell
Ω_c	Non-dimensional circumferential resonance frequency
Ω_r	Non-dimensional radial resonance frequency
Ω_{res}	Asymptotic resonance frequency of the shell-spring-mass system in water
ω_{sp}	Resonance frequency of the springs-mass system
ϕ	Curl-free potential of the displacement field
Φ_1	Shift of the flexural resonance frequency for two nearby shells
ϕ_n	Argument of ζ_n
ψ	Divergence-free potential of the displacement field
ρ	Density of water
ρ'	Mapped density distribution
ρ_0	Density of an elastic material in the pentamode limit
ρ_m	Contribution to the effective density by the added mass m
ρ_s	Density of the shell
ρ_{eff}	Effective density of the shell
ρ_{eq}	Equivalent density of the unit cell
σ	Normal stress on a shell
σ_n	Modal normal stress on a shell
σ_{hoop}	Hoop stress
σ_{ij}	Components of the stress tensor

σ_{tot}	Total scattering cross section
τ	Non-dimensional frequency ratio
θ	Azimuthal coordinate
θ_j	Position of the j^{th} spring
ε	Perturbation parameter
ε_{hoop}	Hoop strain
$\widehat{Z}_n$	Modal acoustic impedance for regular wave functions
ξ	Fast scale
ζ_n	Scaled sum of impedances
A	Area
a	Outer radius of the shell
A_n	Modal amplitudes of the incident wave
b	Side length of the square unit cell
B_n	Modal amplitudes of the scattered wave
b_n	Components of the vector $\mathbf{b}_j$
$B_n^{(0)}$	Components of the vector $\mathbf{B}^{(0)}$
$B_n^{(1)}$	Components of the vector $\mathbf{B}^{(1)}$
c	Sound speed of water
C_{ijkl}^{PM}	Components of the elasticity tensor for a pentamode material
c_L	Longitudinal wave speed
c_p	Extensional wave speed
c_T	Transverse wave speed
c_{eff}	Effective sound speed of the shell
C_{ijkl}	Components of the elasticity tensor
C_{ij}	Components of the elasticity matrix in Voigt notation
C_i^0	Eigenvalues of the elasticity matrix in Voigt notation
d_{1-4}	Components of the coefficient matrix in the equation of motion
E	Energy
E_s	Young's modulus of the shell

F	Total spring force
f	Frequency
$F(\Omega)$	Characteristic equation from shell theory
$f(\theta)$	Net force on the shell due to the springs-mass system
f_n	Modal force on the shell due to the springs-mass system
f_s	Filling fraction of the shell in a square unit cell of water
F_{ij}	Components of the deformation gradient
g	Far-field form function
$g^{(0)}$	Form function for empty shell
$g^{(1)}$	Addition to the form function due to the springs-mass system
g_n	Modal far-field form function
h	Thickness of the shell
H_J	Multiplicative factor for J springs
$H_n^{(1)}$	Hankel function of the first kind of order n
J	Number of springs/stiffeners
J_n	Bessel function of the first kind of order n
K	Bulk modulus of water
k	Wavenumber
K'	Mapped bulk modulus distribution
K_0	Bulk modulus of an elastic material in the pentamode limit
k_n	Normal component of the wave vector
k_t	Tangential component of the wave vector
K_{eff}	Effective bulk modulus of the shell
k_{eff}	Effective spring stiffness
K_{eff}^{thin}	Effective bulk modulus of the shell via thin shell theory
K_{eq}	Equivalent bulk modulus of the unit cell
K_{ps}	Plane strain bulk modulus
k_{res}	Asymptotic resonance wavenumber of the shell-spring-mass system in water
K_{sh}	Bulk modulus factor for a thin shell

K_{sp}	Contribution to the effective bulk modulus by the springs-mass system
k_{sp}	Resonance wavenumber of the springs-mass system
m	Added internal mass
n	Modal index
p	Total pressure
p_0	External pressure
p_i	Incident pressure
P_n	Modal total pressure
p_s	Scattered pressure
Q	Quality factor
R	Reflection coefficient
r	Radial coordinate
$r_{1,2}$	Radii of central rods in ribs-rod model
S_n	Diagonal elements of the S-matrix
T	Transmission coefficient
t	Thickness of the lengthwise ribs
T_{side}	Transmission coefficient from the sides of the lens
T_n	Components of the T-matrix
u	Axial displacement
V	Volume occupied by the shell
v	Azimuthal displacement
V_n	Azimuthal modal displacement
w	Radial displacement
W_n	Radial modal displacement
$w_n^{(J)}$	J-cyclical summation of modal amplitudes W_n
X	Slow scale
x'	Gradient of properties in a pentamode cloak
Z	Impedance of water
z	Axial coordinate

Z_n^{sp}	Modal impedance of the springs-mass system
Z_n	Modal acoustic impedance
Z_n^{sh}	Modal impedance of the shell
Z_n^{tot}	Modal equivalent impedance of the shell-springs-mass system in water
Z_{eff}	Effective impedance of the shell
$\mathbf{B}^{(0)}$	Scattered field modal amplitudes for the empty shell
$\mathbf{B}^{(1)}$	Addition to the scattered field modal amplitudes by the springs-mass system
$\mathbf{b}_j$	Infinite vector representing the contribution of the springs-mass system to T-matrix of the shell
$\mathbf{e}_j$	Eigenvectors
$\mathbf{T}^{(0)}$	Diagonal T-matrix for the empty shell
AS	Antisymmetric modes/bands
BG	Band gap
BZ	Irreducible Brillouin zone
D-M	Donnel-Mushtari thin shell theory
F-B-L	Flügge-Byrne-Lur'ye thin shell theory
FEM	Finite element simulation
IPI	In-plane inertia
L-T	Love-Timoshenko thin shell theory
NZIM	Near-zero-index materials
PC	Phononic crystal
PM	Pentamode
S	Symmetric modes/bands
SC	Sonic crystal
TSCS	Total scattering cross section

Chapter 1

Introduction to acoustic metamaterials

1.1 Acoustic metamaterials background

Metamaterials are man-made macroscopic composites with optimized periodic structure, designed to have properties not found in nature. The unit cell, or the fundamental element, dictates the response of the bulk material through it properties. These properties can either be static or dynamic and might be affected by the surrounding cells within an array which can further complicate the analysis. In acoustic metamaterials, the effective density ρ and bulk modulus K (or alternatively, the sound speed $c^2 = K/\rho$ and impedance $Z = \rho c$) of the unit cell are the design parameters. By masterfully tailoring these properties, such metamaterials exhibit extraordinary effects such as cloaking, negative refraction, hyper-lensing, negative or zero mass/stiffness. Hiding an object from acoustic detection is a particularly interesting topic and consequently the field has exploded in the last decade. As a result, the literature has seen an upsurge of new ideas for acoustic metamaterials.

The review article by Hussein et al. [42] presents a thorough history of acoustic metamaterials. They describe how the field grew from layered composites, to embedded spheres, to sonic crystals, to perforated plates, which then lead to defect engineering in crystals. Based on the physics, acoustic metamaterials can be categorized into three fundamental groups: sonic crystals, phononic crystals, and active metamaterials. The characteristics of each type of acoustic metamaterials is described next.

Sonic crystals (SCs) are the primary topic of this Dissertation. These are periodic arrays of scatterers (inclusions) in an acoustic medium. A wave incident onto such an array can either be transmitted through, reflected back, refractively steered or even redirected to a perpendicular direction. For this material, the fundamental element

is the scatterer which can be rigid, fluid or elastic. If the scatterers are rigid, the the scattering properties are dictated by their filling fraction and distribution. Such SCs typically have low transmission, because of the impedance mismatch with the surrounding fluid. Sometimes it is desirable to filter out certain frequencies. This can be done via Bragg scattering, by tuning the lattice spacing to coincide with the wavelength. A different example is magnifying hyper lensing, which has been demonstrated by a rigid one dimensional radial SC with a central dual-source. Another example is an effectively anisotropic medium made from perforated plates, which can take on extraordinary effective acoustic properties such as full transmission at certain angles of incidence. SC based on rigid inclusion are governed by the constructive and destructive interference of scattered waves only. On the other hand, if the fundamental element in the SC is elastic, the elasticity plays a dominant role. The unit cell can be homogenized in the long wavelength limit yielding effective acoustic properties. Moreover, by introducing a gradient of acoustic properties, a SC is capable of "steering" an incident wave. Such SCs are refereed to as gradient index materials. One can appreciate the difference from classical optics where the shape of the lens is key and not a distribution of the refractive index. In this work, an elastic shell is selected as the scatter. Phononic crystals (PCs) differ from SCs in that the scatterers as well as the matrix are elastic (although this distinction between PCs and SCs is not universally adopted). Consequently, a PC can support propagating shear waves. It is nearly impossible to match the acoustic properties of water with an elastic material without introducing voids. One example of such a cellular material is an elastic foam. It has been demonstrated that an aluminum foam slab can be nearly acoustically transparent. That same slab also exhibits negative refraction at higher frequencies. The downside is the drop in transmission due to the ever-present shear waves. It should be noted that the lack of shear waves in SCs is a most useful attribute. It is also possible to control the response of PCs and SCs actively, which is a field in its own right.

1.2 Outline of Dissertation accomplishments

This Dissertation is outlined as follows. Elasticity in SCs and PCs is the dominant topic of this Dissertation. Chapter 2 introduces the elastic shell as an effective acoustic medium. The axisymmetric substructure used to tune the shells is also described and analyzed. Chapter 3 solves the problem of acoustic scattering from such shells. Chapter 4 describes methods for using tuned shells to design refraction-based acoustic lenses. A closer look at the interference of flexural-borne waves on neighbouring shells is presented in Chapter 5. These results are then used to design a new type of effective medium based on the quadrupolar resonance of a shell in Chapter 6. Chapter 7 presents a solution of the equations of elasticity with a perturbation in shear. This result is used to show the effect of shear in a pentamode-type acoustic cloak. In this Dissertation the term **shell** will be used throughout to describe hollow cylinders which are can also be referred to as tubes or pipes in other contexts.

Several noteworthy accomplishments of this work follow. A sub-wavelength acoustically transparent cylinder has been designed. The elegant problem of acoustic scattering from an elastic shell with axisymmetrically distributed springs has been solved in closed form. A high transmission acoustic lens has been created from an array of elastic shells which demonstrates wave steering. Analytical expressions for the bandwidth of a flexural resonance and the frequency splitting of two nearby shells have been derived. A novel method for redirecting an incident acoustic wave to a normal direction has been discovered. It is referred to as the acoustic Poisson-like effect due to its similarities with the elastodynamic Poisson effect.

Chapter 2

Elastic shell as an effective acoustic medium

A solid elastic cylinder typically cannot be acoustically transparent in the quasi-static regime. That is to say the there are no elastic materials that can simultaneously and exactly match the density and bulk modulus of water. This is because most engineering materials are too stiff and dense. A solution is to introduce a central void to decrease the effective properties. The result is an elastic hollow cylinder or a shell. Of particular interest is an elastic cylindrical shell with a circular cross section because it is axisymmetric. The shell's thickness becomes a design parameter which dictates the response of the shell. Perhaps it is hard to believe at this point, but even a metal shell can behave acoustically as water through an appropriate choice of this parameter. This Chapter will derive and analyze the effective quasi-static properties of empty shells as well as shells with an internal substructure.

2.1 Empty elastic shell

In this section, the effective quasi-static acoustic properties of an empty elastic shell will be determined. Consider an infinitely long elastic shell of outer radius a and

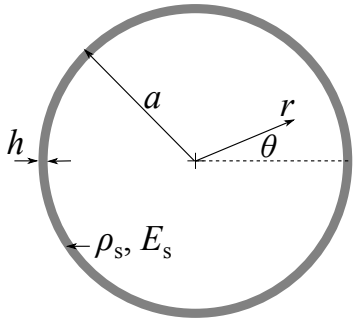

Figure 2.1: Empty elastic shell of outer radius a and thickness h.

thickness h as pictured in Figure 2.1. The density, elastic modulus, and Poisson's ratio are (ρ_s, E_s, ν_s), respectively. The displacement variables are (w, v, u) in the (r, θ, z) cylindrical coordinate system. To obtain the plane strain bulk modulus of the shell, the problem of hydrostatic compression must be solved. Two assumptions are made in the present analysis: i) the loading is axisymmetric (hydrostatic), thus there is no variation with azimuth yielding $v = 0$, $\frac{\partial()}{\partial\theta} = 0$ and ii) the cylinder undergoes plane strain which implies $(\varepsilon_{zz}, u) = 0$. There is no shear stress within the shell since the loading is axisymmetric. The general strain-displacement relations simplify to

$$\varepsilon_{rr} = \frac{\partial w}{\partial r} \qquad \rightarrow \qquad \frac{dw}{dr}, \tag{2.1a}$$

$$\varepsilon_{\theta\theta} = \frac{1}{r}\left(\frac{\partial v}{\partial \theta} + \frac{w}{r}\right) \qquad \rightarrow \qquad \frac{w}{r}, \tag{2.1b}$$

$$\varepsilon_{r\theta} = \frac{1}{2}\left(\frac{1}{r}\frac{\partial w}{\partial \theta} + \frac{\partial v}{\partial r} - \frac{v}{r}\right) \qquad \rightarrow \qquad 0. \tag{2.1c}$$

From Hooke's Law, the hybrid constitutive relations for plane strain are

$$\sigma_{rr} = \frac{E_s}{1-\nu_s^2}(\varepsilon_{rr} + \nu_s \varepsilon_{\theta\theta}) + \frac{\nu_s}{1-\nu_s}\sigma_{zz}, \tag{2.2a}$$

$$\sigma_{\theta\theta} = \frac{E}{1-\nu_s^2}(\varepsilon_{\theta\theta} + \nu_s \varepsilon_{rr}) + \frac{\nu_s}{1-\nu_s}\sigma_{zz}, \tag{2.2b}$$

$$\sigma_{zz} = \nu_s(\sigma_{rr} + \sigma_{\theta\theta}), \tag{2.2c}$$

where σ_{ij} are the stress tensor components. For plane strain, the longitudinal stress σ_{zz} is assumed to be constant. The equation of static equilibrium in the radial direction is

$$\frac{d\sigma_{rr}}{dr} + \frac{\sigma_{rr} + \sigma_{\theta\theta}}{r} = 0. \tag{2.3}$$

The θ-equation of motion is identically satisfied by virtue of the stated assumptions. Substituting equations (2.1) into (2.2) and then into (2.3) yields $r^2 w'' + r w' + w = 0$ after rearranging. This homogeneous Euler's equation has two independent solutions [97]

$$w(r) = \frac{C_0}{r} + C_1 r, \tag{2.4}$$

where C_0 and C_1 are integration constants to be determined by applying boundary conditions. To do so the strains are expressed in terms of these constants as

$$\varepsilon_{rr} = -\frac{C_0}{r^2} + C_1, \qquad \varepsilon_{\theta\theta} = \frac{C_0}{r^2} + C_1. \tag{2.5}$$

Substituting (2.5) into (2.2) yields

$$\sigma_{rr} = \frac{E_s}{1-\nu_s^2}\left(-\frac{(1-\nu_s)}{r^2}C_0 + (1+\nu_s)C_1\right) + \frac{\nu_s}{1-\nu_s}\sigma_{zz}, \tag{2.6a}$$

$$\sigma_{\theta\theta} = \frac{E_s}{1-\nu_s^2}\left(\frac{(1-\nu_s)}{r^2}C_0 + (1+\nu_s)C_1\right) + \frac{\nu_s}{1-\nu_s}\sigma_{zz}, \tag{2.6b}$$

$$\sigma_{zz} = \frac{2\nu_s E_s}{1-\nu_s-2\nu_s^2}C_1. \tag{2.6c}$$

Note that σ_{zz} is indeed independent of r. Eliminating σ_{zz} from σ_{rr} and $\sigma_{\theta\theta}$ in equations (2.6) and applying the boundary conditions $\sigma_{rr}(a-h)=0$ and $\sigma_{rr}(a)=-p_0$, where p_0 is the applied pressure, yields

$$C_0 = \frac{(1+\nu_s)p_0a^2}{E_s}\left(\frac{(1-(h/a))^2}{(1-(h/a))^2-1}\right), \tag{2.7a}$$

$$C_1 = \frac{(1-\nu_s-2\nu_s^2)p_0}{E_s}\left(\frac{1}{(1-(h/a))^2-1}\right). \tag{2.7b}$$

Assuming small displacement $w \ll a$, the decrease in the volume of the shell is

$$\frac{\Delta V}{V} = \frac{(a-w(a))^2-a^2}{a^2} \approx -2\frac{w(a)}{a} = -2\left(\frac{C_0}{a^2}+C_1\right). \tag{2.8}$$

The effective bulk modulus is defined as $K_{eff} = \frac{p_0}{\Delta V/V}$ and simplifies to

$$K_{eff} = \frac{E_s}{2(1+\nu_s)}\frac{(2-\frac{h}{a})\frac{h}{a}}{2(1-\nu_s)-(2-\frac{h}{a})\frac{h}{a}}. \tag{2.9}$$

In the limit as $h/a \to 1$, K_{eff} approaches the plane strain bulk modulus of the material itself, which is

$$K_{ps} = \frac{E_s}{2(1+\nu_s)(1-2\nu_s)} \tag{2.10}$$

Equation (2.9) can also be written in the following useful form

$$K_{eff} = \left(1+\frac{(1+\nu_s-\frac{h}{a})\frac{h}{a}}{2(1-\nu_s)-2\frac{h}{a}+\left(\frac{h}{a}\right)^2}\right)K_{eff}^{thin}, \tag{2.11}$$

which exposes the dependence on the effective bulk modulus for thin shells

$$K_{eff}^{thin} = \frac{E_s}{2(1-\nu_s^2)}\frac{h}{a} = \frac{\rho_s c_p^2}{2}\frac{h}{a}, \tag{2.12}$$

where $c_p = \sqrt{\frac{E_s}{\rho_s(1-\nu_s^2)}}$ is the extensional wave speed. Equation (2.12) is identical to the effective bulk modulus in equation (2.56) on page 38 of Ref. [44]. An alternative derivation of the effective bulk modulus for a thin shell can be found in Section II of

Ref. [102]. The last equality suggests that for a thin shell with $h/a \ll 1$, the bulk modulus is linear with h/a. For thicker shells, a better approximation is $K_{eff} = (1 + \frac{h}{a})K_{eff}^{thin}$. Figure 2.2 shows the normalized effective bulk modulus K_{eff}/K_{ps} of several materials versus the thickness to radius ratio h/a. Note that as $h/a \to 1$, the shell becomes a rod and K_{eff} asymptotically approaches the value of K_{ps}. For the acrylic shell in plot (b), K_{eff}^{thin} is accurate up to $h/a = 0.1$, while the expression $(1+\frac{h}{a})K_{eff}^{thin}$ more closely approximates the effective bulk modulus to about $h/a = 0.3$.

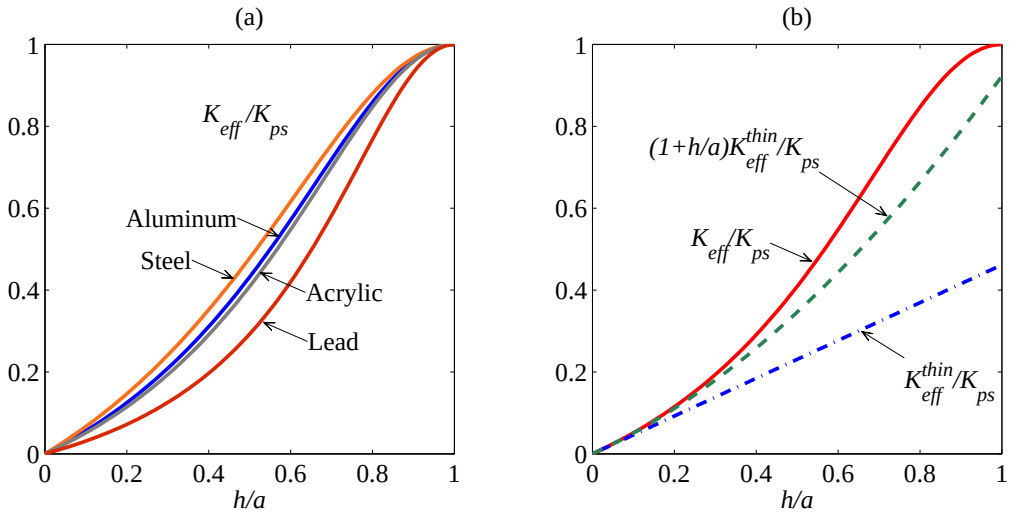

Figure 2.2: Effective bulk modulus of the shell normalized by the plane strain bulk modulus K_{eff}/K_{ps} as a function of thickness to radius ratio h/a. Plot (a) shows K_{eff}/K_{ps} for several common materials. Plot (b) presents the effective bulk modulus for an acrylic shell/rod as well as several approximate functions.

The second parameter which determines the quasi-static response of an elastic shell is the effective density. It is defined as the mass of the shell per the displaced volume.

$$\rho_{eff} = \rho_s \left(2 - \frac{h}{a}\right)\frac{h}{a}. \tag{2.13}$$

The effective bulk modulus (2.9) and density (2.13) define the compressional and inertial properties of the shell, respectively.

2.1.1 Material selection for tuning to water

Acoustic scattering from an object much smaller than the wavelength is described as quasi-static. This simply implies that the loading is gradual enough that the higher order inertial effects can be ignored. For a shell, the amount of scattering depends on its effective static properties. Thus even a metal shell can be acoustically transparent at sub-wavelength frequencies if its effective bulk modulus and density are matched to water. The bulk modulus and density of water are taken as $K = 2.25$ GPa and $\rho = 1000$ kg/m^3, respectively. From equations (2.9) and (2.13), the shell is acoustically tuned to water when the thickness to radius ratio satisfies

$$\frac{E_s}{2(1+\nu_s)}\frac{(2-\frac{h}{a})\frac{h}{a}}{2(1-\nu_s)-(2-\frac{h}{a})\frac{h}{a}} = K, \tag{2.14a}$$

$$\rho_s\Big(2-\frac{h}{a}\Big)\frac{h}{a} = \rho \tag{2.14b}$$

Solving equations (2.14) simultaneously yields a relationship between the extensional and acoustic wave speeds

$$\frac{c_p^2}{4c^2} = 1 - \frac{\rho}{2(1-\nu_s)\rho_s}, \quad \text{or} \quad \frac{4}{c_p^2} = \frac{1}{c^2} + \frac{1}{c_T^2}\frac{\rho}{\rho_s}, \tag{2.15}$$

where the longitudinal and shear speeds of the bulk material follow from Ref. [51] as

$$c_L^2 = \frac{E_s(1-\nu_s)}{\rho_s(1+\nu_s)(1-2\nu_s)}, \quad c_T^2 = \frac{\mu_s}{\rho_s}, \tag{2.16}$$

with the shear modulus $\mu_s = E_s/(2(1+\nu_s))$.

Equations (2.14) suggest that for a given shell with properties (E_s, ρ_s, ν_s), there **may** exist a thickness to radius ratio h/a which satisfies both conditions making the shell acoustically transparent in water. Figure 2.3 plots the normalized effective bulk modulus K_{eff}/K versus the normalized density ρ_{eff}/ρ as h/a is increased from 0 to 1 for several materials. The thickness increases from lower left to upper right. The maxima for each curve correspond to the normalized bulk density and plane strain bulk modulus of the material. The black circles indicate the shell thickness ratio of $h/a = 0.5$ on each curve. The dashed lines represent matched impedance $K_{eff}\rho_{eff}/(K\rho) = 1$ and matched sound speed $K_{eff}\rho/(K\rho_{eff}) = 1$. Table 2.1 shows the shell thickness for each

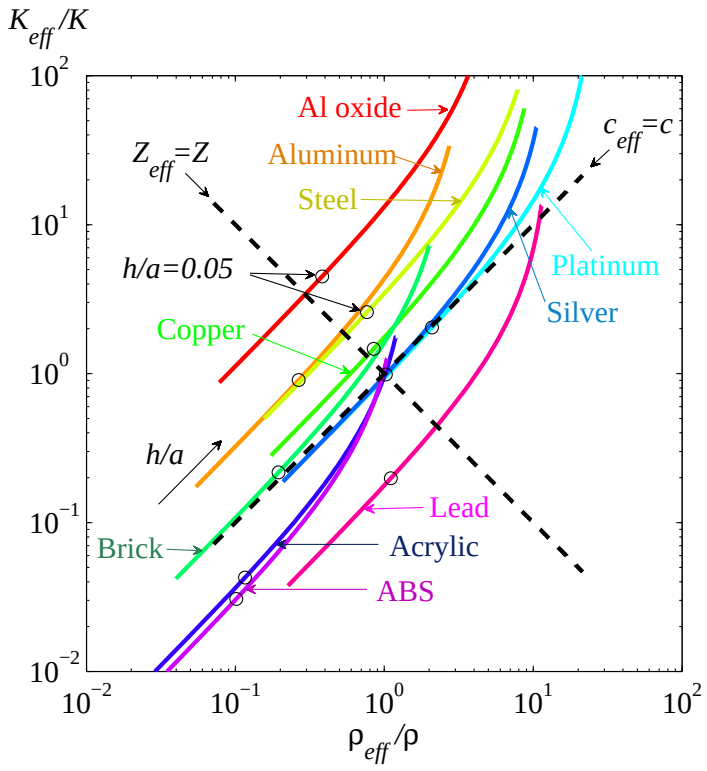

Figure 2.3: Log-log plot of K_{eff}/K versus ρ_{eff}/ρ as h/a is varied for several materials. The dashed black lines represent matched impedance and sound speed to water. The circular dots indicate the shell thickness ratio of $h/a = 0.5$. Shell thickness increases from lower left to upper right.

material when the density is matched to water $\rho_{eff}/\rho = 1$ and when the bulk modulus is matched $K_{eff}/K = 1$, which typically differ.

To have the effective acoustic properties of water, the two values of shell thickness should match. There are several exceptional materials which can accomplish this. They are summarized in the following Table 2.2. Table 2.2 also shows the extensional, longitudinal and transverse speed for each of these materials. Generally, there is no condition on sound speed for the material to be tuned to water, it is simply due to a perfect balance of inertial and stiffness properties. However, for thin shells the necessary condition is

$$c_p = 2c \qquad \Leftarrow \qquad \begin{cases} \rho_s c_p^2 h/(2a) = K \\ 2\rho_s h/a = \rho \end{cases}, \tag{2.17}$$

which is apparently satisfied for the thin platinum shell of thickness $h/a = 0.025$. Comparing equation (2.17) and (2.15) implies that the contribution of shear in thin

Material	ρ_s	E_s	ν_s	c_p	$\frac{h}{a}(\rho)$	$\frac{h}{a}(K)$
Aluminum Oxide	3920	370	0.22	9959	0.137	0.012
Molybdenum	10300	276	0.32	5463	0.050	0.015
Aluminum 3003-H18	2730	69	0.33	5326	0.204	0.055
Steel AISI 4340	7850	205	0.28	5323	0.066	0.020
Titanium beta-31S	4940	105	0.33	4884	0.107	0.037
Copper	8700	110	0.35	3796	0.060	0.035
Concrete	2300	25	0.33	3493	0.248	0.139
Brick	2000	17	0.3	3056	0.293	0.199
Platinum	21450	147	0.39	2842	0.024	0.025
Silver	10500	72.4	0.37	2827	0.049	0.051
Acrylic	1190	3.2	0.35	1751	0.600	0.615
ABS	1040	2.3	0.35	1588	0.804	0.761
Lead	11340	13.87	0.42	1215	0.045	0.204

Table 2.1: The required shell thickness ratio to match the density of water h/a ($\rho_{eff} = \rho$) and to match the bulk modulus h/a ($K_{eff} = K$) for different materials. Units of density are kg/m^3, elastic modulus GPa, speed m/s.

	h/a	c_p	c_L	c_T
Acrylic	0.62	1751	2078	998
Silver	0.51	2827	3492	1586
Platinum	0.025	2843	3697	1570

Table 2.2: Materials capable of matching the properties of water at a particular shell thickness h/a (corresponding to point $(1, 1)$ in Figure 2.3). The extensional, longitudinal and transverse speed for each material are shown.

shells is negligible. For engineering applications, materials such as silver and platinum, are not practical. As a result, other methods of tuning an elastic shell have to be developed. Later, the acoustically transparent acrylic shell of thickness $h/a = 0.62$ will be used to demonstrate the novel acoustic Poisson-like effect in Chapter 6.

2.2 Multi-layer shells

Rather than trying to find a material which will have the properties of water, a multilayer shell can be constructed instead. The simplest example is a bilayer shell as pictured in Figure 2.4. The external radius remains a and the thicknesses of the outer

and inner cylinders are h_1 and h_2, respectively. The subscripts indicate the cylinder throughout. The radial displacements and stresses in each cylinder will differ as

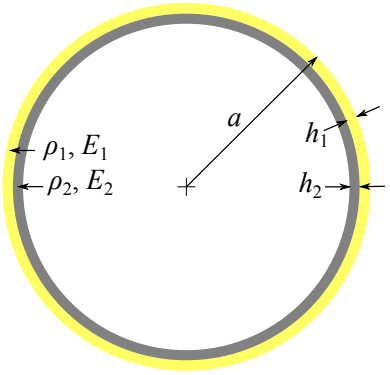

Figure 2.4: Schematic of a bilayer shell.

$$\begin{aligned} w_1 &= \frac{C_0}{r} + C_1 r, & w_2 &= \frac{D_0}{r} + D_1 r \\ \frac{1}{E_1}\sigma_1 &= -\frac{C_0}{(1+\nu_1)r^2} + \frac{C_1}{(1-\nu_1-2\nu_1^2)}, & \frac{1}{E_2}\sigma_2 &= -\frac{D_0}{(1+\nu_2)r^2} + \frac{D_1}{(1-\nu_2-2\nu_2^2)}. \end{aligned} \tag{2.18}$$

where C_0, C_1, D_0, D_1 are the constants of integration. Applying the boundary conditions yields

$$\begin{aligned} \sigma_1(a) = \frac{-p_0}{E_1} \quad &\rightarrow \quad -\frac{C_0}{(1+\nu_1)a^2} + \frac{C_1}{(1-\nu_1-2\nu_1^2)} = \frac{-p_0}{E_1}, \\ w_1(a-h_1) = w_2(a-h_1) \quad &\rightarrow \quad \frac{C_0}{(a-h_1)} + C_1(a-h_1) = \\ &\qquad \frac{D_0}{(a-h_1)} + D_1(a-h_1), \\ \sigma_1(a-h_1) = \sigma_2(a-h_1) \quad &\rightarrow \quad -\frac{C_0}{(1+\nu_1)(a-h_1)^2} + \frac{C_1}{(1-\nu_1-2\nu_1^2)} = \\ &\qquad -\frac{D_0}{(1+\nu_2)(a-h_1)^2} + \frac{D_1}{(1-\nu_2-2\nu_2^2)}, \\ \sigma_2(a-h_1-h_2) = 0 \quad &\rightarrow \quad -\frac{D_0}{(1+\nu_2)(a-h_1-h_2)^2} + \frac{D_1}{(1-\nu_2-2\nu_2^2)} = 0. \end{aligned} \tag{2.19}$$

Solving the system of equations and substituting back into the displacements (2.18) gives the effective bulk modulus

$$\begin{aligned} K_{eff} &= \frac{p_0 a}{-2w_1(a)}, \\ &= \frac{E_1}{2(1-\nu_1^2)}\frac{h_1}{a} + \frac{E_2}{2(1-\nu_2^2)}\frac{h_2}{a} \\ &+ \frac{1}{2}\left(\frac{E_1}{2(1-\nu_1^2)}\left(\frac{h_1}{a}\right)^2 + \frac{E_2}{2(1-\nu_2^2)}\left(\frac{h_2}{a}\right)^2 + \frac{E_2}{(1-\nu_2^2)}\frac{(1+\nu_1)}{(1-\nu_1)}\left(\frac{h_1}{a}\right)\left(\frac{h_2}{a}\right)\right) \\ &+ O(h_1^3, h_2^3). \end{aligned} \tag{2.20}$$

In the case of a thin shell $h \ll a$, the effective bulk modulus is

$$K_{eff} \approx \frac{E_1}{2(1-\nu_1^2)}\frac{h_1}{a} + \frac{E_2}{2(1-\nu_2^2)}\frac{h_2}{a} = \frac{\rho_1 c_1^2}{2}\frac{h_1}{a} + \frac{\rho_2 c_2^2}{2}\frac{h_2}{a}, \tag{2.21}$$

where c_1 and c_2 are the extensional wave speeds. Note that this is a parallel summation of the effective moduli of each shell. Similar to a single shell, the effective density of the bilayer shell is given by

$$\begin{aligned} \rho_{eff} &= \frac{1}{\pi a^2}\left(\rho_1\pi((a-h_2)^2 - (a-h_1-h_2)^2) + \rho_2\pi(a^2 - (a-h_2)^2)\right), \\ &\approx 2\rho_1\frac{h_1}{a} + 2\rho_2\frac{h_2}{a}, \qquad\qquad (h_1, h_2) \ll a. \end{aligned} \tag{2.22}$$

The effective bulk modulus (2.21) and density (2.22) can be solved for the thicknesses of the two shells yielding

$$\frac{h_1}{a} = \frac{\rho_{eff}}{2\rho_1}\left(\frac{(2c_{eff})^2 - c_2^2}{c_1^2 - c_2^2}\right), \tag{2.23a}$$

$$\frac{h_2}{a} = \frac{\rho_{eff}}{2\rho_2}\left(\frac{c_1^2 - (2c_{eff})^2}{c_1^2 - c_2^2}\right), \tag{2.23b}$$

where the effective wave speed is defined as $c_{eff}^2 = K_{eff}/\rho_{eff}$. Equations (2.23) presents a necessary condition on the extensional wave speeds of the shell $c_1 > 2c_{eff} > c_2$, that one shell must be faster and the other slower than twice the effective wave speed $2c_{eff}$. As an example, Table 2.3 demonstrates how an outer layer of lead can be applied to common shells tuning them to the properties of water $c_{eff} \to c$. The idea of layering materials can certainly be extended to more layers. The procedure in essence combines the mass and stiffness properties of the individual shells to create a composite with desired properties. If one is unable to coat a copper shell with lead as suggested, the shell can be tuned with an internal substructure.

Bilayer shell	h_1/a	h_2/a	c_1	c_2	c_{eff}
Lead on Aluminum 3003-H18	0.0318	0.0512	1216	5326	1500
Lead on Copper	0.0184	0.0334	1216	3796	1500
Lead on Steel AISI 4340	0.0317	0.0178	1216	5323	1500

Table 2.3: Three bilayer shells tuned to water where the outer shell is made of lead. The extensional wave speeds in each material are compared to the effective speed of the composite. Subscript $()_1$ is used for the lead shell.

2.3 Shell with an axisymmetric substructure

An internal substructure can be used to stiffen and add mass to a otherwise empty shell. Consider a substructure consisting of a central mass m attached to the shell by an axisymmetric distribution of J springs of stiffness κ as shown in Figure 2.5. A structural realization of this substructure is shown in Figure 2.7 and consist of a central rod supported by lengthwise ribs. The two parameters κ, m make the substructure an oscillator and facilitate the tuning of a shell to have stiffer and denser properties than if left empty. The aim here is to determine how the effective bulk modulus and density vary with these parameters. In doing so, it is sufficient to consider a thin shell as done in Ref. [101].

2.3.1 Springs-mass model

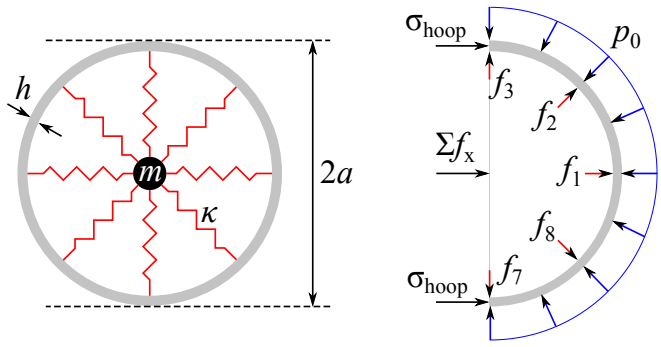

Figure 2.5: External and internal forces acting on the shell with $J = 8$ springs of stiffness κ supporting a central mass m.

Applying a hydrostatic pressure p_0 on the outside of the infinitely long cylindrical shell results in a decrease of the radius $a \to a - w(a)$. The quasi-static effective bulk

modulus is defined as $K_{eff} = -p_0/(\Delta V/V)$, where the volume change is $\frac{\Delta V}{V} = \frac{\Delta A}{A} \approx -2\frac{w(a)}{a}$ since the elastic deformation is plane strain. The radial and azimuthal strain in the shell are both approximately equal to $\varepsilon_{hoop} = \frac{w(a)}{a}$, so that the effective bulk modulus is

$$K_{eff} \approx \frac{p_0}{2\varepsilon_{hoop}}. \tag{2.24}$$

The axial stress is $\sigma_a = \nu_s \sigma_{hoop}$, and consequently the hoop strain and stress are related by $\rho_s c_p^2 = \frac{E_s}{1-\nu_s^2}$ as

$$\varepsilon_{hoop} = \frac{1}{E_s}\left(\sigma_{hoop} - \nu_s \sigma_a\right) = \frac{\sigma_{hoop}}{\rho_s c_p^2}. \tag{2.25}$$

An imaginary bisecting cut exposes the internal forces as shown in Figure 2.5. The static equilibrium condition is then

$$2h\,\sigma_{hoop} - 2a\,p_0 + F = 0, \tag{2.26}$$

where F is the horizontal resultant per unit length of the forces exerted by the springs on the half shell. At the same time, the spring forces are proportional to $w(a)$, say

$$F = k_{eff}\; w(a). \tag{2.27}$$

Equations (2.24) - (2.27) imply that

$$K_{eff} = \frac{h}{2a}\rho_s c_p^2 + \frac{k_{eff}}{4}, \tag{2.28}$$

where the effective stiffness k_{eff} remains to be determined. Hence, referring to Figure 2.5,

$$F \equiv \sum f_x = \kappa w(a) \;\times \begin{cases} \sum\limits_{j=-J/4}^{J/4} \cos\theta_j & \text{for even } J, \\ \sum\limits_{j=0}^{(J-1)/2} \sin\theta_j & \text{for odd } J. \end{cases} \tag{2.29}$$

Performing the sums and using (2.27) gives

$$k_{eff} = \kappa \times \begin{cases} \cot\left(\frac{\pi}{J}\right) & \text{for even } J, \\ \frac{1}{2}\cot\left(\frac{\pi}{2J}\right) & \text{for odd } J. \end{cases} \tag{2.30}$$

Consider even J, in which case equations (2.28) and (2.30) imply that the effective bulk modulus is

$$K_{eff} = \frac{h}{a}K_{sh} + K_{sp}, \text{ where } K_{sh} = \frac{\rho_s c_p^2}{2} \text{ and } K_{sp} = \frac{\kappa}{4}\cot\left(\frac{\pi}{J}\right). \tag{2.31}$$

The effective bulk modulus is greater than that of the bare shell and the increase, K_{sp}, is proportional to the spring stiffness. The effective density is the ratio of total mass to volume, $\rho_{eff} = (m_s + m)/(\pi a^2)$, where $m_s = \rho_s \pi (a^2 - (a-h)^2)$ is the mass per unit length of the shell. Hence, since $h \ll a$ by assumption,

$$\rho_{eff} = \rho_m + \rho_s \left(2\frac{h}{a} - \left(\frac{h}{a}\right)^2 \right) \tag{2.32a}$$

$$\approx \rho_m + 2\frac{h}{a}\rho_s, \tag{2.32b}$$

where $\rho_m = \frac{m}{\pi a^2}$ is the added density.

For instance, consider an aluminum shell of thickness to radius ratio $h/a = 0.03$. Per Table 2.1, this shell is less stiff and less dense than water and thus can accommodate an internal substructure. The normalized effective properties of this shell are $\rho_{eff}/\rho = 0.16$ and $K_{eff}/K = 0.53$. To obtain the properties of water, 84 percent mass $\rho_m = 0.84\rho$ and 47 percent stiffness $K_{sp} = 0.47K$ have to be added. This procedure is graphically demonstrated in Figure 2.6.

2.3.2 Ribs-rod model

A more physical model of the substructure is a central rod with lengthwise ribs supporting it as shown in Figure 2.7(a). The one-component substructure in Figure 2.7(a) has $J = 16$ elastic stiffeners (ribs) of thickness t and a central mass (rod) of radius r_1 made of the same material. The elastic modulus and density of the internal mechanism are E_1 and ρ_1, respectively. Assuming that the stiffeners only deform radially, the effective stiffness (per unit axial length) is $\kappa = E_1 t/(a-h-r_1)$. This first order approximation for additional stiffness κ will prove sufficient for low frequency tuning. The second parameter of interest is the mass of the internal mechanism, $m_1 = \rho_1 \left(Jt(a-h-r_1) + \pi r_1^2 \right)$.

The two variables which define the geometry of the internal mechanism, t and r_1, determine the effective bulk modulus and density of the shell-substructure system. From equation (2.31), the contribution of the internal oscillator to the bulk modulus of the shell-stiffener-mass system is $K_{sp} = \frac{1}{4}\cot(\pi/J) E_1 t/(a-h-r_1)$. Thus the effective

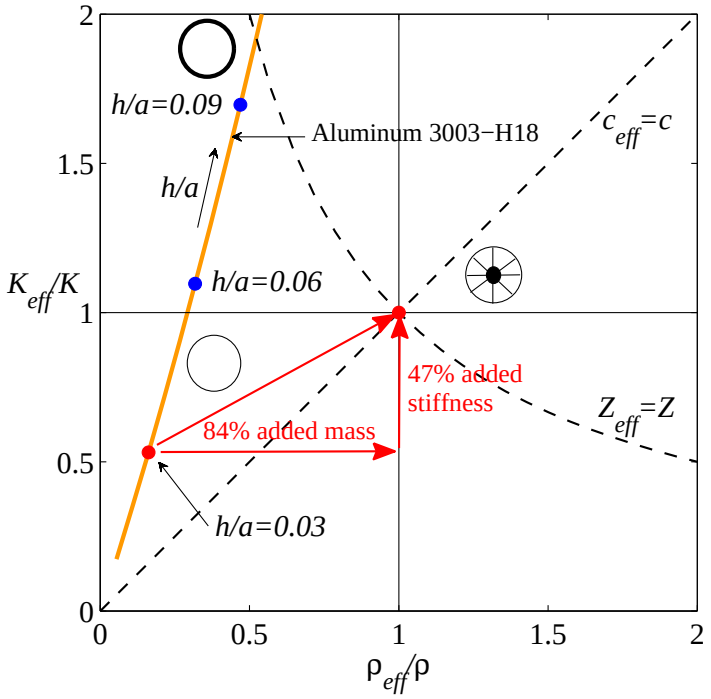

Figure 2.6: Linear plot of K_{eff}/K versus ρ_{eff}/ρ as h/a is varied for an aluminum shell. A shell of thickness $h/a = 0.3$ is tuned to water by adding mass and stiffness. The dashed black lines indicate the matched impedance and sound speed.

properties of the combined system become (see equations (2.31) and (2.32))

$$K_{eff} = K_{sh}\frac{h}{a} + \frac{\cot(\pi/J)E_1 t}{4(a-h-r_1)}, \tag{2.33a}$$

$$\rho_{eff} = \rho_s\frac{h}{a}\Big(2-\frac{h}{a}\Big) + \rho_1\Big(\frac{J}{\pi}\frac{t}{a}\big(1-\frac{h}{a}-\frac{r_1}{a}\big) + \big(\frac{r_1}{a}\big)^2\Big), \tag{2.33b}$$

where the $\mathrm{O}((h/a)^2)$ term in the shell volume is retained for improved accuracy. To get the effective properties, the density of the shell has to be increased by $\rho_m = \rho_{eff} - \rho_s\big(2\frac{h}{a} - (\frac{h}{a})^2\big)$.

Next define the ratio of required additional stiffness in each stiffener to the elastic modulus of the internal material

$$\hat{K} = \frac{4J}{\pi E_1}\big(K - K_{sh}\frac{h}{a}\big)\tan\big(\frac{\pi}{J}\big). \tag{2.34}$$

Solving the stiffness condition (2.33a) for t yields

$$t = J^{-1}\pi\hat{K}(a-h-r_1). \tag{2.35}$$

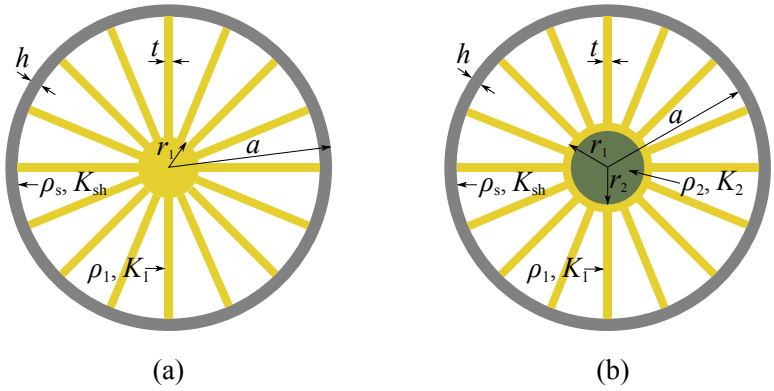

Figure 2.7: Schematic of the tuned shell. Plot (a): a one-component internal mechanism consists of $J = 16$ stiffeners (ribs) with thickness t and a central rod of radius r_1. Plot (b) shows the same internal mechanism, but with an added internal rod of radius r_2.

Substituting into the density condition in (2.33b) yields a quadratic equation for r_1/a,

$$\left(\frac{r_1}{a}\right)^2 + \hat{K}\left(1 - \frac{h}{a} - \frac{r_1}{a}\right)^2 - \frac{\rho_m}{\rho_1} = 0. \tag{2.36}$$

Equations (2.36) and (2.35) provide the geometry of the substructure. Note that since the formulation is in terms of area, there are two solution for r_1 in equation (2.36). There is no guarantee that both solutions will be physically realizable. For $h/a \ll 1$, the roots are approximately $r_1/a = (\hat{K}+1)^{-1}\big(\hat{K} \pm \sqrt{(\rho_m/\rho_1)(\hat{K}+1) - \hat{K}}\big)$.

It can happen that the density of the internal mechanism material is so low, as in some plastics used in rapid prototyping, that it becomes difficult to match both the density and bulk modulus. In that case, a heavy central rod of radius r_2 can be added as shown in Figure 2.7(b). This rod has practically no effect of the effective stiffness, but does offset the density. The effective bulk modulus for this system is the same as in equation (2.33a), and the effective density changes as follows

$$\rho_{eff} = \rho_s \frac{h}{a}\left(2 - \frac{h}{a}\right) + \rho_1\left(\frac{J}{\pi}\frac{t}{a}\left(1 - \frac{h}{a} - \frac{r_1}{a}\right) + \left(\frac{r_1}{a}\right)^2\right) + (\rho_2 - \rho_1)\left(\frac{r_2}{a}\right)^2, \tag{2.37}$$

where ρ_2 and K_2 are the density and bulk modulus of the central rod. Three parameters now define the geometry of the internal mechanism: t, r_1 and r_2. Since there are two conditions, (2.33a) and (2.37), the radius of the internal oscillator is determined after selecting the fraction of density added by the rod $f_\rho \leq \rho_m/\rho_2$, which yields $r_2/a = \sqrt{f_\rho}$ Recalling equation (2.35) for t, and using the definition of ρ_m, equation (2.37) can be

rearranged as

$$\Big(\frac{r_1}{a}\Big)^2 + \hat{K}\Big(1 - \frac{h}{a} - \frac{r_1}{a}\Big)^2 + \Big(\frac{\rho_2}{\rho_1} - 1\Big)\Big(\frac{r_2}{a}\Big)^2 - \frac{\rho_m}{\rho_1} = 0. \tag{2.38}$$

It is clear if $\rho_2 = \rho_1$, equation (2.38) gives the solution for a one-component oscillator, i.e. equation (2.36). For a very thin shell with $h/a \ll 1$, the roots are approximately $r_1/a = (\hat{K}+1)^{-1}\big(\hat{K} \pm \sqrt{(\hat{\rho}/\rho_1)(\hat{K}+1) - \hat{K}}\big)$, where $\hat{\rho} = \rho_m - f_\rho(\rho_2 - \rho_1)$. The discriminant goes to zero if we select f_ρ such that $\frac{\rho_m}{\rho_1} - f_\rho(\frac{\rho_2}{\rho_1} - 1) = \frac{\hat{K}}{\hat{K}+1}$ giving the single solution $\frac{r_1}{a} = \frac{\hat{K}}{\hat{K}+1}$ which corresponds to the largest possible central rod.

2.3.3 Water-like aluminum shell with an acrylic substructure

Consider tuning to water the aluminum shell of thickness $h/a = 0.3$ described in Section 2.3.1 with an acrylic substructure with properties ($\rho_1 = 1190$ kg/m^3, $E_1 = 3.2$ GPa, $\nu_1 = 0.35$). For reasons to be discussed later, $J = 16$ stiffeners are to be used in attaching the central rod to the shell. First, equation (2.36) is solved for (r_1/a) and then equation (2.35) is used to get the thickness. The two solutions for the oscillator's parameters are $(r_1/a, t/a) = (0.821, 0.040)$ and $(0.303, 0.180)$. The lower limit on the internal mass radius r_1 is geometrically constrained by the thickness of each stiffener. The intersection of stiffeners gives a lower bound of roughly $r_1 > Jt/(2\pi)$. In the second solution the radius r_1 is below this bound. This implies that the density is not matched to water, and consequently, only the first solution is retained.

Although the present representation of the added stiffness is a good approximation, it is not exact. The first solution was optimized in COMSOL yielding the exact bulk modulus of water. The geometry of the oscillator was found to be

$$(r_1/a, t/a) = (0.796, 0.081), \tag{2.39}$$

corresponding to $(\rho_{eff}, K_{eff}) = (1000.8\,\mathrm{kg/m^3}, 2.251\,\mathrm{GPa})$.

The radius ratio r_1/a of the inner rod is rather large. It can be made smaller while still matching the effective properties to water by inserting a central steel rod ($\rho_2 = 7944\,\mathrm{kg/m^3}$, $E_2 = 200\,\mathrm{GPa}, \nu_2 = 0.28$). Solving equation (2.38) and using (2.35) yields $(r_1/a, r_2/a, t/a) = (0.560, 0.167, 0.110)$, which were optimized in COMSOL to

give

$$(r_1/a, r_2/a, t/a) = (0.560, 0.129, 0.143). \tag{2.40}$$

Figure 2.8 shows the two substructure designs in equations (2.39) and (2.40).

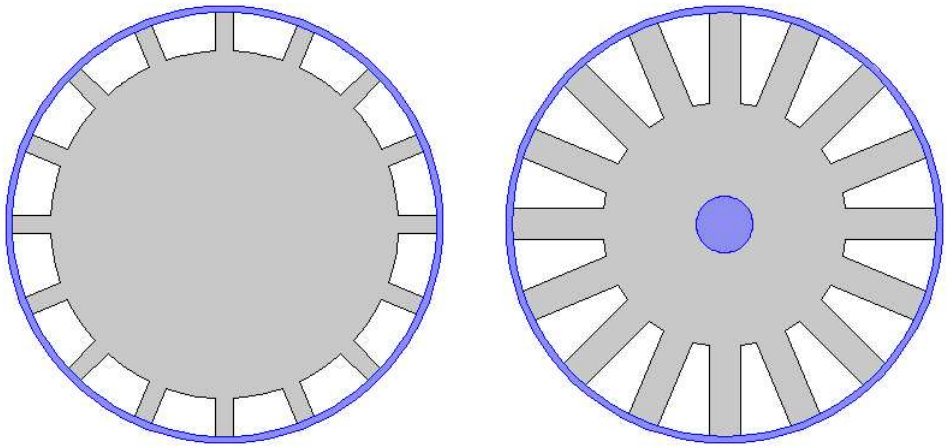

Figure 2.8: Aluminum shell of thickness $h/a = 0.03$ tuned to water with an acrylic substructure. Plot (a) shows the one-component substructure described by equation (2.39). Plot (b) shows the two-component substructure from equation (2.40).

2.3.4 Manufacturability

The oscillator designs in Figure 2.8 are well suited for rapid prototyping. However, that process takes a very long time and the bulk properties of the resulting substructure can be affected by porosity. A faster and more cost effective way to manufacture the acrylic inserts is to machine down acrylic rods. Typical milling bits have rectangular cross sections and thus the design has to be altered so the ribs rather that the voids have a trapezoidal profile. Figure (2.9b) shows the aluminum shell of thickness $h/a = 0.03$ tuned to water with the machined oscillator. It is non-trivial to derive the effective bulk modulus of this system as a function of the tool depth ratio t/a. Therefore, K_{eff} was obtained numerically in COMSOL. Figure (2.9b) shows the effective bulk modulus as a function of the tool depth t. The curve in Figure 2.9 was obtained by matching the density via the tool diameter d for a given tool depth t. The curve is quadratic with a maximum around $t/a = 0.08$.

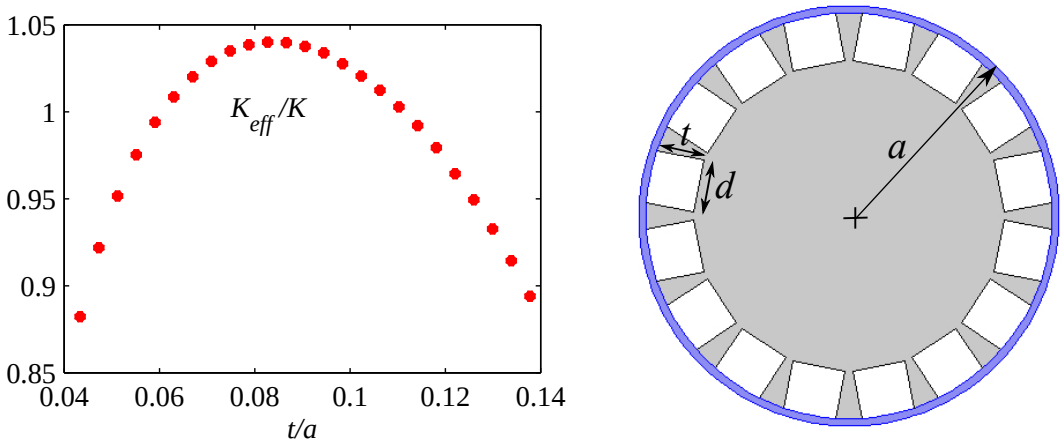

Figure 2.9: Machined acrylic insert tuning an aluminum shell of thickness $h/a = 0.03$ to water. Plot (a) shows the effective bulk modulus as a function of the normalized tool depth t/a with density matched by the tool diameter d. Plot (b) shows one geometry which gives the parameters of water.

Chapter 3

Scattering from an elastic shell with internal substructure

The dynamic response of an elastic shell in an acoustic medium was analysed in the original work of Bleich and Baron [6] and many other in the years since. Historically, acoustic scattering form cylindrical elastic shells has received much attention from the Naval research community. Primarily because many underwater vehicles and weaponry has the iconic cylindrical structure. The interested reader is referred to the text by Junger and Feit [44] for an in-depth look at fluid-structure interaction. What makes the study of scattering from elastic shells in water particularly interesting and important is that the inertial and stiffness properties of the shell and water are comparable, unlike in airborne sound. Thus a strong coupling exist between the vibration of the shell and the acoustic radiation shed into the surrounding fluid.

The chapter is organized as follows. Acoustic scattering from an empty thin elastic shell is described in § 3.1. This is then used to compare the frequency dependent scattering from the empty tuned shells described in Chapter 2. In § 3.2, the more complicated problem of a shell with an internal substructure is solved. Properties of the general solution are discussed in § 3.3. It is shown that the scattered field decomposes into J distinct parts, and that the additional portion of the T-matrix due to the internal springs-mass system can be expressed by J products of vectors, convenient for implementation. Numerical examples are given in § 3.4 along with a discussion of the backscatter and total scattering cross section for plane wave incidence and various spring distributions. Approximate but useful expressions are derived for the effective resonance frequencies of the shell-springs-mass system. An acoustically transparent aluminum shell is described in § 3.5.

3.1 Fluid loaded empty shell

Consider in-plane acoustic wave scattering from a thin cylindrical shell immersed in water. The thin shell has outer radius a, thickness $h\,(\ll a)$, volumetric mass density ρ_s, with elastic properties characterized by Young's modulus E_s and Poisson's ratio ν_s (see Figure 2.1). We assume time dependence $\mathrm{e}^{-i\omega t}$, which is henceforth omitted but understood. The total acoustic pressure on the shell p satisfies the Helmholtz equation

$$\nabla^2 p + k^2 p = 0, \tag{3.1}$$

where $k = \omega/c$ is the acoustic wavenumber. The pressure can be decomposed into two parts, the incident and scattered fields, p_i and p_s respectively, each a separate solution of Helmholtz's equation. Here we consider in-plane or 2D motion with plane wave incidence, requiring only the planar modes. Thus,

$$p = p_i + p_s, \quad p_i = \sum_{n=-\infty}^{\infty} A_n J_n(kr)\mathrm{e}^{in\theta}, \quad p_s = \sum_{n=-\infty}^{\infty} B_n H_n^{(1)}(kr)\mathrm{e}^{in\theta}, \quad r \geq a \tag{3.2}$$

with A_n the incident field coefficients, B_n the scattering coefficients, J_n the Bessel function of the first kind of order n and $H_n^{(1)}$ the Hankel function of the first kind of order n. The objective is to get a relation between the incident amplitudes A_n and the scattering amplitudes B_n. The solution is embodied in the infinite T-matrix defined by [64]

$$\mathbf{B} = \mathbf{T}\mathbf{A}, \tag{3.3}$$

where $\mathbf{A}$ and $\mathbf{B}$ are vectors of infinite length comprised of the elements A_n and B_n at position $n \in \mathbb{Z}$, respectively. The next step is to solve the equation governing wave propagation in the shell. The Donnel-Mushtari thin shell theory is the least complicated of the shell theories and will be used herein. The equations of motion for a thin cylindrical shell in the r and θ directions, respectively, are [44]

$$\frac{1}{a^2}\frac{\partial v}{\partial \theta} + \frac{w}{a^2} + \frac{\beta^2}{a^2}\frac{\partial^4 w}{\partial \theta^4} + \frac{\ddot{w}}{c_p^2} = \frac{\sigma(\theta, t)}{\rho_s c_p^2 h}, \tag{3.4a}$$

$$\frac{1}{a^2}\frac{\partial^2 v}{\partial \theta^2} + \frac{1}{a^2}\frac{\partial w}{\partial \theta} - \frac{\ddot{v}}{c_p^2} = 0, \tag{3.4b}$$

where w and v are the radial and azimuthal displacement, respectively, σ is the normal stress acting in the radial direction and $\beta = h/(\sqrt{12}a)$. The displacements and the normal stress are expanded in normal modes

$$(w,\, v,\, \sigma) = \sum_{n=-\infty}^{\infty} \big(W_n,\, V_n,\, \sigma_n\big)\, \mathrm{e}^{in\theta}. \tag{3.5}$$

Substituting equations (3.5) into (3.4) gives the modal equations as

$$\begin{gathered} (-\Omega^2 + 1 + \beta^2 n^4) W_n + inV_n = \frac{a^2 \sigma_n}{\rho_s c_p^2 h}, \\ inW_n + (\Omega^2 - n^2) V_n = 0, \end{gathered} \tag{3.6}$$

where the non-dimensional frequency is

$$\Omega = \frac{\omega a}{c_p} \quad \Big(= \frac{c}{c_p} ka \Big). \tag{3.7}$$

The characteristic equation of the free-vibration solution with $\sigma_n = 0$ yields the natural frequencies for the radial modes Ω_r and circumferential modes Ω_c, respectively

$$\begin{aligned} \Omega_{r,c}^2 &= \frac{1}{2}\left((1 + n^2 + \beta^2 n^4) \mp \sqrt{(1+n^2)^2 + 2\beta^2 n^4 (1 - n^2)} \right) \\ &= (\beta n^2, n), \quad \beta \ll 1. \end{aligned} \tag{3.8}$$

In the presence of forcing σ_n, such as an incident wave, the modal equations (3.6) are solved for the displacement W_n in terms on σ_n. The resulting expression is written in terms of a shell impedance Z_n^{sh} as

$$\sigma_n = -i\omega Z_n^{sh} W_n, \tag{3.9a}$$

$$Z_n^{sh} = -i\rho_s c_p \frac{h}{a} \Big[\Omega - \frac{\beta^2 n^4}{\Omega} - \Big(\Omega - \frac{n^2}{\Omega} \Big)^{-1} \Big]. \tag{3.9b}$$

Note that the shell impedance Z_n^{sh} is either mass or stiffness-like, depending on the frequency. The natural frequencies of the shell (3.8) correspond to the existence of nontrivial solutions in the absence of loading, and hence are defined as the roots of $Z_n^{sh}(\Omega) = 0$.

Continuity between the radial shell velocity and the radial particle velocity in the fluid, combined with the momentum equation in the fluid implies, using equation (3.2), that $\ddot{w} = -\rho^{-1} \partial p / \partial r$ on $r = a$, hence

$$\rho c \omega W_n = A_n J_n'(ka) + B_n H_n^{(1)\prime}(ka) \quad \Rightarrow \quad B_n = \frac{1}{H_n^{(1)\prime}(ka)} [\rho c \omega W_n - A_n J_n'(ka)]. \tag{3.10}$$

Expanding the surface pressure as $p(a,\theta) = \sum_{-\infty}^{\infty} P_n \mathrm{e}^{in\theta}$ and substituting together with B_n from equation (3.10) into equation (3.2) yields the modal pressure

$$P_n = -i\omega Z_n W_n + i\frac{2}{\pi ka}\frac{A_n}{H_n^{(1)\prime}(ka)}, \tag{3.11}$$

where Z_n is the acoustic impedance defined as

$$Z_n = i\rho c \frac{H_n^{(1)}(ka)}{H_n^{(1)\prime}(ka)}. \tag{3.12}$$

The Wronskian identity $J_n(x)H_n^{(1)\prime}(x) - J_n'(x)H_n^{(1)}(x) = \frac{2i}{\pi x}$ was used to get equation (3.11).

The radial stress on the shell is balanced by the acoustic pressure $\sigma_n = -P_n$, which can be expressed in terms of the dimensionless frequency $\Omega = \omega a/c_p$ as

$$\begin{aligned}\frac{a^2}{\rho_s c_p^2 h}\sigma_n &= -\frac{a^2}{\rho_s c_p^2 h}P_n \\ &= -\frac{\rho c}{\rho_s c_p}\frac{\Omega}{h/a}\frac{H_n^{(1)}(ka)}{H_n^{(1)\prime}(ka)}W_n - i\frac{2a}{\pi\rho_s c_p^2 h/a}\frac{A_n}{kaH_n^{(1)\prime}(ka)},\end{aligned} \tag{3.13}$$

where $\rho_s c_p^2 h/2a = K_{sh}h/a$ is the effective quasi-static bulk modulus of the shell (see equation (2.31)). The scattering coefficients are obtained by solving (3.6) for radial modal displacement W_n

$$W_n = \frac{2}{\pi\omega ka}\frac{A_n}{\zeta_n}, \quad \zeta_n = (Z_n^{sh} + Z_n)H_n^{(1)\prime}(ka). \tag{3.14}$$

The term ζ_n contains the total impedance $(Z_n^{sh} + Z_n)$, which highlights the parallel summation of the shell and acoustic impedances. Substituting equation (3.14) into equation (3.10) and rearranging yields the sought T-matrix, which relates the incident and scattered pressure fields as (* denotes the complex conjugate)

$$\boldsymbol{B} = \mathrm{diag}(T_n)\boldsymbol{A}, \quad T_n = \frac{1}{2}\Big(\frac{\zeta_n^*}{\zeta_n} - 1\Big). \tag{3.15}$$

The associated elements of the diagonal "S-matrix" are

$$S_n = 1 + 2T_n \implies S_n = \mathrm{e}^{-i2\phi_n}, \;\; T_n = -i\mathrm{e}^{-i\phi_n}\sin\phi_n, \;\; \text{with } \phi_n = \arg\zeta_n, \tag{3.16}$$

implying that $|S_n| = 1$, $|T_n| \leq 1$, in conformity with the fact that no dissipation is assumed.

3.1.1 Far-field

The acoustic far-field begins when the pressure amplitude exhibits cylindrical spreading and the pressure is independent of the azimuthal angle θ. As a result the spatial dependence of the pressure field in the far-field is simplified. Using the large argument approximation of the Hankel function $H_n^{(1)}(kr) = \sqrt{2/(\pi kr)}\mathrm{e}^{i(kr-n\pi/2-\pi/4)} + O((kr)^{-3/2})$ for $kr \gg 1$, the far-field scattered pressure field is

$$p_s = \sqrt{\frac{a}{2r}}\mathrm{e}^{ikr} g(\theta) + O\Big((kr)^{-3/2}\Big), \quad kr \gg 1, \tag{3.17}$$

where the form function g follows from equation (3.2)

$$g(\theta) = \sum_{n=-\infty}^{\infty} g_n \mathrm{e}^{in\theta}, \quad g_n = \frac{2\mathrm{e}^{-i\frac{\pi}{4}}}{\sqrt{\pi ka}}(-i)^n B_n. \tag{3.18}$$

Forward scatter is defined as $g(0)$, whereas $g(\pi)$ defines the backscattered pressure. Forward and backward scatter are useful indicators of the scattered field at a given point, but do not provide information about the total scattered power directly.

The total scattering cross section (TSCS or σ_{tot}), which is a measure of the power scattered in all directions due to an incident wave, will be used throughout to compare scattering from various shells. Integrating the scattered pressure in the far-field, the TSCS is defined as

$$\sigma_{tot} = \frac{r}{a}\int_0^{2\pi} p_s p_s^* d\theta = \frac{1}{2}\int_0^{2\pi} |g(\theta)|^2 d\theta = \frac{4}{ka}\sum_{n=-\infty}^{\infty} |B_n|^2. \tag{3.19}$$

The TSCS has been calculated for the special tuned shells of Table 2.2 and the composite shells of Table 2.3. An appropriate baseline for comparing different shell designs is scattering from a rigid cylinder. The sound-hard boundary condition $\partial w/\partial r|_{r=a} = 0$ yields the scattering coefficients $B_n = -J_n'(ka)/H_n^{(1)\prime}(ka)$.

It is clear that the tuned shells are nearly transparent at low frequencies as compared to a rigid cylinder of the same size. For the lead-aluminum and lead-copper bi-layer shells, the TSCS remains low up to about $ka = 2.5$. For the acrylic shell, the TSCS is zero up to about $ka = 0.7$ where there is an $n = 2$ flexural resonance. The total and absolute pressure fields for the lead-aluminum shell and the rigid cylinder are compared in Figure 3.2 at $ka = 2.5$. There is very little scattering from the lead-aluminum shell

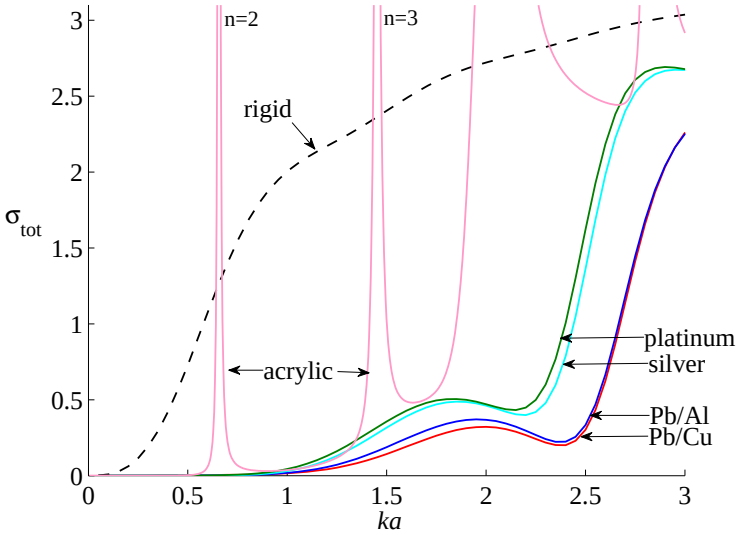

Figure 3.1: Total scattering cross section for acoustically transparent single layer and bi-layer shells. The dashed line represents the TSCS for a rigid cylinder of the same size. The shell thicknesses are given in Table 2.2 and 2.3. The $n = 2$ and $n = 3$ flexural resonances of the thick acrylic shell are labelled.

of radius $a = 1$ cm even when the wavelength is just slightly less then the diameter. This proves that the elastic shell is indeed behaving almost as an acoustic medium at sub-wavelength frequencies. On the other hand, there is much scattering from the rigid cylinder.

3.1.2 Consequence of matching density and bulk modulus

The idea thus far has been to tune elastic shells to behave as an acoustic medium in the quasi-static regime. To see the consequence of doing so, expand the T-matrix in equation (3.15) for low ka yielding

$$T_0 = \frac{i\pi}{4}\left(\frac{K}{K_{eff}} - 1\right)(ka)^2 + O((ka)^4), \tag{3.20a}$$

$$T_1 = \frac{i\pi}{4}\left(\frac{\rho_{eff} - \rho}{\rho_{eff} + \rho}\right)(ka)^2 + O((ka)^4), \tag{3.20b}$$

$$T_2 = \frac{i\pi}{32}(ka)^4 + O((ka)^6), \tag{3.20c}$$

for modes $n = 0, 1, 2$, respectively. Thus it is clear that the leading term in T_0 depends on bulk modulus and the leading term in T_1 is inertial. By tuning the effective density

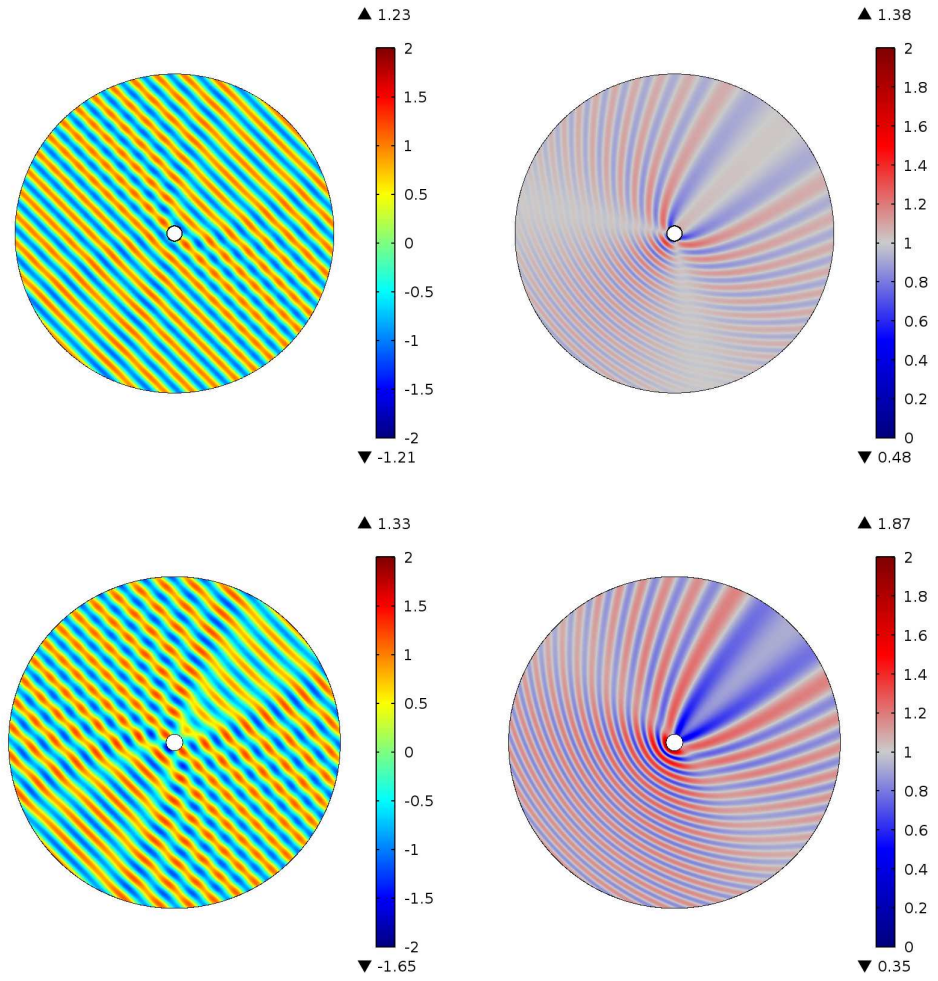

Figure 3.2: Top: Total and absolute pressure fields for the lead-aluminum shell in Figure 3.1 at $ka = 2.5$. Bottom: Same pressure plots but for the rigid cylinder. The radii are $a = 1$ cm and incidence is at 45°

and bulk modulus of the shell to water guarantees $T_n = O((ka)^4)$, leaving a large low-frequency region of no scattering as seen in Figure 3.2. In other words, the monopolar and dipolar response is no longer dominant at low ka. The quadrupolar response T_2 cannot be diminished. Moreover, from equation 3.19, the TSCS is proportional to $\sigma_{tot} = O((ka)^7)$ (see Figure 3.1).

3.2 Shell with an internal springs-mass system

The scattering of acoustic waves from an elastic cylindrical shell with an internal structure is quite distinct from the response of a simple shell. Excitation of waves on shells

arises from two general mechanisms: (i) phase matching to supersonic membrane-type waves [91, 88, 74], or (ii) excitation at structural discontinuities. The latter can excite both supersonic longitudinal waves which then re-radiate into the fluid, and subsonic flexural waves which can persist for long times and over large propagation paths on the structure. Flexural waves are an important source of structural energy transfer, but they are not usually excited on a smooth metallic shell in contact with an exterior acoustic medium such as water because of their subsonic phase speed. The effect of structural discontinuities or constraints can be modeled as effective forces on an otherwise smooth shell, analyzed in the original work of Bleich and Baron [6].

Structural constraints can be separated into three fundamental types: concentrated, linear circumferential, and linear lengthwise. Attachment of a spring-mass system or a beam to the interior surface of the shell constitutes a concentrated constraint. The constraint inhibits or enhances the vibration of the shell through reflection/conversion of structural waves as well as through the resonant behavior of the substructure itself. Undersea vehicles are sometimes modeled as a shell with many spring-mass oscillators attached to the interior. Analysis of such "fuzzy structures" indicates possible wave localization due to structural irregularity, which in turn suggests methods for controlling vibration/scattering [80, 40, 99, 77, 10, 79].

The other type of constraint, circumferential discontinuities, include examples such as rigid discs [92], plates, rings [20], ribs, bulkheads [16, 35, 5, 78, 19, 18, 62, 106, 107], and any other frames thin in the axial direction. Bloch-Floquet waves and Bragg scattering effects appear for oblique incidence if the internals are placed periodically along the axis of the shell, [106, 107]. Analysis of oblique incidence onto shells with several bulkheads show that constructive interference between the scattered pressure due to each bulkhead produces a dipole-like radiation pattern and scattered pressure associated with bending moments yields a quadrupole-like radiation pattern [19, 18].

This Section is concerned with the two dimensional (2D) modeling of lengthwise sheet springs supporting an internal mass as explored in [2, 33, 39], which can be viewed as lengthwise discontinuities. More sophisticated and certainly more realistic models such as deck-type plates [4, 47, 34, 36, 3] and lengthwise elastic ribs [47, 46] also

fall into the category of lengthwise discontinuities. These internal structures provide more mechanisms for coupling to and mixing of the structure-borne waves producing a very complex response. With normal wave incidence and a sufficiently long shell, lengthwise constraints can be analyzed in two dimensions as will be done herein.

Understanding of cause and effect can be obtained through detailed analysis of simple models for internal structure. The simplest model for internal structure is a single mass attached by a single spring to the shell. The structural analogue of this system is a long internal rod attached to the shell by a lengthwise rib. Although springs cannot support the passage of waves, this is a rich and relatively complex system as compared to the bare shell, and it displays many of the dynamic properties of much more complex substructures. The first such analysis by Achenbach et al. [2] considered the 2D problem of a shell with an internal mass supported by a single spring and loaded by an external point force. Via an energy formulation the interaction force between the spring-mass system and the shell was determined and its affect on the acoustic scattering studied, especially in the vicinity of the spring-mass resonance. The presence of the substructure generates acoustic radiation which can be greater or lesser than that of the standalone shell based on the frequency of the harmonic excitation relative to the resonance of the oscillator (spring-mass system).

The problem becomes more complicated when the mass is supported by more than one spring. Guo [33] formulated the scattering solution for a shell with an internal mass attached by a diametrical pair of springs (structural analogue being a rod supported by a diametric pair of lengthwise ribs). He demonstrated that there are two distinct solutions, for even and odd azimuthal modes, which superimpose to produce the overall response of the shell-springs-mass system. This simple model clearly reveals the rich and complex set of resonances resulting from flexural waves excited by the spring attachments. This stiffener-borne wave generation mechanism was investigated earlier by Klauson and Metsaveer [47]. Guo showed that the addition of a dissipative mechanism into the springs-mass system did little to the scattered field. Later, Gaunaurd [27] expanded the analysis by considering a neutrally buoyant spherical shell with a double spring-mass system. Spectral theory was used by Ho [39] to obtain the acoustic

response for a shell with the mass supported by a non-diametrical pair of springs.

The current work reconsiders acoustic scattering at low to mid-frequencies, $ka \leq 20$, from a shell with simpler internal structural models, focusing on a distribution of an arbitrary number of J springs supporting a central internal mass. This is an approximate 2D model of a central rod supported by an equally spaced distribution of J lengthwise ribs. The shell-spring-mass system is particularly interesting because of how differently it responds to an incident wave when compared to fluid filled shells or solid cylinders. Primary reasons for studying such systems include understanding: 1) the acoustic scattering from a shell with a finite number of coupled point forces along the circumference, 2) the propagation of flexural-borne waves into the far-field for different number of springs, 3) the shift in resonance frequencies of the flexural waves due to the added stiffness, 4) low-frequency transparency with large number of springs and 5) the effect of the angle of incidence on scattering. Furthermore, the acoustic response of the shell changes by selecting different spring stiffness and added mass. This ability to tune the shell expands the range of possible acoustic properties for shells presented in Martin et al. [65] and thus makes it a perfect element in graded index sonic crystals as introduced in § 2.3. Here we concentrate on deriving and quantifying the model for arbitrary number of internal springs.

The model considered expands the existing results [2, 33] for masses attached by one or two springs, to the more general case of J attachment springs, where $J \geq 1$ is arbitrary. For an axisymmetric distribution of such springs, teh symmetry of the problem is used to simplify the interaction force, which is later used to determine the T-matrix of the combined system. The results are presented successively for $J = 1$, $J = 2$, and finally $J \geq 3$ springs. The T-matrix is expressed in terms of physical quantities: acoustic, shell and spring impedance. These combine in a non-trivial way by virtue of the problem formulation to give the total impedance of the combined system. This total impedance governs the system's resonant behavior.

3.2.1 Summary of the main results

A single mass per unit axial length m is attached to the inner surface of the shell by a set of $J \geq 1$ springs each of stiffness κ (with units of force per unit area) oriented at angles θ_j with respect to the horizontal, where $j = 1, \ldots, J$. The springs are assumed equally distributed, so that $\theta_{j+1} = \theta_j + 2\pi/J$. The mass is of finite size and free to rotate, as shown in the schematic in Figure 3.3. Our main result is that the T-matrix has the following form

$$\mathbf{T} = \mathbf{T}^{(0)} + \sum_{j=1}^{J} \mathbf{b}_j \mathbf{b}_j^T, \tag{3.21}$$

where (* denotes the complex conjugate)

$$\mathbf{T}^{(0)} = \mathrm{diag}(T_n), \qquad T_n = \frac{1}{2}\left(\frac{\zeta_n^*}{\zeta_n} - 1\right), \quad \zeta_n = (Z_n^{sh} + Z_n) H_n^{(1)\prime}(ka), \tag{3.22a}$$

$$b_{j,n} = \frac{i}{\zeta_n}\left(\frac{2\rho c Z_n^{tot}}{\pi k a}\right)^{1/2} \quad \text{if } n = j \bmod J, \text{ otherwise } 0, \tag{3.22b}$$

and the impedances associated with azimuthal mode n relate the radial stress to radial velocity as (see (3.7) for Ω)

$$Z_n = i\rho c \frac{H_n^{(1)}(ka)}{H_n^{(1)\prime}(ka)}, \quad \widehat{Z}_n = i\rho c \frac{J_n(ka)}{J_n'(ka)}, \tag{3.23a}$$

$$Z_n^{sh} = -i\rho_s c_p \frac{h}{a}\Big[\Omega - \frac{\beta^2 n^4}{\Omega} - \Big(\Omega - \frac{n^2}{\Omega}\Big)^{-1}\Big], \tag{3.23b}$$

$$Z_n^{sp}(J) = \frac{iJ\kappa}{2\pi a \omega} \times \begin{cases} \frac{1}{1 - H_J \frac{\omega_{sp}^2}{\omega^2}}, & n = \pm 1 \bmod J, \\ 1, & \text{otherwise}, \end{cases}, \quad H_J = \begin{cases} J, & J = 1, 2, \\ \frac{J}{2}, & J \geq 3, \end{cases} \tag{3.23c}$$

and

$$\omega_{sp}^2 = \frac{\kappa}{m}, \tag{3.24}$$

is the natural frequency of the internal springs-mass system (see Figure 3.3). Different azimuthal modes are affected differently by the spring-mass system (see Z_n^{sp}) where the function $n = \pm 1 \bmod J$ is used here to mean

$$n = \pm 1 \bmod J \quad \Longleftrightarrow \quad n = \pm 1 + mJ, \text{ where } m = 0, \pm 1, \pm 2, \pm 3, \ldots \tag{3.25}$$

such that J is the modulus of the congruence. The various impedances can be interpreted as follows: Z_n is a radial acoustic impedance associated with radiating wave

functions, as compared with $\widehat{Z}_n$ for regular wave functions; Z_n^{sh} is the shell impedance; and Z_n^{sp} is a generalized spring impedance. The expression for Z_n^{sh} is based on the Donnell-Mushtari thin shell model, see §3.1, which is sufficient for the range of frequencies considered ($ka \leq 20$), although other expressions could be used, including the exact result from elastodynamics. Regardless of the specific shell model, the results in equations (3.26) and (3.21) retain their analytic structure. The total equivalent impedance Z_n^{tot} is defined by the series/parallel combination of the above impedances as

$$\frac{1}{Z_n^{tot}} = \frac{1}{Z_n^{sp}} + \sum_{p=-\infty}^{\infty} \frac{1}{Z_{n+pJ}^{sh} + Z_{n+pJ}}. \tag{3.26}$$

These results are derived next.

3.2.2 Problem formulation

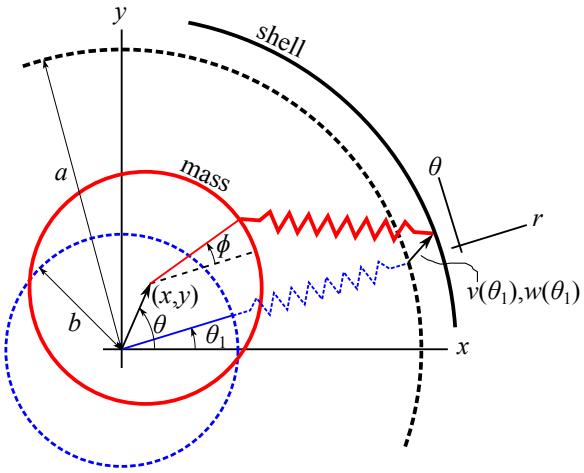

Figure 3.3: Displaced shell and internal mass (shown with solid lines) connected by a single spring initially oriented radially at an angle θ_1 from the x-axis.

Consider now the mass per unit length, m, attached to the shell as shown in Figure 3.3 by $J \geq 1$ springs each of stiffness per unit area, κ, oriented at angles θ_j, where $j = 1, \ldots, J$. The springs are assumed equally distributed, so that $\theta_{j+1} = \theta_j + 2\pi/J$. The horizontal and vertical displacements of the mass are denoted by x and y, respectively. The derivation of the linearized equations of motion for the internal mass and the resulting radial force on the shell are in Appendix A. In summary, the displacement

of the finite sized mass associated with its rotation is of second order and not retained in the linearized equations. Moreover, the angular motion of the mass is not excited by the acoustic incidence. Only the translating degrees of freedom of the mass contribute to the radial force on the shell. Introduce the force distribution per unit area of the shell surface, $f(\theta)$, defined such that $f dA$ is the force acting on an element $dA = a d\theta\, dz$. It follows from the Appendix that in the case of one, two, and $J \geq 3$ springs, respectively,

$$f(\theta) = -\frac{\kappa}{a}\left(\frac{\tau^2}{\tau^2 - 1}\right) w(\theta_1)\delta(\theta - \theta_1), \quad \text{one spring,} \tag{3.27a}$$

$$f(\theta) = -\frac{\kappa}{a}\left(\frac{1}{\tau^2 - 2}\right)\Big[\Big((\tau^2 - 1)w(\theta_1) - w(\theta_2)\Big)\delta(\theta - \theta_1) + \Big((\tau^2 - 1)w(\theta_2) - w(\theta_1)\Big)\delta(\theta - \theta_2)\Big], \quad \text{two springs,} \quad (\theta_2 = \theta_1 + \pi) \tag{3.27b}$$

$$f(\theta) = -\frac{\kappa}{a}\left(\frac{1}{\tau^2 - \frac{J}{2}}\right)\sum_{j=1}^{J}\left[\sum_{n=1}^{J} w(\theta_n)\cos(\theta_j - \theta_n) + \Big(\tau^2 - \frac{J}{2}\Big)w(\theta_j)\right]\delta(\theta - \theta_j), \tag{3.27c}$$

where $\delta(\theta)$ is the Dirac delta function and (see equation (3.7))

$$\tau^2 = \frac{\omega^2}{\omega_{sp}^2} \quad \Big(= \frac{m\omega^2}{\kappa}\Big). \tag{3.28}$$

Expanding the radial force distribution of equation (3.27) in azimuthal modes as

$$f(\theta) = \sum_{n=-\infty}^{\infty} f_n \mathrm{e}^{in\theta}, \tag{3.29}$$

and using the identity $\delta(\theta - \theta_j) = \frac{1}{2\pi}\sum\limits_{n=-\infty}^{\infty} \mathrm{e}^{in(\theta-\theta_j)}$ gives the modal force on the shell

for the cases of one, two, and $J \geq 3$ springs as

$$f_n = -\frac{\kappa}{2\pi a}\Big(\frac{\tau^2}{\tau^2-1}\Big)w(\theta_1)\mathrm{e}^{-in\theta_1}, \quad J=1, \tag{3.30a}$$

$$\begin{aligned} f_n &= -\frac{\kappa}{2\pi a}\Big(\frac{\tau^2-1-\mathrm{e}^{-in\pi}}{\tau^2-2}\Big)\big(w(\theta_1)+w(\theta_1+\pi)\mathrm{e}^{-in\pi}\big)\mathrm{e}^{-in\theta_1}, \\ &= -\frac{\kappa}{2\pi a}\sum_{j=1}^{2} w(\theta_j)\mathrm{e}^{-in\theta_j} \times \begin{cases} \frac{\tau^2}{\tau^2-2}, & \text{for odd } n, \\ 1, & \text{for even } n, \end{cases} \quad J=2, \end{aligned} \tag{3.30b}$$

$$\begin{aligned} f_n &= -\frac{\kappa}{2\pi a}\Big(\frac{1}{\tau^2-\frac{J}{2}}\Big)\sum_{j=1}^{J}\Big[\sum_{m=1}^{J} w(\theta_m)\cos(\theta_j-\theta_m)+\Big(\tau^2-\frac{J}{2}\Big)w(\theta_j)\Big]\mathrm{e}^{-in\theta_j}, \\ &= -\frac{\kappa}{2\pi a}\sum_{j=1}^{J} w(\theta_j)\mathrm{e}^{-in\theta_j} \times \begin{cases} \frac{\tau^2}{\tau^2-\frac{J}{2}}, & n=\pm 1 \bmod J, \\ 1, & \text{otherwise}, \end{cases} \quad J\geq 3, \end{aligned} \tag{3.30c}$$

where the results (A.19) and (A.22) were used for $J \geq 3$ axisymmetrically distributed springs with $\theta_{m+1} = \theta_m + 2\pi/J$ and the notation $n = \pm 1 \bmod J$ is defined in equation (3.25). The modal force for J springs is of only two types. The solution with the coefficient $\tau^2/(\tau^2 - \frac{J}{2})$ is the same as for the single spring. The dependence on τ^2 (i.e. the mass m) implies that the displacement of the internal mass contributes to the net modal force for modes $n = \pm 1 \bmod J$. The second solution is independent of m, suggesting that although the mass does displace as seen in (A.10), there is no net force on the shell due to this displacement.

Equations (3.30) indicate that the set of force coefficients $\{f_n\}$ depend upon J linearly independent combinations of the the radial displacements $\{w(\theta_j)\}$. Thus, for $J = 1$ we have $w(\theta_1)$ only; for $J = 2$ it is $w(\theta_1) + w(\theta_2)$ and $w(\theta_1) - w(\theta_2)$; for $J = 3$ we have $w(\theta_1) + w(\theta_2) + w(\theta_3)$, $w(\theta_1)\mathrm{e}^{-i\theta_1} + w(\theta_2)\mathrm{e}^{i\theta_1} + w(\theta_3)$, and $w(\theta_1)\mathrm{e}^{i\theta_1} + w(\theta_2)\mathrm{e}^{-i\theta_1} + w(\theta_3)$; etc. These independent combination of $\{w(\theta_j)\}$ can also be represented in terms of the infinite series of Fourier coefficients $\{W_m\}$, see equation (3.5). Assuming the springs are fixed to the shell at $\theta_j = j2\pi/J$, $j = 1, \ldots, J$, it follows from equations (3.30)

and (A.22) that the force coefficients can be succinctly expressed

$$f_n = -\frac{J\kappa}{2\pi a}\, w_n^{(J)} \times \begin{cases} \frac{\tau^2}{\tau^2-1}, & J=1, \\ \begin{cases} \frac{\tau^2}{\tau^2-2}, & n \text{ odd}, \\ 1, & n \text{ even}, \end{cases} & J=2, \\ \begin{cases} \frac{\tau^2}{\tau^2-\frac{J}{2}}, & n = \pm 1 \bmod J, \\ 1, & \text{otherwise}, \end{cases} & J \geq 3, \end{cases} \tag{3.31}$$

where

$$w_n^{(J)} \equiv \sum_{p=-\infty}^{\infty} W_{n+Jp}. \tag{3.32}$$

Note that $w_n^{(J)} = w_m^{(J)}$ if $m = n \bmod J$. Also, note that for a diametrical pair of springs, $J = 2$, the summation in (3.30) contains the term $(1 + \mathrm{e}^{i(m-n)\pi})$, which is zero unless n and m are both even or both odd, resulting in $1 + \mathrm{e}^{i(m-n)\pi} = 2$. The representation (3.31) for f_n will prove to be crucial for relating the internal dynamics with the external scattering.

3.2.3 The forcing coefficients

Now that we have an expression for the modal force on the shell in terms of the modal displacement we can substitute it into the equation of motion (3.4a) with the replacement $\sigma = f - p$, and hence $\sigma_n \to f_n - P_n$. The definition of the shell impedance (3.9) gives $f_n - P_n = -i\omega Z_n^{sh} W_n$. Combined with the continuity equation in the form (3.11), this yields (see (3.14) for ζ_n)

$$W_n = \frac{2A_n}{\pi\omega k a \zeta_n} - \frac{f_n}{i\omega(Z_n^{sh} + Z_n)}. \tag{3.33}$$

The scattered field is again given by equations (3.10) which involves the displacement coefficients W_n. It remains to find W_n as a function of the incident wave amplitudes A_n.

As shown in the previous section, there are J distinct forms of the modal force f_n, each dependent upon the $J-$cyclic parameters $w_n^{(J)}$ of (3.32). These may be determined

by taking appropriate summations of (3.33). Define the $J-$cyclic parameters

$$\frac{1}{Z_n^{(J)}} = \sum_{p=-\infty}^{\infty} \frac{1}{Z_{n+pJ}^{sh} + Z_{n+pJ}}, \quad p_n^{(J)} = \frac{i2Z_n^{(J)}}{\pi ka} \sum_{p=-\infty}^{\infty} \frac{A_{n+pJ}}{\zeta_{n+pJ}}, \tag{3.34}$$

then (3.33) implies

$$w_n^{(J)} = \frac{f_n - p_n^{(J)}}{-i\omega Z_n^{(J)}}. \tag{3.35}$$

Equations (3.31) and (3.35) now provide a pair of equations for $w_n^{(J)}$ and f_n. We next consider the solutions for $J = 1$, $J = 2$ and $J \geq 3$ separately.

A single spring $(J = 1)$

In this case there is only one modal displacement coefficient $w^{(1)} = w_n^{(1)}$ independent of n, as are the force coefficients f_n:

$$f_n = i\omega Z^{sp} w^{(1)} \quad \text{with} \quad w^{(1)} = \sum_{n=-\infty}^{\infty} W_n = \frac{(i\omega)^{-1} p^{(1)}}{Z^{(1)} + Z^{sp}} \tag{3.36}$$

where $p^{(1)} = p_n^{(1)}$, $Z^{(1)} = Z_n^{(1)}$ and Z^{sp} are

$$p^{(1)} = \frac{i2Z^{(1)}}{\pi ka} \sum_{n=-\infty}^{\infty} \frac{A_n}{\zeta_n}, \quad \frac{1}{Z^{(1)}} = \sum_{n=-\infty}^{\infty} \frac{1}{Z_n^{sh} + Z_n}, \quad Z^{sp} = \frac{i\kappa}{2\pi a\omega} \frac{\tau^2}{\tau^2 - 1}. \tag{3.37}$$

See equation (3.23b) for Z_n^{sh} and equation (3.23a) for Z_n. The effective spring impedance is denoted by Z^{sp} with a resonance frequency $\omega^2 = \omega_{sp}^2$, see (3.28).

Diametrical pair of springs $(J = 2)$

Now consider the internal mass being supported by a diametrical pair of springs. The modal force is given by equation (3.31). Unlike the single spring scenario, here, due to symmetry of the spring positions, odd and even modes engage the internal mass differently. This gives rise to the two solutions, for even and odd n, as

$$f_n = i\omega Z_{\substack{e \\ o}}^{sp} w_{\substack{e \\ o}}^{(2)} \quad \text{with} \quad w_{\substack{e \\ o}}^{(2)} = \sum_{n \text{ even/odd}} W_n = \frac{(i\omega)^{-1} p_{\substack{e \\ o}}^{(2)}}{Z_{\substack{e \\ o}}^{(2)} + Z_{\substack{e \\ o}}^{sp}} \tag{3.38}$$

where

$$p_{\substack{e\\o}}^{(2)} = \frac{i2Z_{\substack{e\\o}}^{(2)}}{\pi ka} \sum_{n\,\text{even/odd}} \frac{A_n}{\zeta_n}, \quad \frac{1}{Z_{\substack{e\\o}}^{(2)}} = \sum_{n\,\text{even/odd}} \frac{1}{Z_n^{sh} + Z_n}, \tag{3.39a}$$

$$Z_{\substack{e\\o}}^{sp} = \frac{i\kappa}{\pi a\omega} \times \begin{cases} \frac{\tau^2}{\tau^2-2}, & n \text{ odd}, \\ 1, & n \text{ even}. \end{cases} \tag{3.39b}$$

Similar expressions were derived by Guo in [33]. Note, for a diametrical pair of springs, the resonance frequency is $\omega^2 = 2\omega_{sp}^2$, see $(3.28)_1$.

Axisymmetric distribution of three or more springs ($J \geq 3$)

The solution for $J \geq 3$ axisymmetrically distributed springs is essentially the same as for two springs, namely,

$$f_n = i\omega Z_n^{sp} w_n^{(J)} \quad \text{where} \quad w_n^{(J)} = \sum_{p=-\infty}^{\infty} W_{n+pJ} = \frac{(i\omega)^{-1} p_n^{(J)}}{Z_n^{(J)} + Z_n^{sp}}, \tag{3.40}$$

with

$$p_n^{(J)} = \frac{i2Z_n^{(J)}}{\pi ka} \sum_{p=-\infty}^{\infty} \frac{A_{n+pJ}}{\zeta_{n+pJ}}, \quad \frac{1}{Z_n^{(J)}} = \sum_{p=-\infty}^{\infty} \frac{1}{Z_{n+pJ}^{sh} + Z_{n+pJ}}, \tag{3.41}$$

and

$$Z_n^{sp} = \frac{iJ\kappa}{2\pi a\omega} \times \begin{cases} \frac{\tau^2}{\tau^2 - \frac{J}{2}}, & n = \pm 1 \bmod J, \\ 1, & \text{otherwise}. \end{cases} \tag{3.42}$$

The summation in (3.40) is J-cyclic, $w_n^{(J)} = w_{n \bmod J}^{(J)}$. Thus, there are J unique solutions that need to be determined $\{w_0^{(J)}, w_1^{(J)}, w_2^{(J)}, \ldots, w_{J-1}^{(J)}\}$, where the spring impedance for $w_1^{(J)}$ and $w_{J-1}^{(J)}$ differs from other solutions as seen in equation (3.42).

3.2.4 Scattering solution

Write the scattering coefficients from equation (3.10) as

$$B_n = B_n^{(0)} + B_n^{(1)}, \tag{3.43}$$

where $B_n^{(0)}$ are the values for system with no internal spring-mass system. Thus, using equations (3.15) and (3.33),

$$B_n^{(0)} = \frac{1}{2}\left(\frac{\zeta_n^*}{\zeta_n} - 1\right) A_n, \qquad B_n^{(1)} = i\rho c \frac{f_n}{\zeta_n}. \tag{3.44}$$

Substituting the forcing coefficient of equation (3.40) into equation $(3.44)_2$, the contribution of the internal spring-mass system to the scattering coefficient is

$$B_n^{(1)} = i\rho c \frac{Z_n^{tot}\, p_n^{(J)}}{Z_n^{(J)} \zeta_n}, \qquad \frac{1}{Z_n^{tot}} = \frac{1}{Z_n^{(J)}} + \frac{1}{Z_n^{sp}}, \tag{3.45}$$

where Z_n^{tot} is the equivalent total impedance of the shell-spring-mass system.In the following subsections, the scattering coefficients and the T-matrices are determined separately for $J = 1$, $J = 2$, and $J \geq 3$ springs.

Scattering coefficients, $J = 1$

For a single spring, the scattering coefficient is

$$B_n^{(1)} = -\frac{2\rho c Z^{tot}}{\pi k a \zeta_n} \sum_{m=-\infty}^{\infty} \frac{A_m}{\zeta_m}. \tag{3.46}$$

Equation (3.46) can be rewritten compactly by defining the infinite vector $\mathbf{b}$ with elements b_n as

$$\mathbf{B}^{(1)} = \mathbf{b}\mathbf{b}^T\mathbf{A} \quad \text{with} \quad b_n = \frac{i}{\zeta_n}\left(\frac{2\rho c Z^{tot}}{\pi k a}\right)^{1/2}. \tag{3.47}$$

Hence, referring to equation (3.3) where, after truncating the series at N, the vectors $\mathbf{B}$ and $\mathbf{A}$ are

$$\mathbf{B}_{(2N+1)\times 1} = \begin{pmatrix} B_{-N} \\ B_{-N+1} \\ \cdots \\ B_N \end{pmatrix}, \quad \mathbf{A}_{(2N+1)\times 1} = \begin{pmatrix} A_{-N} \\ A_{-N+1} \\ \cdots \\ A_N \end{pmatrix} \tag{3.48}$$

and the T-matrix is

$$\mathbf{T} = \mathbf{T}^{(0)} + \mathbf{b}\mathbf{b}^T, \tag{3.49}$$

where $\mathbf{T}^{(0)}$ is the diagonal matrix with elements T_n on the diagonal, see (3.15). The additional non-diagonal matrix in (3.49) is caused by the spring-mass system.

Scattering coefficients, $J = 2$

Recall that for a diametrical pair of springs there are two solutions for even and odd modes, see (3.38). The scattering coefficient for even and odd modes, respectively, is

(see (3.39))

$$(B_n^{(1)})_{\substack{e\\o}} = -\frac{2\rho c Z_{\substack{e\\o}}^{tot}}{\pi k a \zeta_n} \sum_{m\,\text{even/odd}} \frac{A_m}{\zeta_m}, \qquad \frac{1}{Z_{\substack{e\\o}}^{tot}} = \frac{1}{Z_{\substack{e\\o}}^{(J)}} + \frac{1}{Z_{\substack{e\\o}}^{sp}}. \tag{3.50}$$

In order to express the scattering coefficient vector in the succinct form

$$\mathbf{B}^{(1)} = \mathbf{b}_e \mathbf{b}_{\mathrm{e}}^T \mathbf{A} + \mathbf{b}_o \mathbf{b}_o^T \mathbf{A} \tag{3.51}$$

define the (infinite) vectors $\mathbf{b}_e$ and $\mathbf{b}_o$

$$\mathbf{b}_e = \begin{pmatrix} \vdots \\ b_{-2} \\ 0 \\ b_0 \\ 0 \\ b_2 \\ \vdots \end{pmatrix}, \quad \mathbf{b}_o = \begin{pmatrix} \vdots \\ 0 \\ b_{-1} \\ 0 \\ b_1 \\ 0 \\ \vdots \end{pmatrix}, \; (b_n)_{\substack{e\\o}} = \frac{i}{\zeta_n} \left(\frac{2\rho c Z_{\substack{e\\o}}^{tot}}{\pi k a} \right)^{1/2}. \tag{3.52}$$

Thus the T-matrix becomes

$$\mathbf{T} = \mathbf{T}^{(0)} + \mathbf{b}_e \mathbf{b}_{\mathrm{e}}^T + \mathbf{b}_o \mathbf{b}_o^T. \tag{3.53}$$

The structure of the T-matrix in (3.53) is very interesting. It means that the additional scattering above and beyond that of the shell without the spring-mass is of only two types, proportional to $\mathbf{b}_e$ or $\mathbf{b}_o$. The amplitude of each type of scattered field depends on how the incident wave couples to it, and this is given by the inner products $\mathbf{b}_{\mathrm{e}}^T \mathbf{A}$ and $\mathbf{b}_o^T \mathbf{A}$.

We note that the influence of the spring-mass enters through the two frequency dependent impedances Z_e^{sp} and Z_o^{sp}. They couple to the shell and the radiating wave impedances, Z_n^{sh} and Z_n in series via the expressions in (3.39).

Scattering coefficients, $J \geq 3$

In the general case of $J \geq 3$ springs, the scattering coefficient is (see (3.41) and (3.42))

$$B_n^{(1)} = -\frac{2\rho c Z_n^{tot}}{\pi k a \zeta_n} \sum_{p=-\infty}^{\infty} \frac{A_{n+pJ}}{\zeta_{n+pJ}}, \qquad \frac{1}{Z_n^{tot}} = \frac{1}{Z_n^{(J)}} + \frac{1}{Z_n^{sp}}. \tag{3.54}$$

Conveniently, the vector of scattering coefficients can be written as

$$\mathbf{B}^{(1)} = \mathbf{b}_1\mathbf{b}_1^T\mathbf{A} + \mathbf{b}_2\mathbf{b}_2^T\mathbf{A} + \ldots + \mathbf{b}_J\mathbf{b}_J^T\mathbf{A}, \tag{3.55}$$

where

$$\mathbf{b}_j = \begin{pmatrix} \ldots \\ b_{j,j-J} \\ \mathbf{0}_{(J-1)\times 1} \\ b_{j,j} \\ \mathbf{0}_{(J-1)\times 1} \\ b_{j,j+J} \\ \mathbf{0}_{(J-1)\times 1} \\ \ldots \end{pmatrix} \qquad b_{j,n} = \begin{cases} \frac{i}{\zeta_n}\left(\frac{2\rho c Z_n^{tot}}{\pi k a}\right)^{1/2}, & n = j \bmod J, \\ 0, & \text{otherwise.} \end{cases} \tag{3.56}$$

The full T-matrix then takes the form

$$\mathbf{T} = \mathbf{T}^{(0)} + \sum_{j=1}^{J} \mathbf{b}_j\mathbf{b}_j^T. \tag{3.57}$$

3.3 Discussion of the general solution for the shell with substructure

The structure of the derived results is well suited for numerical implementation. The contribution of the spring-mass system to the to the T-matrix of the empty shell is expressed via vectors, thereby removing the need for matrix multiplication. Also, the J sub-solutions only need to be added to produce the final response.

3.3.1 Spectral properties of the T-matrix

Let λ be an eigenvalue of the T-matrix with associated eigenvector $\mathbf{u}$, i.e.

$$\mathbf{T}\mathbf{u} = \lambda\mathbf{u}. \tag{3.58}$$

We note that the equation for λ, $\det(\mathbf{T} - \lambda\mathbf{I}) = 0$, can be expressed

$$\mathbf{b}_j^T\left(\lambda\mathbf{I} - \mathbf{T}^{(0)}\right)^{-1}\mathbf{b}_j = 1, \quad j = 1, \ldots, J. \tag{3.59}$$

In order to see this, first use (3.57) to rewrite (3.58) as

$$\mathbf{u} = \sum_{j=1}^{J}(\mathbf{b}_j^T\mathbf{u})\left(\lambda\mathbf{I} - \mathbf{T}^{(0)}\right)^{-1}\mathbf{b}_j. \tag{3.60}$$

Taking the inner product with $\mathbf{b}_i$ yields

$$\sum_{j=1}^{J} \mathbf{b}_i^T \left(\lambda \mathbf{I} - \mathbf{T}^{(0)}\right)^{-1} \mathbf{b}_j \left(\mathbf{b}_j^T \mathbf{u}\right) = \mathbf{b}_i^T \mathbf{u}. \tag{3.61}$$

This simplifies by virtue of the facts that $\lambda\mathbf{I} - \mathbf{T}^{(0)}$ is diagonal, and that, for any diagonal matrix $\mathbf{D}$, $\mathbf{b}_i^T \mathbf{D} \mathbf{b}_j = \delta_{ij}\, \mathbf{b}_j^T \mathbf{D} \mathbf{b}_j$, where δ_{ij} is the Kronecker delta and from which (3.59) follows.

Equation (3.59) implies that the eigenvalues of the T-matrix form J distinct sets, and that the eigenvectors, which follow form (3.60), are likewise separated into J families. Hence, $\mathbf{T}$ can be partitioned into J distinct T-matrices:

$$\begin{aligned} \mathbf{T} &= \sum_{j=1}^{J} \mathbf{T}^{(j)} \quad \text{where} \quad \mathbf{T}^{(j)} = \mathbf{T}^{(0)} \mathbf{I}^{(j)} + \mathbf{b}_j \mathbf{b}_j^T, \\ \mathbf{I} &= \sum_{j=1}^{J} \mathbf{I}^{(j)}, \quad \mathbf{I}^{(j)} = \operatorname{diag}\big(\ldots 1,\, \mathbf{0}_{(J-1)\times 1},\, 1,\, \mathbf{0}_{(J-1)\times 1} \ldots\big). \end{aligned} \tag{3.62}$$

Conservation of energy is ensured in each subset of modes according to

$$\mathbf{S}^{(j)^+} \mathbf{S}^{(j)} = \mathbf{S}^{(j)} \mathbf{S}^{(j)^+} = \mathbf{I}^{(j)} \quad \text{where} \quad \mathbf{S}^{(j)} = \mathbf{I}^{(j)} + 2\mathbf{T}^{(j)},\ j = 1, \ldots, J. \tag{3.63}$$

The structure of these matrices is illustrated in Figure 3.4. For instance, when $J = 2$, Figure 3.4a shows that one half of the elements of the infinite matrix are zero. The matrix is full for the case $J = 1$, and the number of zero elements increases as J becomes larger. The examples in Figure 3.4 show schematically how the fraction of non-zero elements decreases as J increases: there are always elements on the main diagonal, with the other non-zero elements becoming further separated from the main diagonal as J increases.

3.3.2 Far-field response

The far-field scattered pressure field is given in equation (3.17), where the form function g now has the form

$$g(\theta) = g^{(0)}(\theta) + g^{(1)}(\theta) = \sum_{n=-\infty}^{\infty} g_n \mathrm{e}^{in\theta}, \quad g_n = \frac{2\mathrm{e}^{-i\frac{\pi}{4}}}{\sqrt{\pi k a}} (-i)^n B_n. \tag{3.64}$$

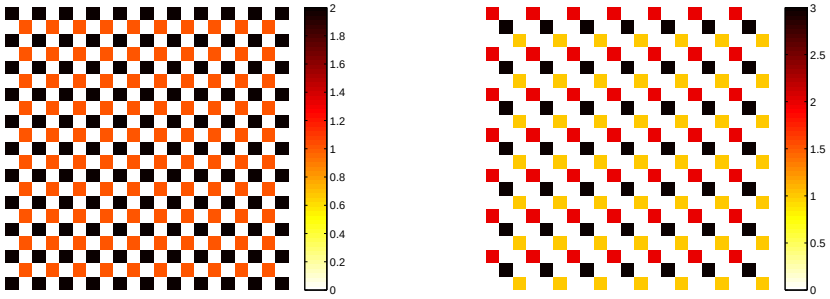

(a) J=2 (b) J=3

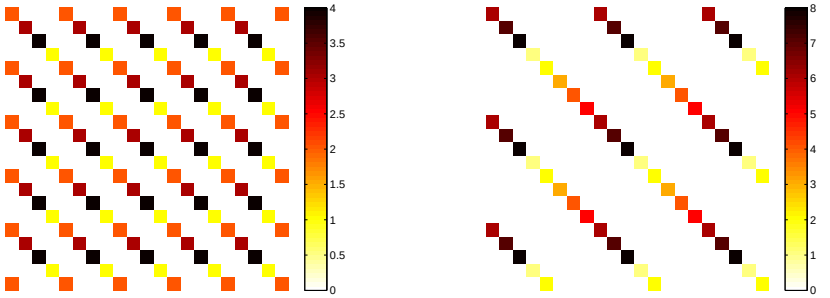

(c) J=4 (d) J=8

Figure 3.4: Structure of the matrices $\mathbf{S}^{(j)}$. Matrix elements indicated by white spaces are zero, and the other colors indicate non-zero elements of the J matrices $\mathbf{S}^{(j)}$ for $j = 1, \ldots, J$.

The form function $g^{(0)}$ is for the shell without the substructure in equation (3.18). For a plane wave incident on the shell at an angle θ_0, the scattering coefficient is $B_n = \sum_{m=-\infty}^{\infty} T_{nm} A_m$ where $A_m = (-i)^m \mathrm{e}^{-im\theta_0}$. This allows us to write the far-field form function as (see (3.15) for T_n)

$$g_n = \frac{2\mathrm{e}^{-i\frac{\pi}{4}}}{\sqrt{\pi ka}} \sum_{m=-\infty}^{\infty} (-i)^{n+m} \mathrm{e}^{-im\theta_0} \times \begin{cases} \big(\delta_{nm} T_m + b_n b_m\big), & J = 1, \\ \big(\delta_{nm} T_m + b_n^{(e)} b_m^{(e)} + b_n^{(o)} b_m^{(o)}\big), & J = 2, \\ \big(\delta_{nm} T_m + \sum_{j=1}^{J} b_{j,n} b_{j,m}\big), & J \geq 3, \end{cases} \tag{3.65}$$

where δ_{nm} is the Kronecker delta.

The total scattering cross section (TSCS) σ_{tot} is defined as

$$\sigma_{tot} = \frac{1}{2} \int_0^{2\pi} |g(\theta)|^2 d\theta = \frac{4}{ka} \sum_{n=-\infty}^{\infty} |B_n|^2, \quad \text{and} \quad \sigma_{tot}^{(0)} = \frac{4}{ka} \sum_{n=-\infty}^{\infty} |B_n^{(0)}|^2, \tag{3.66}$$

where $\sigma_{tot}^{(0)}$ is TSCS for the empty shell as in equation (3.19).

3.4 Numerical example 1: steel shell with an internal substructure

Consider a steel shell ($\rho_s = 7810$ kg/m^3, $c_p = 5505$ m/s) immersed in water ($\rho = 1000$ kg/m^3, $c = 1484$ m/s). Shell thickness to radius ratio is $\frac{h}{a} = \frac{1}{100}$. We define the internal mass to shell mass ratio as $\frac{m}{2\pi\rho_s h a} = 3$. The spring stiffness is assumed to be such that the resonance frequency of the oscillator satisfies (see (3.23) for H_J)

$$\frac{\kappa}{m}\frac{a^2}{c^2} = \frac{1}{H_J} \quad \Longrightarrow \quad \kappa = \frac{m}{a^2}\frac{c^2}{H_J}, \tag{3.67}$$

which gives $k_{sp}a \equiv \sqrt{H_J}\frac{\omega_{sp}a}{c} = 1 \; \forall J$.

Figures 3.5, 3.6, and 3.7 show the backscatter $g(\theta_0)$, total impedance $|Z^{tot}|$ and its phase for $J = 1, 2, 3$, respectively. The angle of incidence is taken to be $\theta_0 = 0$ and the truncation limit is $N = 100$.

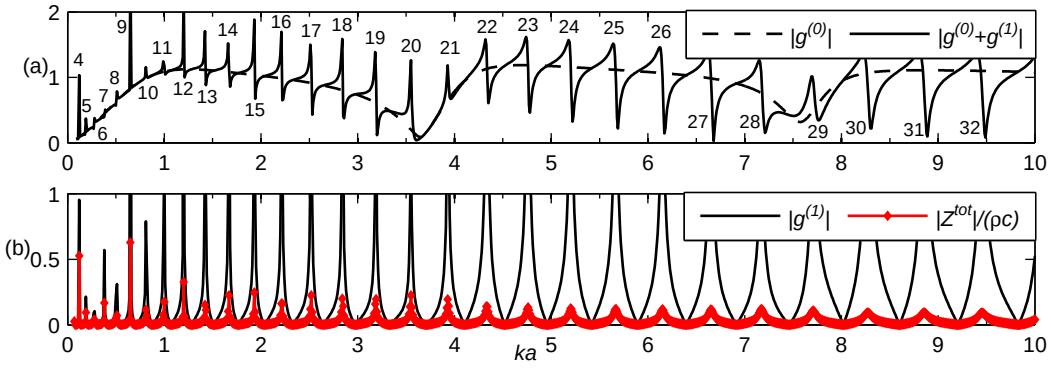

Figure 3.5: Backscatter and total impedance as a function of ka for $J = 1$ and incident angle $\theta_0 = 0$. The dashed line in plot (a) is the backscatter for the empty shell. In plot (b), the backscatter due to the presence of the spring-mass system $g^{(1)}$ has the same resonances as the total impedance Z^{tot}. The small numbers over the resonances indicate the flexural mode.

With a single spring attaching the internal mass to the shell (Figure 3.5) the backscatter is close to that of the empty shell but with many resonances. We show in §3.4.1 that the resonance peaks are associated with flexural modes on the shell excited by the structural discontinuity caused by the spring attachments. The backscatter

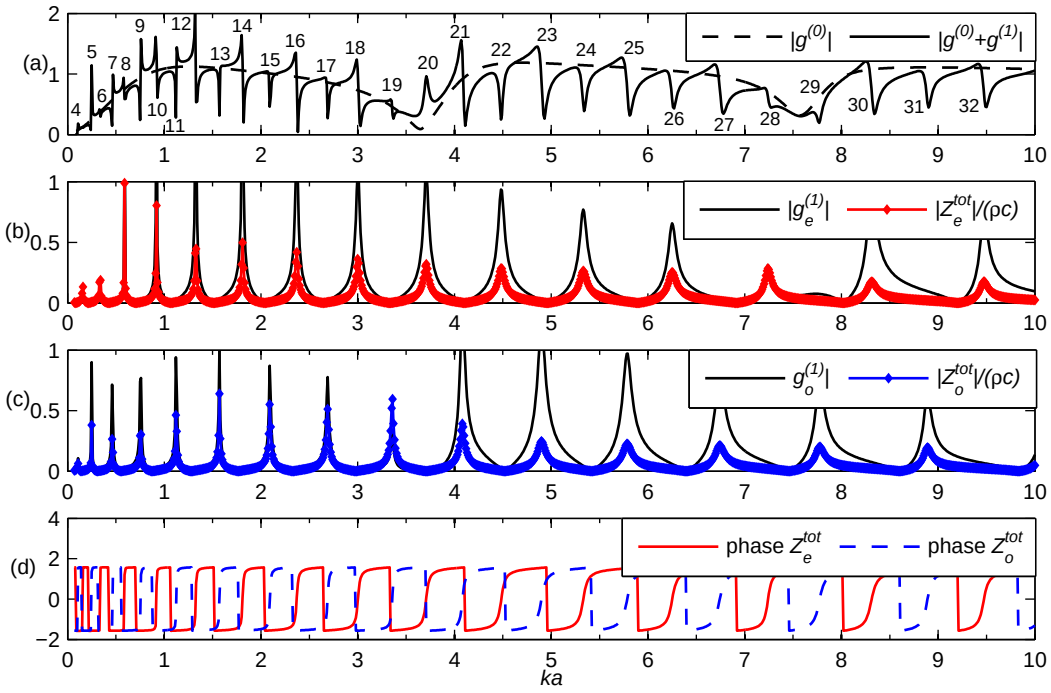

Figure 3.6: Backscatter, total impedance and its phase as a function of ka for $J = 2$, $\theta_0 = 0$. The dashed line in plot (a) is the backscatter for the empty shell. The backscatter due to the even and odd solutions are plotted separately in plots (b) and (c), respectively. The phase of the total impedance is shown in figure (d). The small numbers over the resonances indicate the flexural mode.

becomes more complex as the number of springs increases. For $J = 2$ springs, the sub-solutions of the form function are plotted below the total response in Figure 3.6. It is evident that half of the resonance peaks come from the even solution and the other half from the odd. At each resonance, the magnitude of the total impedance $|Z_{e}^{tot}_{o}|$ is at a maximum and its phase is zero. This implies that the position and spacing of the resonances can be determined from the total impedance Z^{tot}, which is explored further below in §3.4.1. The backscatter from the shell with $J = 2$ springs in Figure 3.6(a), which was obtained using the general solution (equations (3.18) and (3.65)), is identical to Figure 3(a) in Ref. [33].

The case of $J = 3$ springs in Figure 3.7 displays a new feature not previously

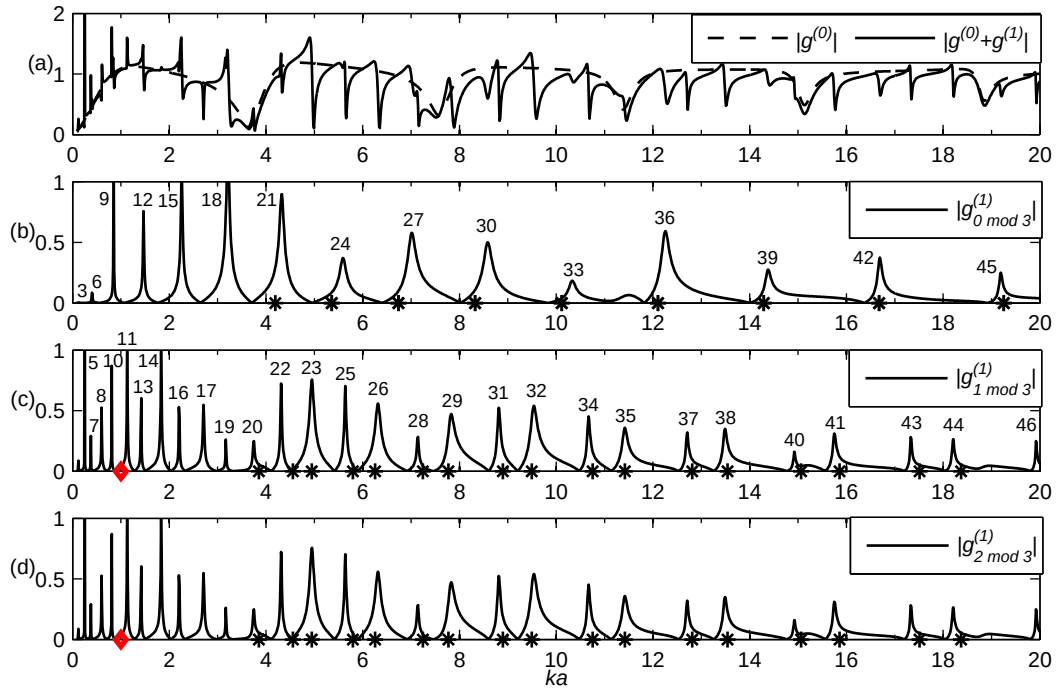

Figure 3.7: Backscatter as a function of ka for $J = 3$, $\theta_0 = 0$. The dashed line in the plot (a) is the backscatter for the empty shell. Plots (b), (c), and (d) show the backscatter for the three subsolutions. The red diamond on the horizontal axis indicates the resonance frequency of the spring-mass system $k_{sp}a = 1$. The black stars are the resonances of the shell-spring-mass system as predicted by equation (3.73). The small numbers over the resonances indicate the flexural mode.

evident for $J = 1$ and $J = 2$: viz. the $1 \bmod 3$ solution and the $2 \bmod 3$ solution are identical. The repetition is a consequence of (i) the symmetries of the four impedances of equation (3.23) under the interchange $n \to -n$, and (ii) the fact that the integer sets $1 \bmod 3$ and $2 \bmod 3$ are identical under a change of sign, i.e. $\{\ldots -5, -2, 1, 4, \ldots\} \leftrightarrow \{\ldots -4, -1, 2, 5, \ldots\}$. These properties together ensure that the impedance Z_n^{tot} is also unchanged under $n \to -n$, and hence cause the repetition seen in Figure 3.7. It follows that for any $J \geq 1$ the J parts of the $T-$matrix actually reduce to $1 + \lfloor \frac{J}{2} \rfloor$ distinct parts, where $\lfloor \cdot \rfloor$ is the floor function.

3.4.1 Resonant behavior of the shell-spring-mass system

As noted above for the cases with $J = 1$, $J = 2$ and $J = 3$ springs, the resonant behavior of shell-spring-mass system in Figures 3.5-3.7 arise from singularities of Z^{tot} lying close to the real ka-axis. Thus, at resonance, from equation (3.26),

$$\frac{1}{Z_n^{sp}} + \sum_{p=-\infty}^{\infty} \frac{1}{Z_{n+pJ}^{sh} + Z_{n+pJ}} = \epsilon, \quad |\epsilon| \ll 1. \tag{3.68}$$

We consider the spring-mass systems of the above numerical examples, for which the resonances are in the range $ka \gg 1$, and in particular, above the spring resonance frequency. The spring impedance is then (see 3.42)

$$Z_n^{sp} \approx \frac{i}{(ka)} \frac{J\kappa}{2\pi c}, \quad ka \gg 1. \tag{3.69}$$

This is independent of n, and it's inverse is large, O(ka). We therefore assume that the condition (3.68) is satisfied by one of the terms in the infinite series becoming large relative to all others, in which case the condition reduces to

$$Z_n^{sp} + Z_n^{sh} + Z_n \approx 0, \tag{3.70}$$

for some n and a related frequency ka. The resonances of the combined system are determined by approximating the individual impedances in (3.70). To get an expression for the effective resonance frequencies of the combined system, the acoustic impedance is approximated as

$$Z_n \approx -i\rho c \frac{ka}{n}, \quad n \gg ka, \quad n \neq 0. \tag{3.71}$$

The roots of the shell impedance Z_n^{sh} of (3.23b), which correspond to the natural frequencies of the shell, are $\Omega_{r,c}^2 = ((1 + n^2 + \beta^2 n^4) \mp \sqrt{(1 + n^2 + \beta^2 n^4)^2 - 4\beta^2 n^6})/2$ associated with flexural and circumferential modes, respectively (an equivalent form of equation (3.8)). The thin shell approximation implies $\beta \ll 1$, consequently the resonance frequencies are $(\Omega_r, \Omega_c) \approx (\beta n^3/\sqrt{n^2+1}, \sqrt{n^2+1})$ while $\beta n < 1$. Since $\Omega_c \approx n$, the shell impedance behaves as

$$Z_n^{sh} \approx -i\rho_s c_p \frac{h}{a} \left(\Omega - \frac{\Omega_r^2}{\Omega} \right) \quad \text{where} \quad \Omega_r \approx \beta n^2 \tag{3.72}$$

is the flexural natural frequency.

The condition of resonance given by (3.70), combined with equations (3.69), (3.71) and (3.72), now results in a quadratic equation for the resonance frequencies $k_{res}a = \frac{c_p}{c}\Omega_{res}$. Solving the equation yields

$$\Omega_{res}^2 = \frac{\beta^2 n^4 + \frac{J\kappa}{2\pi\rho_s c_p^2}\frac{a}{h}}{1 + \frac{1}{n}\frac{\rho}{\rho_s}\frac{a}{h}}, \qquad k_{sp}a < k_{res}a \ll n. \tag{3.73}$$

The resonance can therefore be interpreted as, to leading order, the flexural resonance at $\Omega = \Omega_r$ (see (3.72)) modified by an added mass term in the denominator which accounts for the fluid mass-loading (the same factor is present in equation 9.4 on page 282 of the text by Junger & Feit [44] for a fluid-loaded spherical shell), and by an additional stiffness term in the numerator associated with the stiffness of the springs. Note that the flexural resonances are *not* excited by the smooth shell (see Figure 3.5) because they are sub-sonic and hence do not couple with the incident field. The coupling to the quasi-flexural waves occurs directly because of the introduction of structural discontinuities at the spring-shell attachment points. These act as sources for the flexural waves which, in turn, radiate to the exterior fluid via the same discontinuities.

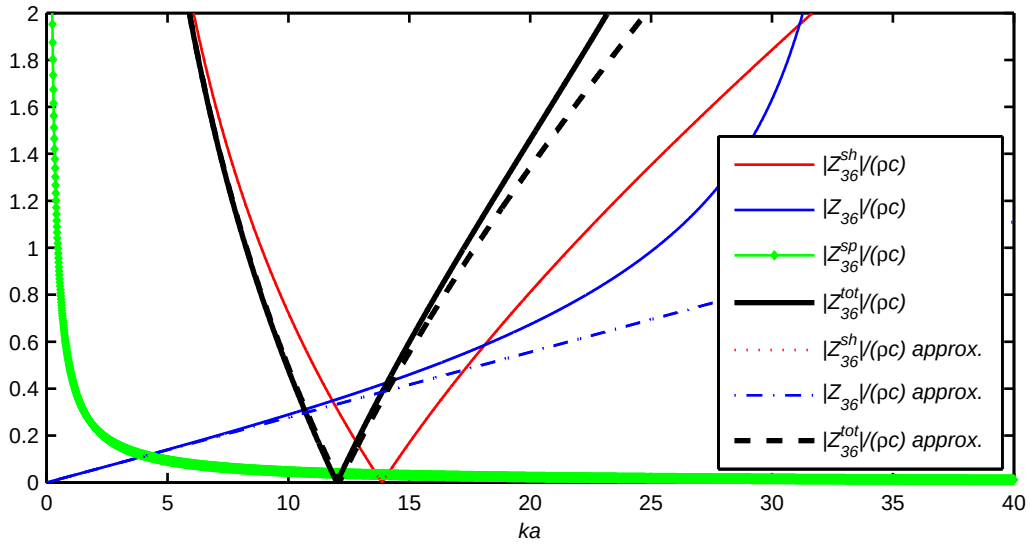

Figure 3.8: Comparison of impedances for mode n=36. This corresponds to the resonance near $ka = 12$ of Figure 3.7. The solid lines are the exact impedances while the dashed lines are approximations.

The various approximations leading to the expression for the resonance frequency are verified in Figure 3.8 which shows the approximate impedances plotted along with the exact impedances. The curves are very close as long as $n \gg ka$. At larger frequencies this condition is violated and the expression for the effective frequencies, equation (3.73) is no longer accurate. However, the spring impedance $Z_n^{sp} \sim O(1/(ka))$ and hence its effect at larger frequencies is negligible. The effective resonances are plotted on the horizontal axis for the $J = 3$ case in Figure 3.7. Although, the values are close to the resonances of the combined system they are not exact. This is primarily because we only take a single term from the summation of Z_n^{tot} when formulating the condition of resonance (see equation (3.68) and equation (3.70)).

3.4.2 Large J limit

As the number of springs J increases, the loading on the shell transitions from discrete point forces to an effective pressure at the frequencies of interest $ka \leq 20$. However, unlike a fluid filled shell where there is also a pressure distribution over the inner surface, in this idealized model the internal structure has an infinite wave velocity since the transfer of energy from one contact point on the shell to the other is instantaneous. Figure 3.9 plots the total scattering cross section for the same shell but with increasing number of springs $J = 2, 4, 8, 16, 32$ at the angle of incidence $\theta_0 = 0$. Since the resonance frequency of the oscillator is kept constant (see equation (3.67)), the stiffness of each spring has to decrease with increasing J. This allows us to investigate solely the affect of increasing the number of contact points.

In general, Figure 3.9 shows that increasing the number of contact points results in a decrease in the number of flexural resonances propagating into the far-field. This is due to the presence of forces at anti-nodes of flexural modes which inhibit their vibration. Only the response for even numbers of springs is plotted and hence the odd modes are prominent as J increases. For $J = 16$ and $J = 32$, large intervals appear without flexural resonances, however, the TSCS is slightly increased over the empty shell (shown by the dashed line) due to the added stiffness and mass. The low frequency TSCS is asymptotically zero for these two cases because the effective quasi-static properties of

the shell-spring-mass system are water-like. For the case with $J = 32$ springs there are only a few large resonances near the resonance frequency of the oscillator $k_{sp}a = 1$, the $n = 9$ and $n = 11$ flexural modes.

As J approaches infinity no flexural modes will be visible in the far-field with the exception of the closest ones to the springs-mass resonance. The mechanically equivalent system as $J \to \infty$ is one of a highly anisotropic medium, with zero azimuthal stiffness and infinite wave speed in the radial direction. The latter is a result of ignoring the spring mass; this could be included but is beyond the goals of the present analysis which is aimed at the low to moderate frequency regime.

3.4.3 Angle of incidence

The discrete number of attachment points on the shell produces symmetries which couple to the angle of incidence. The J springs are distributed axisymmetrically, therefore only angles of incidence in the range $\theta_0 = [0, \pi/J]$ produce unique results for even J. Figure 3.10 presents the total scattering cross section (TSCS) for several distributions of springs. The dashed line represents the TSCS of the empty shell.

For the $J = 2$ case in plot (a) we observe a decrease in the amplitude and the number of peaks as the angle of incidence goes from 0 to $\pi/2$. This is because only the even flexural modes are unconstrained by the springs when the plane wave is perpendicular to the pair as described by [33]. Analysing larger numbers of springs, it has been determined that such clear separation of response also occurs for $J = 4$ springs in plot (c). Furthermore, for $J = 2$ springs, as the angle of incidence is changed from 0 to $\pi/4$, the asymmetric profile of the flexural resonances flips due to a relative phase between the shell-spring-mass system and the surrounding water. In the new results with $J = 3$ springs all flexural modes propagate into the far-field regardless of the angle of incidence. The TSCS for $\theta_0 = 0$ is identical to that of $\theta_0 = \pi/3$ because both coincide with the orientation of exactly one of the springs.

The TSCS for $J = 4$ springs is shown in plot (c) of Figure 3.10. Again, the total number of peaks is halved as compared to the $J = 2$ case due to the fact that the 4 springs exactly coincide with the anti-nodes of the even flexural modes. Thus the shell

stiffened with $J = 4$ springs vibrates mostly with odd modes. Because different modes are affected differently by the substructure, certain even modes fall near an excited odd mode and are consequently enhanced. The resulting resonance is no longer sharp, but has a plateau-like form as seen at $ka = 7.7$ and $ka = 8.7$ for the $n = 28, 29$ and $n = 30, 31$ mode pairs, respectively. For $J = 8$ springs we see that the low frequency flexural modes are unaffected by the angle of incidence, but the higher modes are affected. For example the $n = 26$ flexural mode at $ka = 6.28$ is not exited with $\theta_0 = 0$ but is clearly visible at $\theta_0 = \pi/16$ and $\pi/8$.

3.5 Numerical example 2: acoustically transparent aluminum shell

Consider a thin shell made of aluminum 3003-H18 ($\rho_s = 2730$ kg/m^3, $c_p = 5326$ m/s). Matching the effective properties of the shell-springs-mass system to water implies $K_{eff} = K$ and $\rho_{eff} = \rho$. The resonance frequency of the internal spring-mass system ω_{sp} can be expressed in terms of the density and bulk modulus of the effective medium as

$$\omega_{sp}^2 = H_J \tan\left(\frac{\pi}{J}\right) \frac{4}{\pi a^2} \left(\frac{K_{eff} - \frac{h}{a} K_{sh}}{\rho_{eff} - 2\frac{h}{a}\rho_s} \right). \tag{3.74}$$

In the case of odd J, $\tan(\pi/J)$ should be replaced by $2\tan(\pi/(2J))$ which has the same limit for large J, as expected. A necessary condition for low frequency transparency is that this internal resonance lie above the low-frequency range, here considered as roughly $0 < ka < 0.5$. Figure 3.11 plots the non-dimensional resonance wavenumber $k_{sp}a = \omega_{sp}/c$ as a function of shell thickness ratio for several numbers of distributed springs J. As the shell thickness decreases, the resonance frequency of the internal oscillator increases at a diminishing rate. Equivalently, as the shell becomes thinner the added stiffness must increase faster than the mass. Also note that the resonance frequency drops as the number of springs, J, increases. This is due to the factor $H_J \tan(\pi/J)$ in equation (3.74).

From Figure 3.11 as well as Table 2.1 we see that the upper bound on shell thickness is $h/a = 0.055$. Since aluminum is relatively light there is a substantial mass deficiency $\rho_m = 0.68\rho$ at that thickness. In order to tune the shell to water, a central mass is added.

However, the mass has to be supported by springs, therefore the shell must be thinner than the upper bound to accommodate the additional stiffness, namely $h/a = 0.03$. From equations (2.31) and (2.32), the added stiffness must be $K_{sp} = 0.52K$ and the added density $\rho_m = 0.84\rho$.

3.5.1 Flexural resonances

The scattering response of the tuned shell is analyzed for plane wave incidence. Figure 3.12a shows the TSCS of equation (3.19) as a function of ka for the three cases in Figure 3.11 at the thickness ratio $h/a = 0.03$. The star on the horizontal axis indicates the resonance frequency of the springs-mass system, which per previous discussion decreases with J. For $J = 4$ and $J = 8$ springs the tuning is only effective at extremely low frequencies, because of the presence of several flexural resonances. However with $J = 16$ springs the TSCS is close to zero at frequencies up to $ka = 0.8$, where the magnified view is shown in Figure 3.12b. By further increasing the number of springs, the transparent region increases only slightly, because it is bounded by the resonance frequency of the oscillator which for large J is at about $k_{sp}a = \omega_{sp}a/c = 0.95$ (see equation (3.74)).

The shell thickness of $h/a = 0.03$ is the optimal shell thickness, because it maximizes the range of frequencies of low TSCS. At the optimal thickness the lowest resonance of the combined acoustic and shell impedances $\big(\sum_{p=-\infty}^{\infty} 1/(Z^{sh}_{n+pJ} + Z_{n+pJ})\big)^{-1}$ coincides with the resonance frequency of the oscillator Z^{sp}_n. The result is that there is a large region free from flexural resonances but still close enough to the oscillator resonance for it to be effective.

The reason for the decrease in the number of flexural resonances with increasing J can be understood by considering the radial displacement of the shell $w(\theta)$ at each resonance. These are plotted in Figure 3.13, where indeed each resonance corresponds to a certain flexural mode. The red radial lines indicate the positions of the springs. From these we can conclude that as the number of springs J increases more flexural modes are constrained by the springs. The modes that do appear are either modes where the spring attachments coincide with the anti-nodes of the radial displacement

or if the mode is odd, the displacement is anti-symmetric.

Note that although we can attribute each resonance peak to a flexural mode, the position of the peak is difficult to predict in the low frequency range, see Ref. [102] for further details.

3.5.2 Acrylic substructure

The analytical model demonstrates the theoretical possibility of tuning elastic shells. Next, the two physical oscillator designs in Figure 2.8 will be considered. The TSCS is determined in COMSOL by simulating plane wave incidence onto the tuned shell and integrating the far-field scattered pressure over a closed contour (see equation (3.19)). The mesh is selected such that the largest elements do not exceed one sixths of the shortest wavelength, the shear wave in acrylic (see Table 2.1 for the shear speed). To prevent artificial scattering from domain boundaries a cylindrical radiation condition is used.

Figure 3.14 shows the TSCS for the two oscillator designs described by equations 2.39 and 2.40 (see Figure 2.8) as well as the analytical springs-mass solution of Figure 3.12b and that for the empty shell. The presence of the oscillator significantly decreases the scattered power at low frequencies. The TSCS is effectively zero at frequencies below $ka = 0.6$ making the shell transparent in water. The acrylic substructure with the central rod gives the broadest region of negligible scattering. The accuracy of the analytical springs-mass solution versus the finite element results of an acrylic oscillator is quite remarkable.

Aside from being acoustically transparent, the internal spring-mass system can be used to purposely introduce a strong local resonance in an array of such shells. This resonance could also be spatially varying by appropriately selecting the number of stiffeners J.

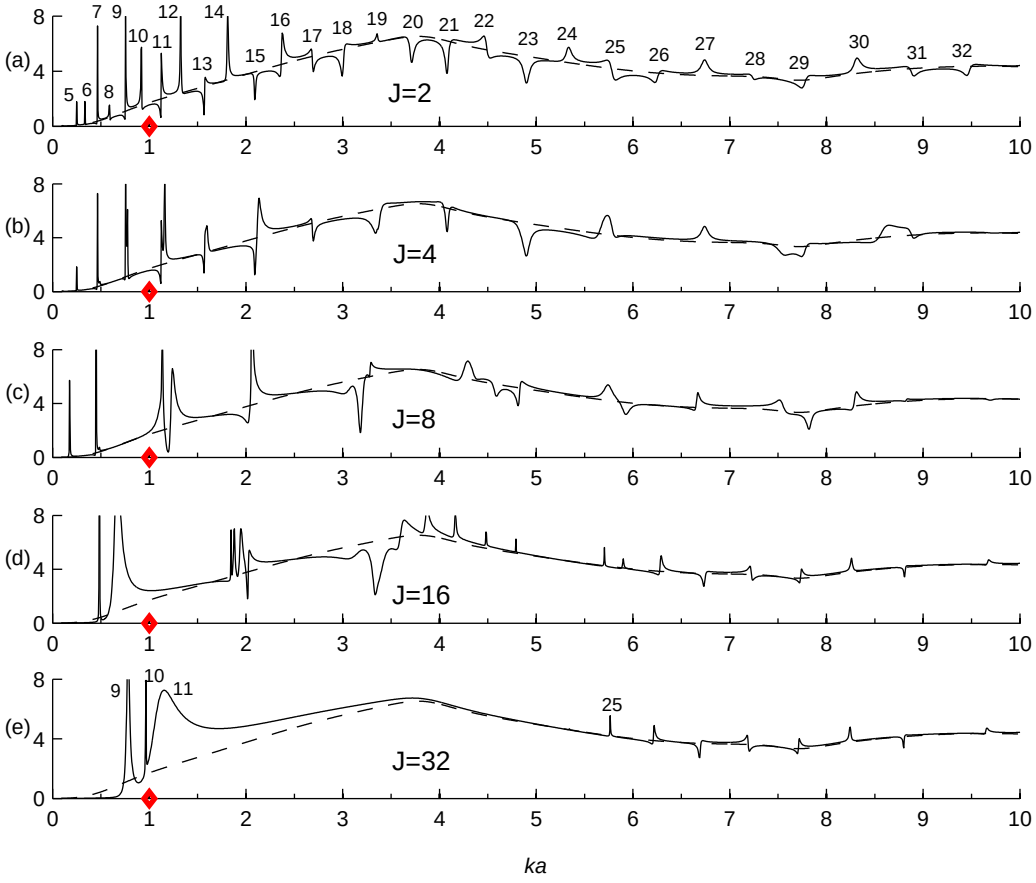

Figure 3.9: Total scattering cross section as defined in equation (3.66) for $J = 2, 4, 8, 16, 32$ springs at the angle of incidence $\theta_0 = 0$ in plots (a), (b), (c), (d), (e), respectively. The dashed line in all plots is the TSCS for the empty shell. The red diamonds on the horizontal axis indicate the constant resonance frequency of the spring-mass system $k_{sp}a = 1$. The small numbers over the resonances indicate the flexural mode.

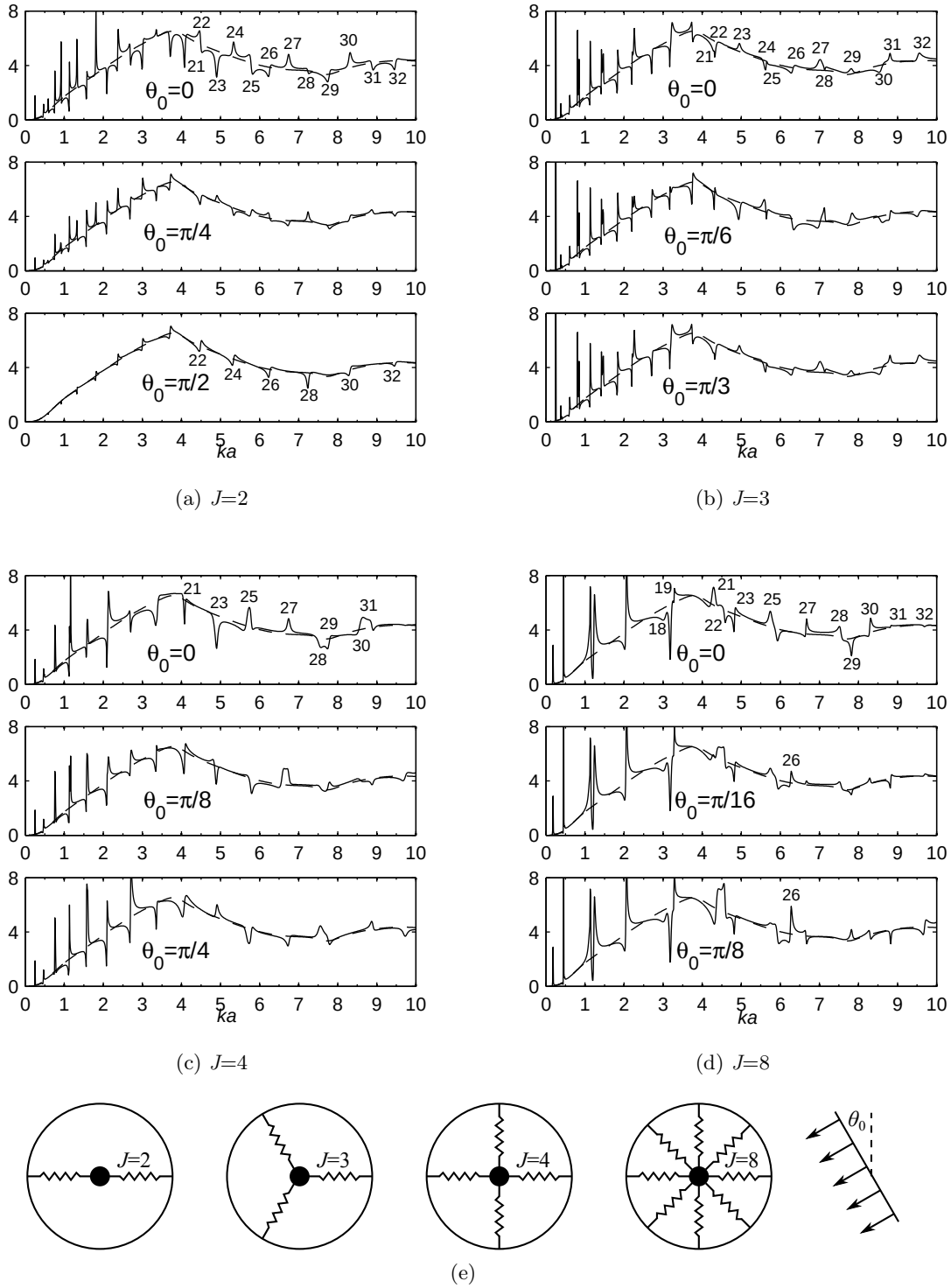

(a) J=2 (b) J=3

(c) J=4 (d) J=8

(e)

Figure 3.10: Total scattering cross section as defined in equation (3.66) for $J = 2, 3, 4, 8$ as a function of the plane wave angle of incidence, θ_0. The dashed curve is the total scattering cross section of the empty shell. The spring orientations relative to the incoming wave are shown in figure (e). The spring resonance frequency is $k_{sp}a = 1$ in all cases. The small numbers over the resonances indicate the flexural mode.

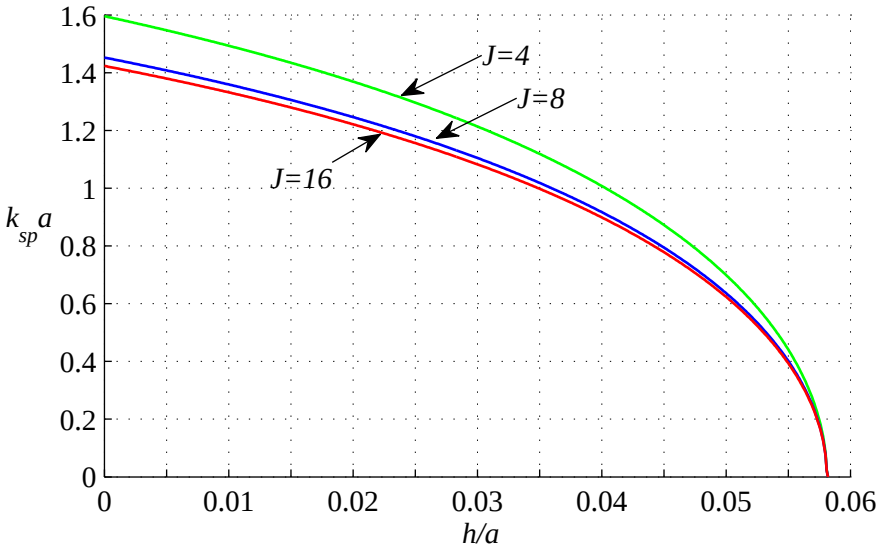

Figure 3.11: Non-dimensional resonance wavenumber $k_{sp}a = \omega_{sp}a/c$ of the internal springs-mass system as a function of shell thickness (see equation (3.74)). The aluminum shell is tuned to water.

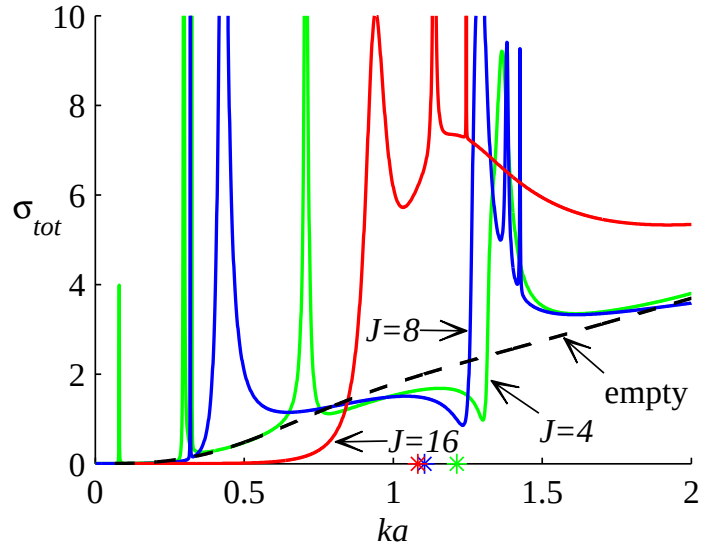

(a)

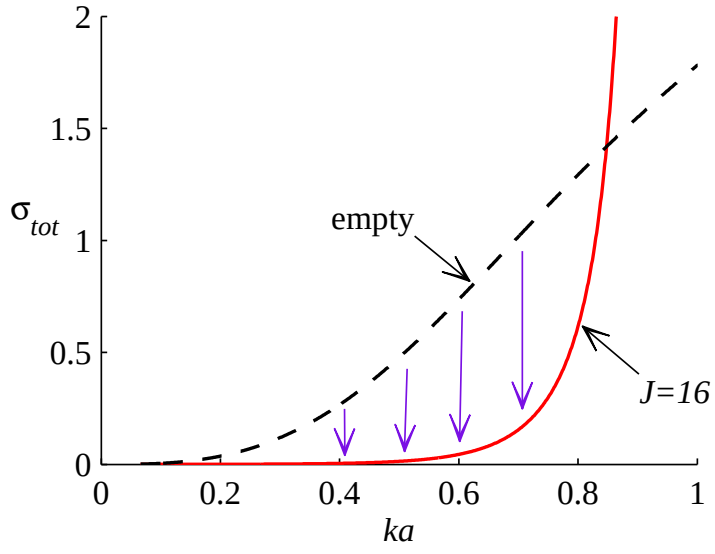

(b)

Figure 3.12: Plot (a) shows the total scattering cross section for an aluminium shell of thickness $h/a = 0.03$ with $J = 4, 8, 16$ springs supporting a central mass. The dashed line is the TSCS of the empty shell. Plot (b) is a close up of plot (a) showing the achieved decrease in the scattering cross section from an empty shell to a tuned shell with $J = 16$ springs.

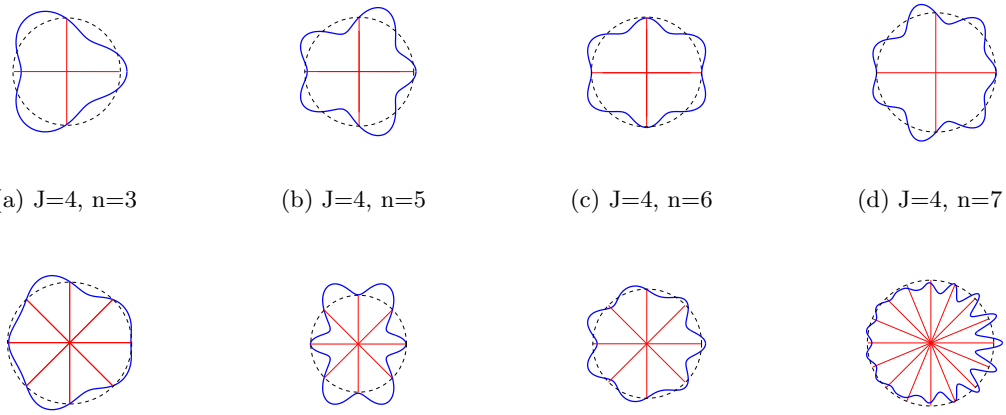

(a) J=4, n=3 (b) J=4, n=5 (c) J=4, n=6 (d) J=4, n=7

(e) J=8, n=5 (f) J=8, n=6 (g) J=8, n=7 (h) J=16, n=15

Figure 3.13: Radial displacement $w(\theta)$ for the $J = 4$ case at resonance frequencies: $ka = 0.081, 0.303, 0.338, 0.74$ in (a), (b), (c) and (d), respectively. Plots (e), (f) and (g) show the radial displacement $w(\theta)$ for the case with $J = 8$ springs at resonance frequencies: $ka = 0.273, 0.321, 0.434$, respectively. Plot (h) is the radial displacement for $J = 16$ springs at the resonance frequency of $ka = 0.945$. The radial lines depict the internal springs. The thickness of the aluminum shell is $h/a = 0.03$. Displacement has been arbitrarily scaled for clear depiction of the mode shape.

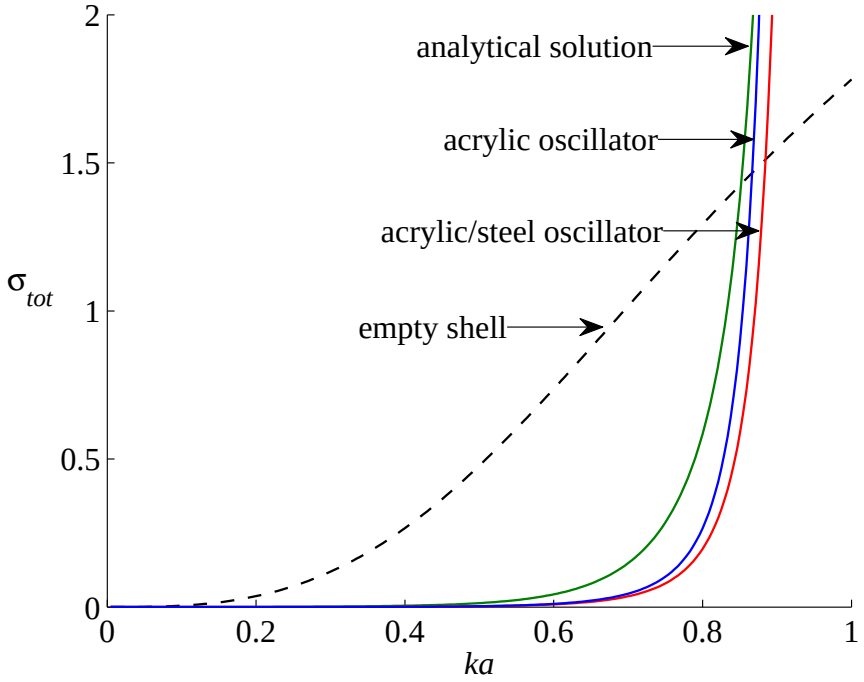

Figure 3.14: Total scattering cross section of the two acoustically transparent aluminum shells with an internal acrylic oscillator shown in Figure 3.14.

Chapter 4

Tuned shells as elements in acoustic metamaterials

Transformation based design of materials for wave steering originated in electromagnetics. Using singular transformations and the invariance of Maxwell's equations under such transformations the possibility of wave steering was demonstrated [75]. The idea of cloaking is to steer an incident wave in a finite region surrounding the object such that there is no scattering. Although the theory is frequency independent, only cloaking of objects at microwave frequencies has been achieved experimentally [90]. Cloaking objects at frequencies of visible light is theoretically possible using conformal mapping as shown by Leonhardt [55], but is experimentally unconfirmed. Other applications of transformation optics include beam shifters and splitters [69] and carpet cloaks [57] .

By natural progression the ideas found applications in acoustics. Cummer et al. [17] showed the equivalent invariance under coordinate transformations between Maxwell's and Helmholtz' equations. Using singular transformations they designed a 2D acoustic cloak with anisotropic density and bulk modulus. Simulations showed that the cloak could steer waves around the annulus. Chen and Chan [12] applied the same concept to the design of a 3D acoustic cloak. Cloaking of elastodynamic waves was also investigated [66].

One way to achieve the anisotropic density required for inertial cloaking is by use of layered fluids [105, 73]. However, such cloaking devices are not viable because the density requirement results in an infinitely massive cloak [70]. Urzhumov et al. [108] attempted to improve cloaks based on layering fluids to include solids. They concluded that the added shear waves in the solid layers do not alter the cloaking effect for nearly incompressible materials, with Poisson's ratio $\nu > 0.49$, such as rubber. There has also been interest in designing acoustically cloaked sensors via elastic shells [32, 37, 31].

An analogous problem to hiding an object surrounded by a wave medium is to do so on a surface. The resulting carpet cloak as it is called transforms a finite region between the object and the external medium to one that would yield the same scattering as from the back surface. Carpet cloaks were initially investigated for electromagnetic waves [57, 109]. There have also been several experimental studies of acoustic carpet cloaks [82, 81, 114]. The acoustic carpet cloak in air was achieved with layered perforated plastic plates which gave the necessary anisotropic properties.

A sonic crystal (SC) is capable of filtering, guiding and/or steering an incident wave based on a gradient of effective properties [13, 68, 11, 58, 60, 15, 86, 59]. SCs originated as the acoustic analog of the early photonic crystals of Yablonovitch [111] and John [43] which exhibited opaqueness at certain frequencies. The scatter is the fundamental element of the SC and is responsible for the behaviour of the complete array, which may present a compounding effect of the individual elements. For an air-based SC, the scatterer can be modelled as rigid [89, 103, 86]. Therefore, for a two dimensional air-based SC the design parameters are the scatterers' size, geometry, spacing and lattice structure. For water-based SC the elasticity of the scatter is not only non-negligible, but essential in the modelling of such structures.

The transformation acoustics example which will be discussed here is the cylindrical-to-plane wave lens as designed by Layman et al. [53]. It works by steering waves, due to a monopole source at the center, from the corners to the faces of the lens. The SC of Ref. [53] is based on constructive multiple scattering from finite embedded elastic materials in a fluid matrix, something previously investigated by Torrent and Sanchez-Dehesa [104]. This Chapter expands the possibilities in Ref. [104] by increasing the range of achievable properties over those presented by Martin et al. [65].

This Chapter is organized as follows. The conformal mapping which yields the required distribution of properties for a cylindrical-to-plane wave lens is formulated in § 4.1.1. A realization of this lens design with internally tuned shells is presented in § 4.1.2. An alternative design is presented in § 4.1.3, which uses readily available empty shells. An active control mechanism for tuning the effective properties of the shell is presented in § 4.2 an applied to an active radial array.

4.1 Cylindrical-to-plane wave lens

Refraction based wave steering lenses are an efficient way of steering an incident wave. Snell's Law dictates that if a wave enters an isotropic medium with a different sound speed, then the wave will be refracted according to

$$\frac{\sin\theta_1}{\sin\theta_2} = \frac{c_1}{c_2}, \tag{4.1}$$

where θ_1, θ_2 are the incident and refracted wave angles, respectively, and c_1, c_2 are the respective wave speeds. Full control of incident sound can be achieved with a two dimensional distribution of effective properties. However, the resulting medium must also have a high transmittance in order to be useful. An efficient cylindrical-to-plane wave lens depends on the accurate distribution of the properties via the conformal map described next.

4.1.1 Distribution of properties

The wave equation for an acoustic medium is invariant under coordinate transformations. Moreover, if the transformation $\gamma = x + iy \to s = x' + iy'$ is conformal, $s = s(\gamma)$, then the mapped density ρ' and bulk modulus K' in the transformed coordinates are [72]

$$\rho' = \rho, \qquad K' = K|ds/d\gamma|. \tag{4.2}$$

Consider the conformal transformation of a unit γ circle to a unit s square. The circle is first mapped to the upper half plane through a bilinear transformation; the subsequent polygon mapping takes the upper half plane to the unit square in s. The resulting unit square to unit circle inverse mapping is

$$\gamma = \frac{1-\chi}{1+\chi}\mathrm{e}^{-i\pi/4}, \tag{4.3a}$$

$$\chi = i\,\mathrm{cn}^2\left(\frac{1}{2}\mathbf{K}\left(\frac{1}{\sqrt{2}}\right)(s+1+i)\right), \tag{4.3b}$$

where $\mathbf{K}()$ is the complete elliptic integral of the first kind and $\mathrm{cn}(u)$ is the Jacobi elliptic function. The bulk modulus distribution in the transformed space is

$$K' = \frac{2K}{\mathbf{K}(\frac{1}{\sqrt{2}})\sqrt{\gamma^4+1}}. \tag{4.4}$$

It should be noted the elliptic integral is singular at the corners of the square region.

The distribution (4.4) is used to design a cylindrical-to-plane wave lens. The complex variable defining the square is $\{s(x+iy)|x,y:-L/2,L/2\}$. Substituting s into (4.3) and then the obtained γ into (4.4) gives the continuous function of the bulk modulus distribution. In order for the distribution to be applicable to an array of sub-wavelength scatterers it has to be discretized. This is done by averaging the value of the bulk modulus over a square unit cell of the array. Having used the notation K_{eff} for the effective bulk modulus of the shell, denote the bulk modulus of a unit cell as K_{eq}. As an example, the normalized bulk modulus distribution is discretized into 7 by 7 cells as in Figure 4.1b.

(a)

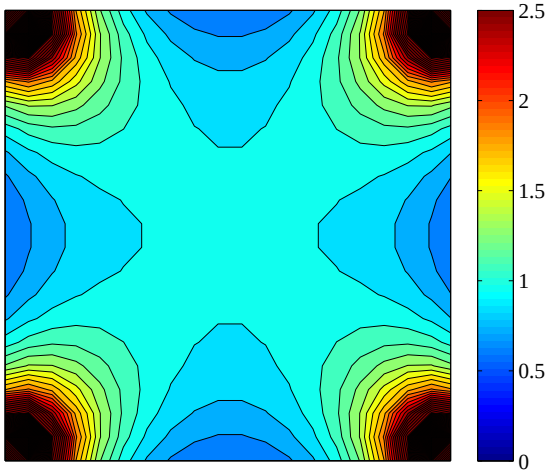

(b)

2.3	1.24	0.92	0.84	0.92	1.24	2.3
1.24	1.12	0.99	0.95	0.99	1.12	1.24
0.92	0.99	0.99	0.98	0.99	0.99	0.92
0.84	0.95	0.98	0.98	0.98	0.95	0.84
0.92	0.99	0.99	0.98	0.99	0.99	0.92
1.24	1.12	0.99	0.95	0.99	1.12	1.24
2.3	1.24	0.92	0.84	0.92	1.24	2.3

Figure 4.1: Plot (a) shows the continuous bulk modulus distribution K_{eq}/K. Plot (b) show the same function discretized into 7x7 cells.

4.1.2 Realization with internally tuned shells

The unit cell of the square array, shown in Figure 4.2a, consists of a shell with an internal acrylic substructure surrounded by a square region of water. The shell volume fraction in the unit cell is $f_s = \pi a^2/b^2$, where b is the cylinder spacing as well as the side length of the unit cell. The equivalent density and bulk modulus, ρ_{eq}, K_{eq}, of the

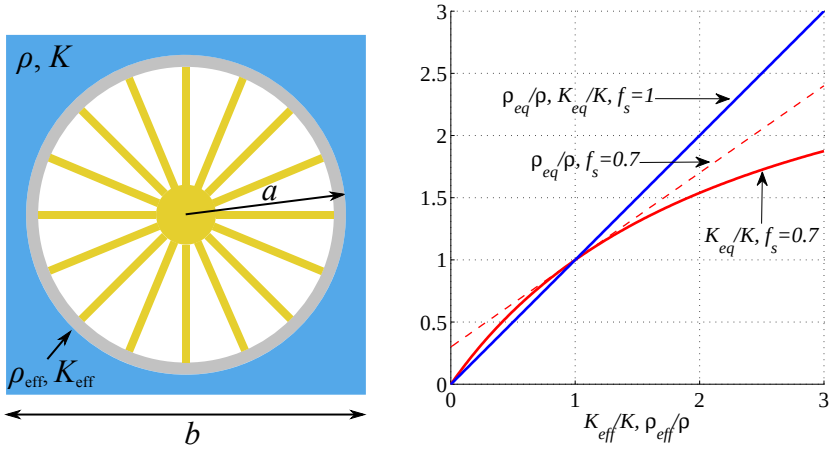

Figure 4.2: Left: A square unit cell of a fluid saturated array of shells. Right: Equivalent bulk modulus of the unit cell K_{eq} as a function of the effective bulk modulus of the tuned shell K_{eff} for several filling fractions.

unit cell depend on the surrounding fluid as

$$\frac{\rho_{eq}}{\rho} = 1 + f_s\Big(\frac{\rho_{eff}}{\rho} - 1\Big) \quad \Rightarrow \quad \frac{\rho_{eff}}{\rho} = 1 + \frac{1}{f_s}\Big(\frac{\rho_{eq}}{\rho} - 1\Big), \tag{4.5a}$$

$$\frac{K_{eq}}{K} = \frac{1}{1 + f_s(\frac{K}{K_{eff}} - 1)} \quad \Rightarrow \quad \frac{K_{eff}}{K} = \frac{1}{1 + \frac{1}{f_s}(\frac{K}{K_{eq}} - 1)}. \tag{4.5b}$$

The equivalent density and bulk modulus of the unit cell are significantly affected by the surrounding fluid. For shells of radius $a = 1$ cm with a relatively tight packing of $b = 2.2a$ yields a filling fraction of $f_s = 0.65$. In this case, in order to have the effective quasi-static bulk modulus of the unit cell $K_{eq} = 2K$, the effective bulk modulus of the shell-springs-mass system must be $K_{eff} = 4.33K$ (see Figure 4.2b).

The effective impedance of each shell relative to water (acoustic impedance $Z_{eff} = \sqrt{\rho K}$) is determined by

$$\frac{\rho_{eff}K_{eff}}{\rho K} = \frac{\rho_{eq}K_{eq}}{\rho K}\Big(\frac{1 - (1 - f_s)\rho/\rho_{eq}}{1 - (1 - f_s)K_{eq}/K}\Big). \tag{4.6}$$

The proposed array contains 7 by 7 unit cells of size $b = 2.2a$ with cylinders of radius $a = 1$ cm giving a filling fraction $f_s = 0.65$ and the side length of the lens $L = 15.4$ cm. Using this required equivalent stiffness of each unit cell K_{eq} in Figure 4.1a, the properties of the shell-springs-mass system are obtained from equation (4.5) as $\frac{K_{eff}}{K} = (1 + 1.54(\frac{K}{K_{eq}} - 1))^{-1}$. Consequently the effective properties of the shells must

be more extreme as shown in Figure 4.3a. The effective density of each shell-springs-mass system is tuned to water, see (4.2).

Each shell-spring-mass system is designed by the method outlined in § 2.3.2. The thickness of the aluminum shells has to vary form 0.03 to 0.12 to achieve this inhomogeneity of bulk modulus from $\frac{K_{eff}}{K} = 0.93$ to 3.21. Appropriate geometry of acrylic internal oscillator with $J = 16$ stiffeners tunes the shell to the required acoustic properties. The slow shells with $\frac{K_{eff}}{K}$ ranging from 0.62 to 0.86 are made of acrylic with $\frac{h}{a} = 0.3$ and tuned with an acrylic oscillator. The central shell is removed to give room for a monopole source.

The total pressure field was obtained by simulating the lens made of elastic shells in COMSOL. A symmetric quarter of the pressure field at monopole source frequencies of 10 kHz ($ka = 0.42, \lambda/a = 15$) and 15 kHz ($ka = 0.63, \lambda/a = 10$) is shown at same scales in Figures 4.3c and 4.3d, respectively. Also, Figure 4.3b shows the pressure ratio along the quarter circular arcs in Figures 4.3c and 4.3d between the field with the lens (shown) and source only (not shown).

At low frequencies the wavelength is much larger than the shell size $\lambda/a = 15$ and the lens is essentially transparent. However, at 15 kHz when $\lambda/a = 10$ each tuned shell behaves as an effective acoustic medium steering the wave from the corner to the faces. The wave travels across only 3 rows of shells and the maximum amplitude is magnified by a factor of 7 as seen in Figure 4.3b. The increase in the pressure amplitude from the faces and its decrease from the corner demonstrates wave steering.

A larger array of shells will increase the effectiveness of the lens. In the design of each shell, it is important to understand that this is a model with three parameters: shell thickness, oscillator stiffness and mass. The effectiveness of the internal oscillator changes with shell thickness. The following procedure will guarantee a successful design of this type of acoustic lens:

- Select the thickness of each shell to optimize the range of frequencies for it to behave as an effective medium.

- Design each oscillator so as to suppress all low frequency flexural waves of the

shell and maximize its natural frequency.

4.1.3 Realization with empty shells

In practice, it is difficult to produce the acrylic internal oscillators necessary to tune the shell as described in the previous section. As an alternative, it is possible to use quasi-statically tuned empty shells. This complicates the acoustic response as flexural resonances could be introduced. The three primary design criteria are that: 1) the shells are readily available, 2) the effective density of each shell matches water and 3) the effect is apparent near 20 kHz, which is the designated frequency of interest. The shells must be sub-wavelength, so the common outer diameter of 0.5 inches is selected. Fixing this outer dimension leaves two parameters: the shell thickness h/a, and the material of the shell. Table 4.1 summarizes several common shells which have nearly the same density as water, but varying effective bulk moduli.

Material	OD (in)	h (in)	h/a	ρ_{eff}	K_{eff}	c_{eff}	Z_{eff}	denoted
PVC	0.54	0.088	0.33	0.71	0.36	0.71	0.51	1
ABS	0.5	0.125	0.5	0.98	0.52	0.73	0.71	2
Acrylic	0.5	0.125	0.5	0.89	0.68	0.88	0.78	3
Polycarbonate	0.5	0.125	0.5	0.90	0.77	0.93	0.83	4
Brass	0.5	0.14	0.056	0.93	1.63	1.32	1.23	5
Brass	0.5	0.02	0.08	1.31	2.38	1.35	1.77	6
Copper	0.625	0.028	0.09	1.50	2.74	1.35	2.03	7
Aluminum	0.5	0.035	0.14	0.71	2.78	1.98	1.41	8
Aluminum	0.5	0.049	0.20	0.97	4.13	2.07	2.00	9
Aluminum	0.5	0.065	0.26	1.24	5.88	2.18	2.69	10

Table 4.1: Readily available shells (i.e. tubes and pipes) that have the effective density of water but different effective bulk moduli. All properties are normalized to water.

Clearly, it is extremely difficult to find shells that have the effective density of water while at the same time provide the necessary effective bulk modulus per Figure 4.1a. Instead, a near perfectly mapped lens is created, see Figure 4.4. The shell spacing is selected to be b=2.2 cm, hence the side length of the lens is 15.4 cm.

The simulation of the lens was carried out in COMSOL and is shown in Figure 4.4.

The frequency of the monopole source in the center of the lens is 22 kHz. For comparison, the lens with the unit cells replaced by the effective acoustic medium is shown and the pressure field due to the monopole source. The simulations indicate that the cylindrical-to-plane wave lens made from empty shells performs very well as compared the optimal case of each unit cell having the prescribed effective acoustic properties directly from the conformal mapping. It is also evident that the transmission is high. The downside to using empty shells is the possibility of exciting flexural resonances, which is not an issue with internally tuned shells. Since the shells are of different thickness and materials these flexural resonances are spread over many frequencies. If a shell resonates in a flexural mode, the effectiveness of the lens will drop or altogether disappear. The interaction of flexural waves on neighbouring shells will be analyzed closely in Chapter 5.

4.2 Active control of the effective properties

Aside form passive control of the effective acoustic properties via tuned shells, active control is also theoretically possible. To achieve this, the density and/or bulk modulus have to be changed dynamically. Although possible, it would be rather difficult to add or remove mass from a cylinder. Instead the stiffness could be changed. There are many springs which can dynamically change the stiffness, particularly from the robotics industry. One such example is a variable stiffness robot leg [25] which is essentially a curved beam with variable length. A schematic of the device applied to tuning an elastic shell is shown in Figure 4.6

This proposed mechanism consists of $J = 4$ variable stiffeners attached to a central rod. The rod serves as the added mass. The stiffness of the four open shells is controlled by their effective length. As the central rod is rotated relative to the shell, the length of the stiffener changes thereby changing the stiffness. The process of changing the stiffness can be almost instant. As a result, the cylinder can take on a range of effective acoustic properties. One application would be to detect and actively steer and incident wave.

Since this variable stiffness cylinder would be difficult to manufacture, a more appropriate first experiment would involve a binary type control. The shell could be either turned on, in which case the internal substructure makes it acoustically transparent, or turned off, in which case there would be much scattering. To promote the feasibility of such devices Figure 4.7 presents a circular array which is two shells in thickness in the radial direction. The array is insonified with a point source which is on top and out of the plotting window. Pink circles represent the tuned shells (turned on) and the white circles represent the empty shells (turned off). The absolute pressure field at $ka = 0.2$ is shown for three cases: (a) all shell are on and are acoustically transparent, (b) one radial row of shells is turned off and (c) three radial rows of shells are switched off. These simulations were done with a multiple scattering code developed in the acoustics group at Rutgers University which uses the T-matrix (3.21) for the tuned shells. The aluminum shells are those from § 3.5. The pressure distribution in plot (a) shows very little scattering proving that the shells are almost completely transparent by design. In plot (b) and more so in plot (c) the double ring of shells behaves as a Helmholtz resonator. The column of water in the throat oscillates projecting a beam in a direction normal to the incident wave.

One could also envision tuned shells as a mechanism for harvesting and converting incident acoustic energy. If the lengthwise ribs of the internal substructure are replaced by an appropriate piezoelectric material, a deformation will produce charge. This electrical energy can be gathered from many such shells and stored for later use. Such an idea is particularly suitable for underwater applications since all of the electronics could be stored safely inside of the shell.

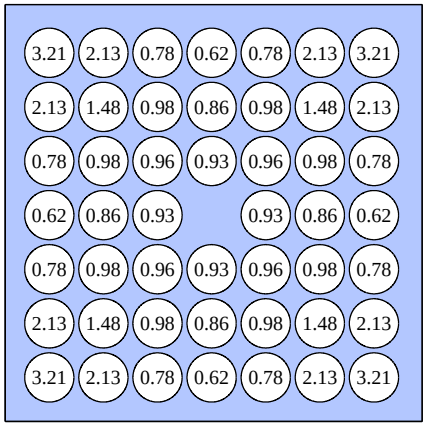

(a)

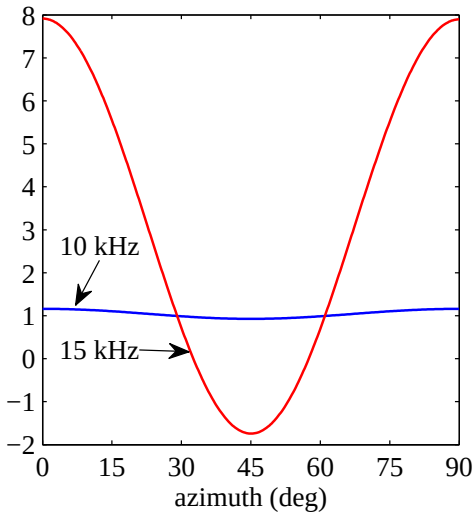

(b)

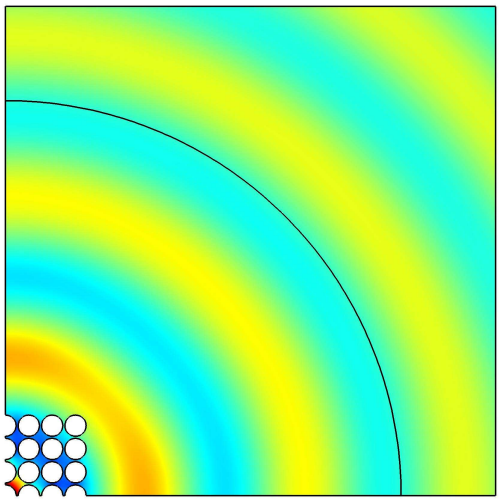

(c)

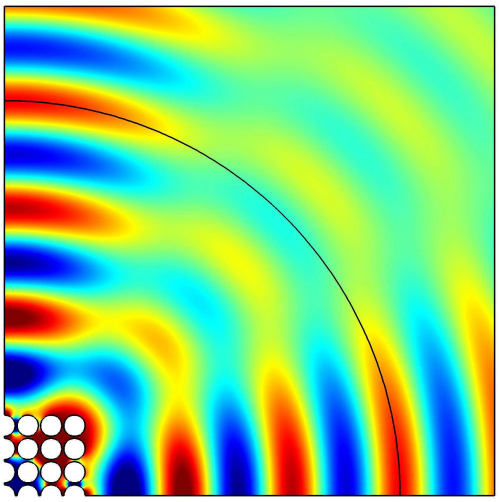

(d)

Figure 4.3: Cylindrical-to-plane wave lens. Plot (a) shows the bulk modulus distribution in the 7x7 array of tuned shell. Plots (c) and (d) show the pressure field around the lens at 10 kHz and 15 kHz, respectively. Plot (b) is the pressure normalized by the monopole source pressure without the lens along the quarter circular arcs in (c) and (d).

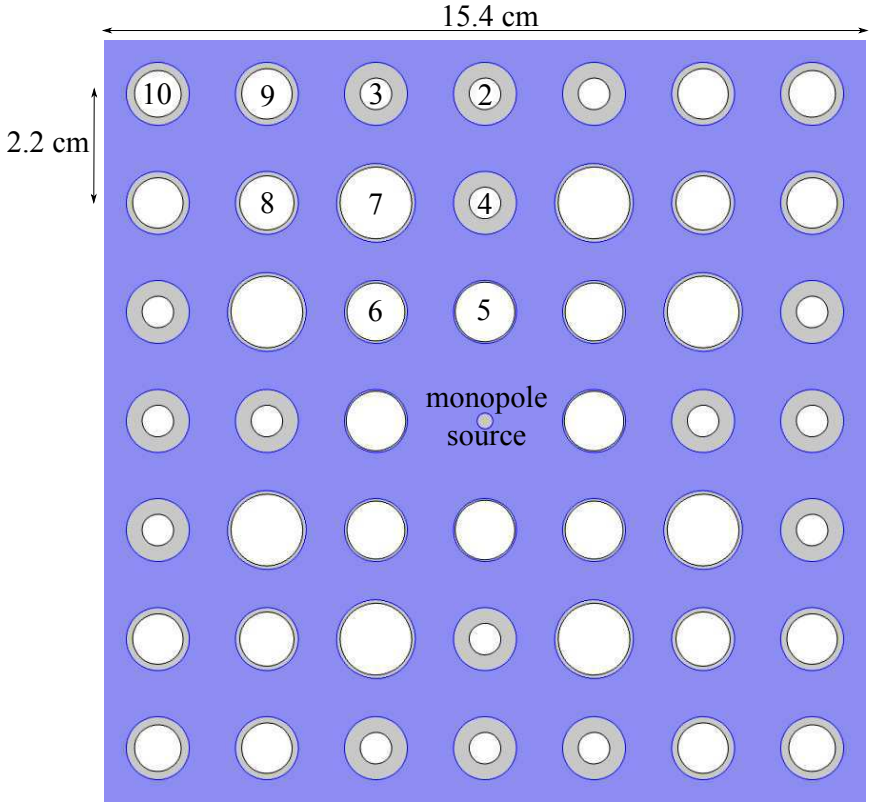

Figure 4.4: A cylindrical-to-plane wave lens constructed from a 7x7 array of various empty shells. The numbers correspond to the index of each shell shown in Table 4.1. Note the varying thicknesses.

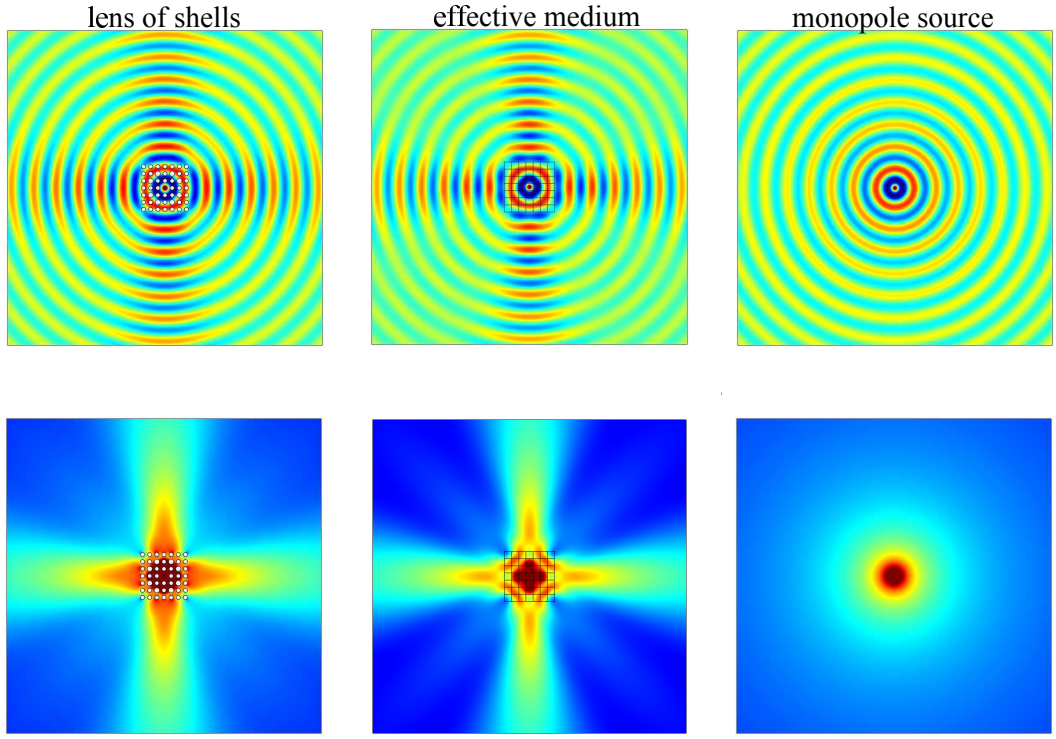

Figure 4.5: Left, middle and right columns are the simulated pressure fields for the lens of Figure 4.4, the effective acoustic medium in Figure 4.1 (the optimal case) and the source without the lens, respectively. Top row shows the total pressure field and the bottom row shows the absolute pressure field at 22 kHz.

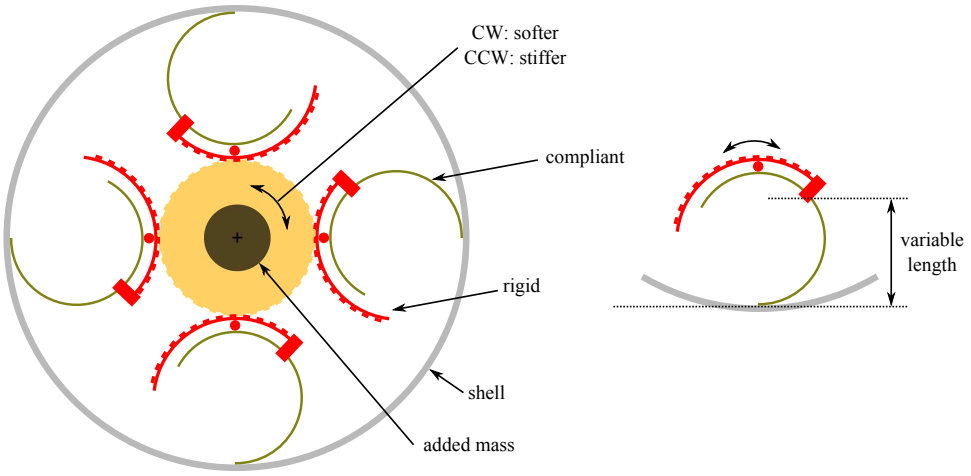

Figure 4.6: Mechanical tuning of an elastic shell by a variable stiffness mechanism leading to active control of the effective properties.

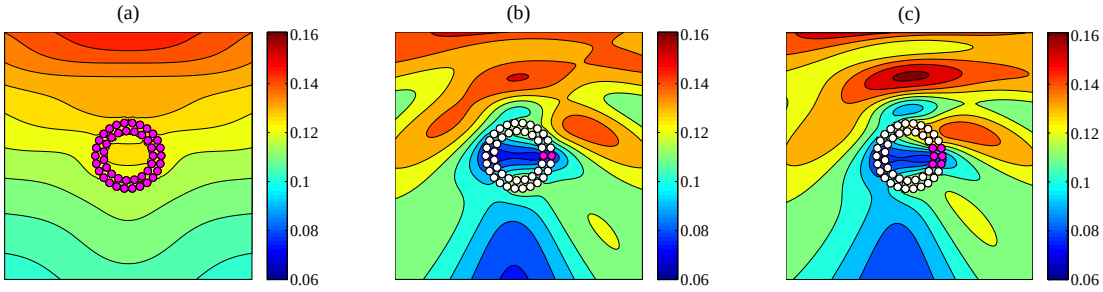

Figure 4.7: Absolute pressure field around a double ring of shells which can either be transparent (pink) or scattering (white). The point source which is on top and outside of the plot window at a frequency of $ka = 0.2$. The split ring in plots (b) and (c) the resembles a Helmholtz resonator.

Chapter 5

Interference of flexural-borne waves on closely spaced thin shells

Flexural waves are not present in sonic crystals of internally tuned elastic shells. This is because the proposed internal substructure couples the displacement of the shell at many points thereby stiffening the flexural modes (see § 3.5). As a result, the resonance frequency of these modes increases leaving a large low-frequency region where the system behaves as an acoustic medium. At higher frequencies, flexural waves diminish the performance by inhibiting wave steering and transmission.

For empty thin shells the flexural modal density is high (see equation (3.8)). Thus it is difficult to design broadband acoustic metamaterials with such elements. Although gratings of elastic shells in a fluid have seen application in acoustic metamaterials [48, 49, 63], the interaction of scattered fields from flexural waves on neighbouring shells is not well understood. Being subsonic, these waves do not couple to the incident field, but behave as a local resonance in the SC. These locally resonant inclusions in a wave medium produce narrow bands in the frequency spectrum, which can interfere with the propagating mode resulting in asymmetric pseudogaps in the frequency response. When the flexural resonance is out of phase with the surrounding medium, the array takes on negative effective properties (a resonant effect). On the contrary, full transmission has been observed within the Bragg band gap if the flexural resonance lies thereat, a region in which incident plane waves typically cannot propagate. Here we investigate the local interaction of neighbouring resonators, elastic cylindrical shells, and the resulting effect on the far-field response.

Liu et al. [61] point out that if an inclusion in an elastic matrix has a resonance frequency ω_0, the transmission coefficient is proportional to $1/(\omega_0^2 - \omega^2)$ yielding an

asymmetric profile. They present experimental and theoretical work on an 8x8x8 cubic array of rubber coated lead spheres in a hard epoxy matrix. The asymmetric shape of the transmission coefficient near the resonance is discussed and correlated with the band diagram where the dip in the transmission corresponds to the lower edge of the pseudogap and the peak, the upper edge. A very important point made is that the sonic attenuation is a consequence of the local resonant behaviour and would be apparent even for a monolayer, as opposed to Bragg scattering which requires many periodic layers to abate an incident wave.

The study was extended to square arrays of circular cylinders by Goffaux et al. [29]. It was noted that the asymmetric profile of the transmission spectrum near the resonance frequency of the cylinder resembled the Fano [21] resonance due to the interference of a discrete autoionized state with a continuum. Goffaux et al. proposed a 1D spring-mass model to describe the interference between the elastic cylinder and surrounding matrix. Later, Goffaux and Sanchez-Dehesa [28] formulated a variational method for efficient calculation of the band structure of such phononic crystals. Furthermore, they improved the 1D model used to describe the interference with the resonant inclusion and validated it by comparing the predicted width of the pseudogap as a function of the lattice constant to simulated results.

The effect of flexural waves on elastic shells in a sonic crystal was first investigated by Khelif et al. [45], although the distinction that these are flexural waves was not made. They studied steel shells in water with thickness to radius ratio between $h/a = 0.4-0.45$ and a lattice parameter to radius ratio of $b/a = 2.5$. By tuning the shell's flexural resonance to lie in the Bragg band gap, they were able to achieve full transmission at a single frequency and no transmission elsewhere in the band gap. This was shown to be a suitable approach for filtering a single frequency from an input signal. The work was further expanded by Pennec et al. [76] by introducing shells of alternating thickness in a row along the direction of propagation. This lead to the transmission of two distinct frequencies in the effective guide. This system can also be used for separating or merging signals of different frequencies.

Kosevich et al. [48] studied transmission through a periodic array of thin elastic

cylindrical shells in air (artificial shells with $\rho_s = 50\rho_{air} = 50\text{kg/m}^3$, $C_{ts} = 2000\text{m/s}$, $C_{ls} = 4000\text{m/s}$). Analogous to previous structures, the flexural resonances are responsible for the asymmetric profile of the transmission spectrum. It was shown that an enhancement of the width of the Bragg band gap occurs when the lowest flexural resonance of the shell ($n = 2$) lies in the band gap associated with Bragg scattering.

Before the interest in acoustic metamaterials, Heckl and Mulholland [38] studied wave propagation through a grating of elastic shells in the context of heat exchangers. Lethuillier et al. [56] analyzed the resonant interaction of the Scholte-Stoneley waves on neighboring shells. More recently, low frequency breathing modes of soft rubber shells in air also have been shown to produce pseudogaps below the Bragg frequency [49], but flexural vibrations are quite different due to their azimuthal directionality. It has also been shown that the A-wave interaction on neighbouring shells results in a significant increase in the far-field scattered pressure at resonance [96].

This Chapter investigates the interaction of the flexural-borne waves from neighbouring shells in water and whether any enhancement of the far-field scattering is possible. The aim is to accurately predict the resonance frequency, bandwidth and decay rate of a flexural resonance. This will be achieved through asymptotic analysis of a higher order shell theory with multiple scattering theory.

5.1 Evanescence

Consider a wave incident onto a cylindrical shell with wavenumber $k = \omega/c$. Some incident energy will be transferred to the flexural vibrations of the shell and the rest will scatter back into the fluid. Define the normal and tangential wavenumbers as k_n and k_t, respectively. The wavelength of the n^{th} flexural wave is $\lambda = 2\pi a/n$, thus the tangential wavenumber can be expressed as $k_t = n/a$. From the Helmholtz equation, the wavenumber of the scattered wave is $k_n^2 = k^2 - k_t^2 = \frac{\omega^2}{c^2} - \frac{n^2}{a^2}$. Thus at flexural resonance

$$(k_n a)^2 = \frac{c_p^2}{c^2}\Omega_r^2 - n^2, \tag{5.1}$$

which implies that the scattered wave is evanescent while $\frac{c_p}{c}\Omega_r < n$. In § 5.2.2, the expression for the low order resonance frequency of flexural modes on thin shells is derived, which is $\Omega_r^2 = \beta^2(n^2-1)^2/(1+\rho/(\sqrt{12}\beta n\rho_s))$. Figure 5.1 shows the normal component of the wavenumber scattered from a flexural resonance for an aluminum shell with thickness ratio $h/a = 0.03$.

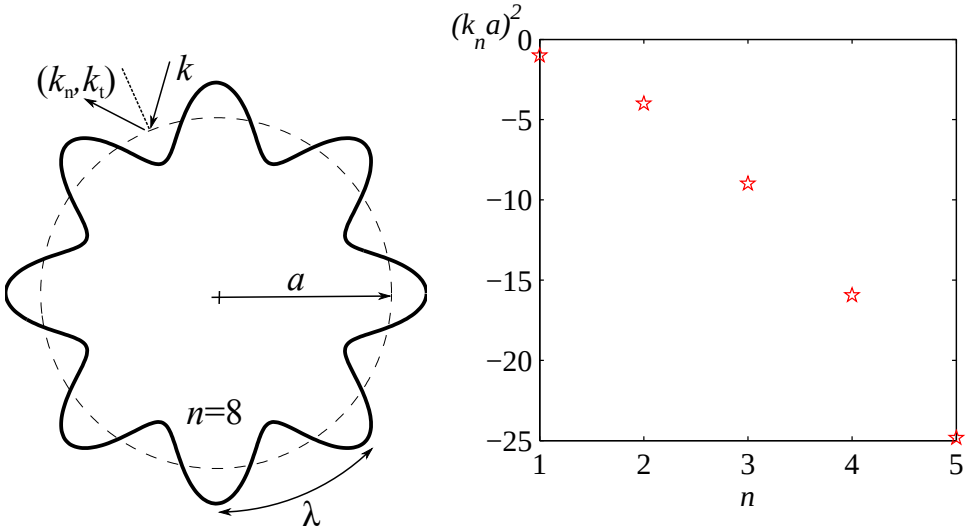

Figure 5.1: Left: Scattering from the n=8 flexural mode of a thin shell. Right: Normal component of the scattered wavenumber squared $(k_n a)^2$ for several low order flexural modes of an aluminum shell of thickness ratio $h/a = 0.03$.

This simple analysis demonstrates that low order flexural waves of thin shells are evanescent, decaying with radial distance. As an example, the amplitude of the wave scattered form the $n = 2$ flexural wave on the aluminum shell in Figure 5.1 decays by 63% (e^{-1}) in a distance $r/a = 0.5$. Therefore, scattered flexural waves from thin shells do not propagate into the far-field (see the dashed line in Figure 3.12b for the empty shell of thickness $h/a = 0.03$). Of all of the low order flexural waves, the $n = 2$ flexural resonance is the least evanescent.

5.2 Higher order shell theories

For most engineering applications, the Donnel-Mushtari (D-M) thin shell theory is sufficient. However, it will be demonstrated that in order to accurately predict the

lowest flexural resonances, a higher order shell theory is required, such as the Love-Timoshenko (L-T) or Flügge-Byrne-Lur'ye (F-B-L) theories.

5.2.1 Free vibration

Loosely adopting the notation from Leissa's text [54], the shell's equations of motion can be written as $[\mathcal{L}]\{u_i\} = \{\bar{\sigma}_i\}$ where the matrix $[\mathcal{L}]$ operates on the displacement vector $\boldsymbol{u} = \{w, v, u\}$ in the (r, θ, z) cylindrical coordinates. The dimensionless traction vector is $\bar{\sigma} = \{\frac{a^2}{\rho_s c_p^2 h}\sigma(\theta, t), 0, 0\}$, where we only include the radial component of the stress $\sigma(\theta, t)$. For in-plane vibrations the operator takes the form

$$[\mathcal{L}] = \underbrace{\begin{bmatrix} 1+\beta^2\frac{\partial^4}{\partial\theta^4}+\frac{a^2}{c_p^2}\frac{\partial^2}{\partial t^2} & \frac{\partial}{\partial\theta} \\ \frac{\partial}{\partial\theta} & \frac{\partial^2}{\partial\theta^2}-\frac{a^2}{c_p^2}\frac{\partial^2}{\partial t^2} \end{bmatrix}}_{D-M} + \beta^2 \left(\underbrace{\begin{bmatrix} 0 & -\frac{\partial^3}{\partial\theta^3} \\ -\frac{\partial^3}{\partial\theta^3} & \frac{\partial^2}{\partial\theta^2} \end{bmatrix}}_{L-T} \text{ OR } \underbrace{\begin{bmatrix} 1-2\frac{\partial^2}{\partial\theta^2} & 0 \\ 0 & 0 \end{bmatrix}}_{F-B-L} \right) \tag{5.2}$$

where $\beta = h/(\sqrt{12}a)$ is a small bending parameter. Note the second term, which is the improvement over the Donnel-Mushtari equations. The differences in shell theories arise form different definitions of the change in curvature and twist of the middle surface. Expanding the in-plane displacements and stresses in azimuthal modes $(w, v, \sigma) = \sum_{n=-\infty}^{\infty}(W_n, V_n, \sigma_n)\mathrm{e}^{in\theta}\mathrm{e}^{-i\omega t}$ and substituting into the equations of motions yields

$$\begin{bmatrix} d_1 & d_2 \\ d_3 & d_4 \end{bmatrix} \begin{bmatrix} W_n \\ V_n \end{bmatrix} = \begin{bmatrix} \frac{a^2}{\rho_s c_p^2 h}\sigma_n \\ 0 \end{bmatrix}, \tag{5.3}$$

where the elements d_{1-4} depend on the shell theory used

$$\begin{bmatrix} d_1 & d_2 \\ d_3 & d_4 \end{bmatrix} = \underbrace{\begin{bmatrix} (-\Omega^2+1+\beta^2 n^4) & in \\ in & (\Omega^2-n^2) \end{bmatrix}}_{D-M} + \beta^2 \left(\underbrace{\begin{bmatrix} 0 & in^3 \\ in^3 & -n^2 \end{bmatrix}}_{L-T} \text{ OR } \underbrace{\begin{bmatrix} 1-2n^2 & 0 \\ 0 & 0 \end{bmatrix}}_{F-B-L} \right). \tag{5.4}$$

Define the shell impedance Z_n^{sh}, which relates the applied pressure to the resulting velocity, as

$$\sigma_n = -i\omega Z_n^{sh} W_n, \quad Z_n^{sh} = -i\rho_s c_p \frac{h}{a}\left(\frac{-d_1 d_4 + d_2 d_3}{\Omega d_1}\right). \tag{5.5}$$

The determinant of the coefficient matrix (5.4), explicitly visible in the shell impedance (5.5), governs the natural frequencies $\Omega_{r,c} = \omega_{r,c}a/c_p$ for radial (flexural or in-plane bending) and circumferential modes of vibration, respectively, which are for $n \neq 0$ [24, 54] The ex-

Theory	$\Omega^2_{r,c}$	$\lim_{\beta\to 0} \Omega_r$	
		w/IPI	w/o IPI
D-M	$\frac{1}{2}\{(1+n^2+\beta^2n^4) \mp\sqrt{(1+n^2+\beta^2n^4)^2-4\beta^2n^6}\}$	$\frac{\beta n^3}{\sqrt{1+n^2}}$	βn^2
L-T	$\frac{1}{2}\{(1+n^2)(1+\beta^2n^2) \mp\sqrt{(1+n^2)^2(1+\beta^2n^2)^2-4\beta^2n^2(n^2-1)^2}\}$	$\frac{\beta n(n^2-1)}{\sqrt{1+n^2}}$	$\beta(n^2-1)$
F-B-L	$\frac{1}{2}\{(1+n^2+\beta^2(n^2-1)^2) \mp\sqrt{(1+n^2+\beta^2(n^2-1)^2)^2-4\beta^2n^2(n^2-1)^2}\}$	$\frac{\beta n(n^2-1)}{\sqrt{1+n^2}}$	$\beta(n^2-1)$
membrane	$(0, 1+n^2)$	-	-

Table 5.1: Comparison of the resonance frequencies of a shell's radial and circumferential modes using several shell theories. Asymptotic forms are shown with and without the inclusion of in-plane inertia (IPI) in the equations of motion.

pressions for $\Omega^2_{r,c}$ in Table 5.1 are complete and differ slightly from Table 2.1 of Leissa's text [54] where terms of order β^2 were omitted. The natural frequencies for $n = 0$ are $\Omega^2_{r,c} = (1, 0)$ from both the D-M and L-T theories and $\Omega^2_{r,c} = (1+\beta^2, 0)$ from the F-B-L theory. The asymptotic radial frequencies as $\beta \to 0$ are presented with and without the in-plane inertia (IPI) term $\frac{a^2}{c_p^2}\frac{\partial^2 v}{\partial t^2}$ in equation (5.2), which is often omitted to simplify the expression. At this stage it is clear that both the L-T and F-B-L theories yield the same natural frequencies for thin shells. The D-M shell theory predicts a higher flexural resonance frequency for a given mode n and as Forsberg [24] points out, the maximum error is for the $n = 2$ flexural mode.

5.2.2 Fluid loaded shell

Of interest is the in-plane acoustic wave scattering from a thin cylindrical shell immersed in an acoustic medium of density ρ and sound speed c. The external pressure field satisfies the Helmholtz equation (3.1) leading to expressions for the scattering coefficients (3.10) and modal pressure (3.11). The radial stress on the shell is balanced by the acoustic pressure $\sigma_n = -P_n$ as in (3.13). Substituting equations (3.13) into (5.2)

yields the equation of motion as

$$\begin{bmatrix} \left(d_1 + \frac{\rho c}{\rho_s c_p}\frac{\Omega}{h/a}\frac{H_n^{(1)}(ka)}{H_n^{(1)\prime}(ka)}\right) & d_2 \\ d_3 & d_4 \end{bmatrix} \begin{bmatrix} W_n \\ V_n \end{bmatrix} = \begin{bmatrix} -i\frac{2a}{\pi\rho_s c_p^2 h/a}\frac{A_n}{kaH_n^{(1)\prime}(ka)} \\ 0 \end{bmatrix}, \tag{5.6}$$

The scattering coefficients are obtained by solving (5.6) for radial modal displacement W_n (3.14) and leading to the T-matrix definition (3.15). The difference now is that the shell impedance in the term ζ_n (3.14) will differ depending on the shell theory.

In order to obtain insight about the structure of the T-matrix, we first apply the small argument approximation as in Ref. [2] to the Halkel functions seen in the acoustic impedance Z_n (3.12)

$$\frac{H_n^{(1)}(ka)}{H_n^{(1)\prime}(ka)} \approx -\frac{ka}{n} - i\frac{4\pi(ka/2)^{2n+1}}{(n!)^2}, \quad ka \ll n, \quad n \neq 0. \tag{5.7}$$

This assumption is valid near the n^{th} flexural resonance since $\Omega_r = \beta n^2 \ll n$ for thin shells. Substituting equation (5.7) into equation (3.12) yields the asymptotic form of the acoustic impedance

$$Z_n = -i\rho_s c_p \frac{h}{a}\left[\frac{\alpha}{n}\Omega + i\alpha\gamma_n\Omega^{(2n+1)}\right], \tag{5.8}$$

where $\gamma_n \equiv \frac{2\pi}{(n!)^2}\left(\frac{c_p}{2c}\right)^{2n}$ and the parameter α relates the mass of the shell to that of the displaced fluid as

$$\alpha \equiv \frac{\rho}{\rho_s h/a}. \tag{5.9}$$

The total impedance takes the form

$$\begin{aligned} Z_n^{sh} + Z_n &= -i\rho_s c_p \frac{h}{a}\left[\frac{((\alpha/n)\Omega^2 - d_1)d_4 + d_2 d_3}{\Omega d_1} + i\alpha\gamma_n\Omega^{(2n+1)}\right] \\ &= -i\rho_s c_p \frac{h}{a}\left[\frac{(1+\alpha/n)F(\Omega)}{\Omega d_1} + i\alpha\gamma_n\Omega^{(2n+1)}\right], \end{aligned} \tag{5.10}$$

where the real and imaginary portions have been grouped. The coefficients d_{1-4} depend on the shell theory used and are given in (5.4). The characteristic equation $F(\Omega)$ for

each shell theory is given by

$$F(\Omega) = (\Omega^2)^2 - \begin{cases} ((1+\beta^2 n^4)(1+\alpha/n)^{-1} + n^2)\Omega^2 + \beta^2 n^6 (1+\alpha/n)^{-1}, & \text{D-M,} \\ ((1+\beta^2 n^4)(1+\alpha/n)^{-1} + (1+\beta^2)n^2)\Omega^2 + \beta^2 n^2 (n^2-1)^2 (1+\alpha/n)^{-1}, & \text{L-T,} \\ ((1+\beta^2 (n^2-1)^2)(1+\alpha/n)^{-1} + n^2)\Omega^2 + \beta^2 n^2 (n^2-1)^2 (1+\alpha/n)^{-1}, & \text{F-B-L.} \end{cases} \tag{5.11}$$

If $\alpha = 0$, the two roots of equations (5.11) yield the natural frequencies of free vibration in Table 5.1. Otherwise, the two roots correspond to the damped resonance frequencies of the radial and circumferential modes of vibration Ω_1 and Ω_2, respectively (previously denoted by Ω_r and Ω_c for the free vibration case). The fluid loading on the shell lowers the flexural resonance frequencies only, not the circumferential resonances. The asymptotic flexural frequencies are $\Omega_1^2 = \Omega_r^2(1+\alpha/n)^{-1}$. The factor α, defined in equation (5.9), governs the radiation damping through the ratio of shell's mass to the mass of the displaced water.

Figure 5.2 plots the first five flexural resonance frequencies for a thin aluminum shell ($\rho_s = 2730$ kg/m^3, $E_s = 69e9$ GPa, $\nu_s = 0.33$, $c_p = 5326$ m/s) of thickness $h/a = 0.01$ and 0.05 yielding $\alpha = 36.6$ and 7.3, respectively. The theoretical frequencies are compared to finite element (FEM) eigenfrequency simulations. All of the theories are based on the thin shell assumption, thus the results for the thicker shell with $h/a = 0.05$ are not as well predicted. However, for the very thin shell with $h/a = 0.01$, the flexural resonance frequency is almost exactly predicted by the asymptotic form without in-plane inertia from L-T or F-B-L theories. Therefore, from here on the following approximate radial and circumferential resonance frequencies will be used

$$\Omega_1 = \frac{\beta(n^2-1)}{\sqrt{1+\alpha/n}}, \qquad \Omega_2 = n. \tag{5.12}$$

Note that for the lowest order modes, the radial resonance frequency is nonlinear $\Omega_1^2 = O(\beta^{3/2}, n^{5/2}, \alpha^{1/2})$.

Since the two frequencies Ω_1 and Ω_2 are roots of $F(\Omega) = (\Omega^2 - \Omega_1^2)(\Omega^2 - \Omega_2^2)$ the

total impedance can be rewritten in a more compact form

$$Z_n^{sh} + Z_n = -i\rho_s c_p \frac{h}{a}\left[\frac{(1+\alpha/n)(\Omega^2-\Omega_1^2)(\Omega^2-\Omega_2^2)}{\Omega d_1} + i\alpha\gamma_n\Omega^{(2n+1)}\right]. \tag{5.13}$$

The definition of d_1 in equation (5.4) for the L-T theory is $d_1 = \Omega^2 - n^2(1+\beta^2)$, which for thin shells is approximately $d_1 = \Omega^2 - n^2$. Substituting this d_1 into (5.13) yields

$$Z_n^{sh} + Z_n = -i\rho_s c_p \frac{h}{a}\left[\frac{(1+\alpha/n)(\Omega^2-\Omega_1^2)(\Omega^2-\Omega_2^2)}{\Omega(\Omega^2-n^2)} + i\alpha\gamma_n\Omega^{(2n+1)}\right]. \tag{5.14}$$

5.3 Width of flexural resonances

Near a flexural resonance Ω_1, the total impedance behaves linearly as

$$Z_n^{sh} + Z_n = -i\rho_s c_p \frac{h}{a}\left[c_n(\Omega-\Omega_1) + i\alpha\gamma_n\Omega_1^{(2n+1)}\right], \tag{5.15}$$

where $c_n = 2(1+\alpha/n)(\Omega_1^2-\Omega_2^2)(\Omega_1^2-n^2)^{-1}$. Using (5.15) and the definition of ζ_n in (3.14), the T-matrix (3.15) becomes

$$T_n = -\frac{1}{2}\left[\left(\frac{\Omega_1-\Omega+i\epsilon_n}{\Omega_1-\Omega-i\epsilon_n}\right)\frac{H_n^{(2)\prime}(ka)}{H_n^{(1)\prime}(ka)} + 1\right], \tag{5.16}$$

where

$$\epsilon_n \equiv \alpha\gamma_n\Omega_1^{(2n+1)}/c_n = \frac{\pi\alpha}{(1+\alpha/n)(n!)^2}\frac{(\Omega_1^2-n^2)}{(\Omega_1^2-\Omega_2^2)}\left(\frac{c_p}{2c}\right)^{2n}\Omega_1^{(2n+1)}. \tag{5.17}$$

Using the asymptotic frequencies in equation (5.12), the nondimensional half-width of the flexural resonance becomes

$$\epsilon_n = \frac{\pi\alpha(n^2-1)^{(2n+1)}}{(1+\alpha/n)^{(n+3/2)}(n!)^2}\left(\frac{c_p}{2c}\right)^{2n}\beta^{(2n+1)}. \tag{5.18}$$

The asymmetric profile of the T-matrix is now clearly visible. The width of the flexural resonance is $2\epsilon_n$ and remains small because $\epsilon_n \propto (h/a)^{(3n+3/2)}$ while $\alpha > n$. For example, for the $n = 2$ flexural mode $\epsilon_n \propto (h/a)^{7.5}$. The quality factor for the n^{th} flexural resonance of a thin shell is thus very large

$$Q \equiv \frac{\Omega_1}{\epsilon_n} = \frac{(n!)^2}{\pi(n^2-1)^{2n}}\left(\frac{2c}{c_p}\right)^{2n}\frac{(1+\alpha/n)^{(n+1)}}{\alpha\beta^{2n}}. \tag{5.19}$$

Although the asymmetric response is narrowband, it has an interesting structure with four distinct modes of coupling to the incident wave: at the maximum, at the resonance, at the minimum and far from the resonance and are summarized in Table 5.3.

	Ω	T_n	analogue
Far from Ω_1	$\lvert\Omega/\Omega_1\rvert \gg 1$	$-\frac{J_n'}{H_n^{(1)\prime}}$	sound hard
Maximum	$\Omega_1 - \epsilon_n$	$-\frac{iJ_n'}{H_n^{(1)\prime}} - \frac{1-i}{2}$	$\mathrm{e}^{i\pi/2}$ out of phase
At resonance	Ω_1	$\frac{J_n'}{H_n^{(1)\prime}} - 1$	$\mathrm{e}^{i\pi}$ out of phase
Minimum	$\Omega_1 + \epsilon_n$	$\frac{iJ_n'}{H_n^{(1)\prime}} - \frac{1+i}{2}$	$\mathrm{e}^{-i\pi/2}$ out of phase

A special case occurs when the effective density of the thin empty shell is tuned to water such that $2\rho_s h/a = \rho$ giving $\alpha = 2$ and the extensional wave speed is $c_p = 2c$. The half-width of the flexural resonance becomes $\epsilon_n = 2\pi\left(\frac{(n^2-1)^{(2n+1)}}{(1+2/n)^{(n+3/2)}(n!)^2}\right)\beta^{(2n+1)}$, which will never be zero for $n \geq 2$.

Figure 5.3 compares the exact T-matrix for the $n = 2$ flexural mode from equation (3.15) with the linearized T-matrix in equation (5.16). Although there is a very small frequency shift, this figure demonstrates that the approximation (5.7) is accurate at frequencies near the lower flexural resonances of a thin shell. Thus, the following conclusions can be made about the present analysis: i) equation (5.12) accurately predicts the flexural resonance frequencies of a thin shell ii) equation (5.17) accurately describes the width of the flexural resonance.

5.4 Multiple scattering of several shells

Multiple scattering of acoustic waves from two or more elastic shells at a flexural resonance is now investigated. The cylinders are laying on a line separated by a distance b. In order to relate the scattered field from one scatterer to the other, Graf's addition theorem is necessary. It states that the Hankel function at the j^{th} cylinder can be transformed to the coordinates of the i^{th} cylinder as

$$H_n^{(1)}(kr_j)\mathrm{e}^{in\theta_j} = \sum_{m=-\infty}^{\infty} J_m(kr_i)\mathrm{e}^{im\theta_i} \times \begin{cases} H_{m-n}^{(1)}(kb), & r_j < r_i, \\ H_{n-m}^{(1)}(kb), & r_j > r_i. \end{cases} \tag{5.20}$$

5.4.1 Two scatterers

Consider two shells: one at the origin and the other at a distance b on the positive x-axis. The shells are described by the respective polar coordinates (r_1, θ_1) and (r_2, θ_2), respectively. An incident wave $p_i^{(j)} = \sum_{n=-\infty}^{\infty} A_n^{(j)} J_n(kr_j)\mathrm{e}^{in\theta_j}$ will scatter from the pair giving rise to two scattered waves $p_s^{(1)} = \sum_{n=-\infty}^{\infty} B_n^{(1)} H_n^{(1)}(kr_1)\mathrm{e}^{in\theta_1}$ and $p_s^{(2)} = \sum_{n=-\infty}^{\infty} B_n^{(2)} H_n^{(1)}(kr_2)\mathrm{e}^{in\theta_2}$. The resulting total pressure field $p = p_i + p_s^{(1)} + p_s^{(2)}$ can be expressed in terms of the coordinates of the individual shell as [64]

$$p^{(1)} = \sum_{n=-\infty}^{\infty} \left(A_n^{(1)} J_n(kr_1)\mathrm{e}^{in\theta_1} + B_n^{(1)} H_n^{(1)}(kr_1)\mathrm{e}^{in\theta_1} + B_n^{(2)} H_n^{(1)}(kr_2)\mathrm{e}^{in\theta_2}\right), \quad (5.21a)$$

$$p^{(2)} = \sum_{n=-\infty}^{\infty} \left(A_n^{(2)} J_n(kr_2)\mathrm{e}^{in\theta_2} + B_n^{(1)} H_n^{(1)}(kr_1)\mathrm{e}^{in\theta_1} + B_n^{(2)} H_n^{(1)}(kr_2)\mathrm{e}^{in\theta_2}\right), \quad (5.21b)$$

where the superscript on p indicates from where the pressure is observed. Using Graf's addition theorem, the radial coordinate of the second scattered wave is transformed to the radial coordinate of the first via

$$H_n^{(1)}(kr_2)\mathrm{e}^{in\theta_2} = \sum_{m=-\infty}^{\infty} H_{m-n}^{(1)}(kb) J_m(kr_1)\mathrm{e}^{im\theta_1}, \quad r_2 < r_1 \quad (5.22a)$$

$$H_n^{(1)}(kr_1)\mathrm{e}^{in\theta_1} = \sum_{m=-\infty}^{\infty} H_{n-m}^{(1)}(kb) J_m(kr_2)\mathrm{e}^{im\theta_2}, \quad r_1 > r_2. \quad (5.22b)$$

Substituting (5.22) into (5.21) yields the total pressure field

$$p^{(1)} = \sum_{n=-\infty}^{\infty} \mathrm{e}^{in\theta_1}\left(A_n^{(1)} J_n(kr_1) + B_n^{(1)} H_n^{(1)}(kr_1) + J_n(kr_1) \sum_{m=-\infty}^{\infty} B_m^{(2)} H_{n-m}^{(1)}(kb)\right), \quad (5.23a)$$

$$p^{(2)} = \sum_{n=-\infty}^{\infty} \mathrm{e}^{in\theta_2}\left(A_n^{(2)} J_n(kr_2) + B_n^{(2)} H_n^{(1)}(kr_2) + J_n(kr_2) \sum_{m=-\infty}^{\infty} B_m^{(1)} H_{m-n}^{(1)}(kb)\right), \quad (5.23b)$$

The total incident wave onto each shell is the sum of the incident wave and the scattered wave from the neighbouring shell, i.e. the total incident wave onto the first shell is $p_i^{(1)} = \sum_{n=-\infty}^{\infty} \left[A_n^{(1)} + \sum_{m=-\infty}^{\infty} B_m^{(2)} H_{m-n}^{(1)}(kb)\right] J_n(kr_1)\mathrm{e}^{in\theta_1}$. The scattered pressure field

from each shell is obtained by using the general definition of the T-matrix

$$p_s^{(1)} = \sum_{n=-\infty}^{\infty} T_n^{(1)}\big(A_n^{(1)} + \sum_{m=-\infty}^{\infty} B_m^{(2)} H_{n-m}^{(1)}(kb)\big) H_n^{(1)}(kr_1)\mathrm{e}^{in\theta_1}, \tag{5.24a}$$

$$p_s^{(2)} = \sum_{n=-\infty}^{\infty} T_n^{(2)}\big(A_n^{(2)} + \sum_{m=-\infty}^{\infty} B_m^{(1)} H_{m-n}^{(1)}(kb)\big) H_n^{(1)}(kr_2)\mathrm{e}^{in\theta_2}, \tag{5.24b}$$

where the T-matrix retains its definition in equation (3.15) and relates the incident and scattered coefficients as

$$B_n^{(1)} = T_n^{(1)}\big(A_n^{(1)} + \sum_{m=-\infty}^{\infty} B_m^{(2)} H_{n-m}^{(1)}(kb)\big), \tag{5.25a}$$

$$B_n^{(2)} = T_n^{(2)}\big(A_n^{(2)} + \sum_{m=-\infty}^{\infty} B_m^{(1)} H_{m-n}^{(1)}(kb)\big). \tag{5.25b}$$

Generally, after truncating the series, the linear system of equations (5.25) can be solved in matrix form for the scattered coefficients $B_n^{(1,2)}$ via

$$\left(\begin{bmatrix} \boldsymbol{I} & \mathbf{0} \\ \mathbf{0} & \boldsymbol{I} \end{bmatrix} - \begin{bmatrix} \mathrm{diag}(T_n^{(1)}) & \mathbf{0} \\ \mathbf{0} & \mathrm{diag}(T_n^{(2)}) \end{bmatrix} \begin{bmatrix} \mathbf{0} & [H_{n-m}^{(1)}(kb)] \\ [H_{m-n}^{(1)}(kb)] & \mathbf{0} \end{bmatrix}\right) \begin{bmatrix} [B_n^{(1)}] \\ [B_n^{(2)}] \end{bmatrix} = \begin{bmatrix} \mathrm{diag}(T_n^{(1)}) & \mathbf{0} \\ \mathbf{0} & \mathrm{diag}(T_n^{(2)}) \end{bmatrix} \begin{bmatrix} [A_n^{(1)}] \\ [A_n^{(2)}] \end{bmatrix}. \tag{5.26}$$

5.4.2 Frequency splitting

For a shell excited by a monochromatic incident wave at frequencies near the n^{th} flexural mode, the n^{th} coefficient will be by far the largest. Thus equation (5.25) can be approximated by

$$B_n^{(1)} = T_n^{(1)}\left[A_n^{(1)} + B_n^{(2)} H_0^{(1)}(kb) + B_{-n}^{(2)} H_{2n}^{(1)}(kb)\right], \tag{5.27a}$$

$$B_{-n}^{(1)} = T_{-n}^{(1)}\left[A_{-n}^{(1)} + B_n^{(2)} H_{-2n}^{(1)}(kb) + B_{-n}^{(2)} H_0^{(1)}(kb)\right], \tag{5.27b}$$

$$B_n^{(2)} = T_n^{(2)}\left[A_n^{(2)} + B_n^{(1)} H_0^{(1)}(kb) + B_{-n}^{(1)} H_{-2n}^{(1)}(kb)\right], \tag{5.27c}$$

$$B_{-n}^{(2)} = T_{-n}^{(2)}\left[A_{-n}^{(2)} + B_n^{(1)} H_{2n}^{(1)}(kb) + B_{-n}^{(1)} H_0^{(1)}(kb)\right]. \tag{5.27d}$$

Since the scatterers are identical, $T_{\pm n}^{(1)} = T_{\pm n}^{(2)} = T_{\pm n}$, and from equation (3.15) it is clear that $T_n = T_{-n}$. Also, the Hankel functions are related as $H_{-2n}^{(1)}(kb) = H_{2n}^{(1)}(kb)$.

Equations (5.27) can then be expressed in matrix form

$$\mathbf{Mb} = \mathbf{a} \quad \text{where}$$

$$\mathbf{M} = \begin{bmatrix} 1/T_n & 0 & H_0^{(1)}(kb) & H_{2n}^{(1)}(kb) \\ 0 & 1/T_n & H_{2n}^{(1)}(kb) & H_0^{(1)}(kb) \\ H_0^{(1)}(kb) & H_{2n}^{(1)}(kb) & 1/T_n & 0 \\ H_{2n}^{(1)}(kb) & H_0^{(1)}(kb) & 0 & 1/T_n \end{bmatrix}, \ \mathbf{b} = \begin{bmatrix} B_n^{(1)} \\ B_{-n}^{(1)} \\ B_n^{(2)} \\ B_{-n}^{(2)} \end{bmatrix}, \ \mathbf{a} = \begin{bmatrix} A_n^{(1)} \\ A_{-n}^{(1)} \\ A_n^{(2)} \\ A_{-n}^{(2)} \end{bmatrix}. \tag{5.28}$$

Note that for plane wave incidence $A_{\pm n}^{(1)} = A_{\pm n}^{(2)} = A_{\pm n} = i^{\mp n} \mathrm{e}^{-in\theta_0}$. The system of equations (5.28) can be solved as

$$\mathbf{b} = \sum_{j=1}^{4} \lambda_j^{-1} \, \mathbf{e}_j \mathbf{e}_j^T \mathbf{a} \tag{5.29}$$

since $\mathbf{M} = \sum_{j=1}^{4} \lambda_j \, \mathbf{e}_j \mathbf{e}_j^T$ where

$$\begin{aligned} \lambda_1 &= T_n^{-1} + H_0^{(1)}(kb) + H_{2n}^{(1)}(kb), \\ \lambda_2 &= T_n^{-1} - H_0^{(1)}(kb) - H_{2n}^{(1)}(kb), \\ \lambda_3 &= T_n^{-1} + H_0^{(1)}(kb) - H_{2n}^{(1)}(kb), \\ \lambda_4 &= T_n^{-1} - H_0^{(1)}(kb) + H_{2n}^{(1)}(kb), \end{aligned} \tag{5.30}$$

$$\mathbf{e}_1 = \frac{1}{2} \begin{bmatrix} 1 \\ 1 \\ 1 \\ 1 \end{bmatrix}, \ \mathbf{e}_2 = \frac{1}{2} \begin{bmatrix} 1 \\ 1 \\ -1 \\ -1 \end{bmatrix}, \ \mathbf{e}_3 = \frac{1}{2} \begin{bmatrix} 1 \\ -1 \\ 1 \\ -1 \end{bmatrix}, \ \mathbf{e}_4 = \frac{1}{2} \begin{bmatrix} 1 \\ -1 \\ -1 \\ 1 \end{bmatrix}.$$

The explicit solution (5.29) shows the form of the resonance near a zero of λ_j, $j = 1, 2, 3, 4$. Hence, if $\lambda_j \approx 0$ then $\mathbf{b} \propto \mathbf{e}_j$. The eigenvectors $\mathbf{e}_j$ show that the shells either vibrate in phase or π out phase.

At low frequencies where $ka \ll n$, the Hankel functions can be approximated by equations 9.1.8 and 9.1.9 in Ref. [1]

$$H_0^{(1)}(ka) = -H_0^{(2)}(ka) \approx 1 + \frac{2i}{\pi} \ln(ka), \tag{5.31a}$$

$$H_n^{(1)}(ka) = -H_n^{(2)}(ka) \approx \frac{-i\Gamma(n)}{\pi} \left(\frac{ka}{2} \right)^{-n}, \tag{5.31b}$$

where $\Gamma(n)$ is the gamma function. From equation (5.31), it is clear that $\frac{H_n^{(2)\prime}(ka)}{H_n^{(1)\prime}(ka)} = -1$, thus the linearized T-matrix in equation (5.16) simplifies to

$$T_n = \frac{i\epsilon_n}{\Omega_1 - \Omega - i\epsilon_n}. \tag{5.32}$$

Since $H_0^{(1)}(ka) \ll H_n^{(1)}(ka)$ while $ka \ll 1$, the eigenvalues demonstrate the frequency shift Φ_1 of the shells' flexural resonance as $\lambda_j = [(\Omega_1 + \Phi_1) - \Omega - i\epsilon_n]/i\epsilon_n$ for $j = 1, 4$ and $\lambda_j = [(\Omega_1 - \Phi_1) - \Omega - i\epsilon_n]/i\epsilon_n$ for $j = 2, 3$, where $\Phi_1 = i\epsilon_n H_{2n}^{(1)}(ka)$. Using definition (5.17) and (5.31) the frequency shift is

$$\Phi_1 = \frac{\alpha}{1 + \alpha/n}\left(\frac{(2n-1)!}{(n!)^2}\right)\left(\frac{a}{b}\right)^{2n}\Omega_1, \tag{5.33}$$

where $\Gamma(2n) = (2n-1)!$ was applied since n is positive (see also (5.17) for ϵ_n). Note that Φ_1 in equation (5.33) satisfies the necessary limit $\lim_{(b/a)\to\infty} \Phi_1 = 0$. The equation for the frequency split due to two nearby identical scatterers is valid for any scatterer near a local resonance of width ϵ_n. For two nearby thin elastic shells with a flexural resonance width ϵ_n, the shift is large $\Phi_1 \gg \epsilon_n$.

The following Figure 5.4 compares the $n = 2$ and $n = 3$ flexural resonance split Φ_1 for two thin aluminum shells ($h/a = 0.01$, $\alpha = 36.6$) in water using COMSOL eigenfrequency analysis and equation (5.33). The frequency split is nearly identical between theory and finite element simulations for all spacings b. However, the finite element frequencies are shifted up slightly. In general, when the scatterers are close, the frequency split is profound. On the other hand, when they are far from each other, they behave as individual scatterers with the same frequency and the split disappears. The same analysis has been carried out for platinum shells with equally accurate results, implying that the dependence on α in equation (5.33) must be correct. These important results demonstrate that now it is possible to accurately predict the position, width and interaction of flexural resonances on neighbouring thin shells.

5.4.3 Effect on the far-field

Solving equation (5.28) for the scattering coefficients yields

$$B_n^{(j)} = \frac{i\epsilon_n A_n}{(\Omega_1 \pm \Phi_1) - \Omega - i\epsilon_n} \tag{5.34}$$

for even and odd flexural modes n, respectively. Thus the TSCS of equation (3.19) becomes

$$\sigma_{tot} = \frac{r}{a}\int_0^{2\pi} p_s p_s^* d\theta = \frac{4}{ka}\sum_{n=-\infty}^{\infty} |B_n|^2 = \frac{4}{ka}(|B_n^{(j)} + B_{-n}^{(j)}|^2). \tag{5.35}$$

Figure 5.5 shows the TSCS for an aluminum shell with another shell at a close distance $b = 2.2a$. The angle of incidence with respect to the line through the centers of the shells is varied. Firstly, note that the $n = 2$ flexural resonance of the stand alone shell does not appear because it is very narrow. The TSCS does, however, show split resonances of the two shells. From equations (5.30), it is evident that the higher $n = 2$ resonance corresponds to the shells vibrating in phase, while at the $n = 2$ lower resonance they are π out of phase. As a result, Figure 5.5 shows that when a plane wave is incident along the line joining the shell centers, $\theta = 0°$, only the in-phase (upper) resonance propagates into the far-field. At $\theta_0 = 45°$, both resonances are apparent and at $\theta_0 = 90°$ only the out of phase (lower) resonance propagates into the far-field.

In conclusion, it is apparent that due to the interaction of two neighbouring shells, typically evanescent flexural-borne waves can propagate into the far-field. Moreover, it is the angle of incidence which in part determines the magnitude and width of the resonance peaks. The wavelength for this $n = 2$ resonance is very long, implying $\lambda \gg b$. One could imagine that if a particular shell had an $n = 2$ flexural resonance at higher frequencies so that two shells could be spaced on the order of the wavelength, coherent scattering is expected. This notion is investigated in the following Chapter.

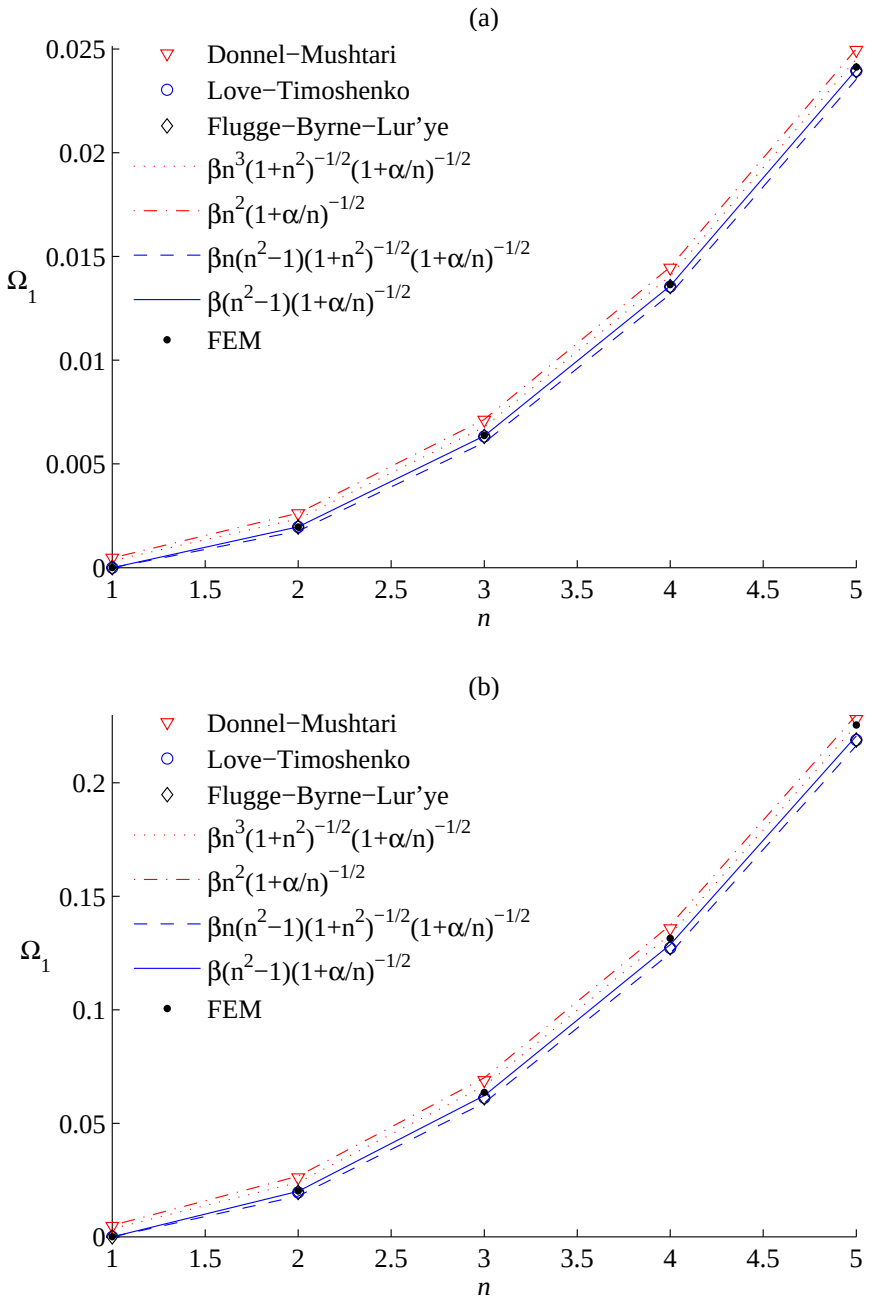

Figure 5.2: Resonance frequencies of the first five flexural modes of vibration for fluid-loaded aluminum shells of thickness to radius ratios $h/a = 0.01$ and $h/a = 0.05$ in plots (a) and (b), respectively. The empty square, circle and triangle markers are the solutions of equations (5.11) for D-M, L-T and F-B-L theories, respectively. The various lines depict the approximate flexural resonance frequencies $\Omega_1^2 = \Omega_r^2(1+\alpha/n)^{-1}$, where the frequencies Ω_r are shown in Table 5.1.

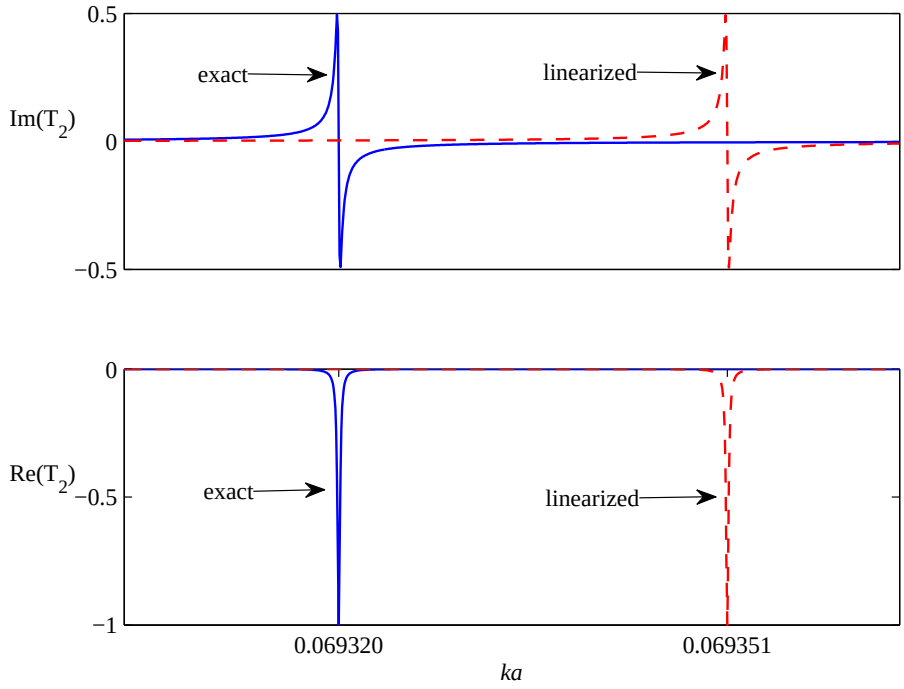

Figure 5.3: The real and imaginary parts of the second term in the T-matrix, T_2, as a function of dimensionless frequency ka for an aluminum shell of thickness to radius ratio $h/a = 0.05$. Exact refers to equation (3.15) and linearized to equation (5.16).

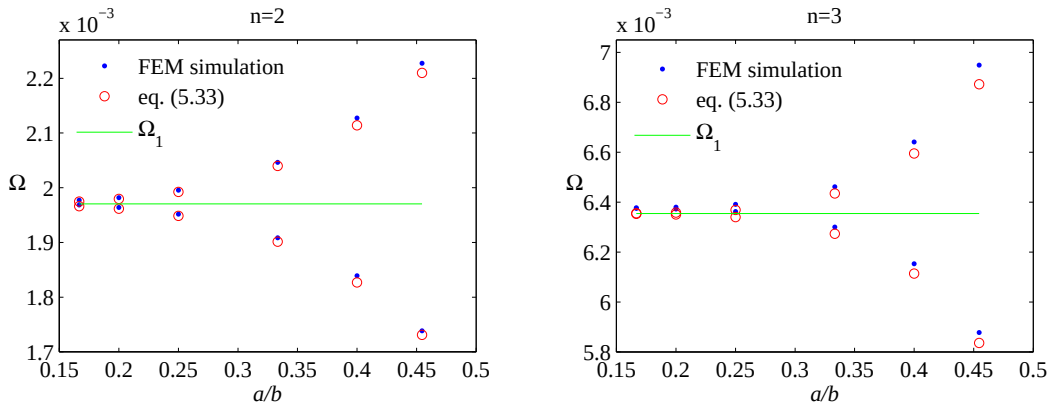

Figure 5.4: Split of the $n = 2$ and $n = 3$ flexural resonances for two aluminum shells of radius a with thickness to radius ratio $h/a = 0.01$ spaced at a distance b. The resonance frequencies Ω_1 are from Figure 5.2(a).

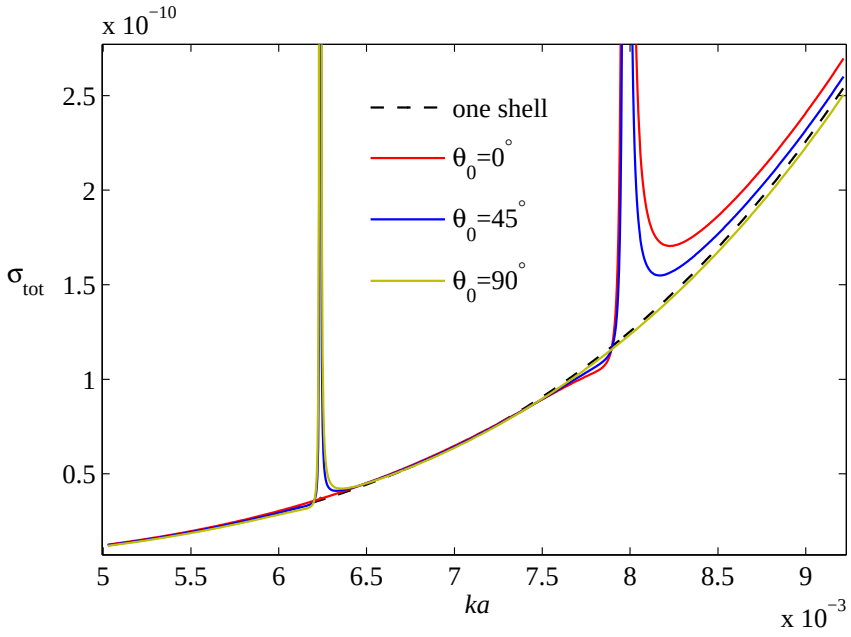

Figure 5.5: TSCS near the $n = 2$ resonance of an aluminum shell with an adjacent identical shell at a distance $b = 2.2a$ for several angles of incidence θ_0.

Chapter 6

Acoustic Poisson-like effect

Wave propagation in a SC is characterized by Bloch waves, which, by virtue of the structural periodicity, can be folded in the wavenumber domain into the smallest indivisible portion of the unit cell, the irreducible Brillouin zone [9]. The resulting band diagrams completely describe the frequency response of the SC, including band gaps (BGs) formed by Bragg scattering when the incident wavelength is close to the lattice constant. Consequently, incident waves of frequency inside a BG cannot propagate through the SC, but decay exponentially, implying that BGs may be interpreted as bands of frequencies associated with a single Bloch wavelength [8]. A complete BG exists when a plane wave at any angle of incidence cannot propagate. Many studies have been conducted to understand the formation of complete BGs and discover ways to increase their bandwidth. These methods involve changing the filling fraction [93, 59, 50], shape [112], lattice [26], orientation [30, 95, 86] and the relative impedance and or density of the scatterer [13, 48]. Miyashita [68] compiled a great review article on the topic.

It has been demonstrated that if the scatterer is a circular metal shell, there exists a unique thickness at which it matches the impedance and index of water [65], maximizing transmission through an array of scatterers. The reason [101] is that although the metal has both stiffness and density greater than water, the effective stiffness and density of the shell are proportional to the thickness-to-radius ratio $\frac{h}{a} < 1$ and therefore a unique value of $\frac{h}{a}$ exists at which the product of stiffness and density equals the square of the acoustic impedance of water. By varying $\frac{h}{a}$ it is also possible to tune either the quasi-static bulk modulus of the shell or its effective density to those of water, but it is rarely possible to match both simultaneously, with some material exceptions [101]. In

particular, the effective sound speed of the shell is almost independent of $\frac{h}{a}$. However, it is possible to match both the density and bulk modulus by inserting an axisymmetric elastic substructure into the shell [101, 102]. Matching the bulk modulus to water removes the monopolar response, while the matched density eliminates dipole radiation, dramatically reducing the scattering at sub-wavelength frequencies. Such control of the quasi-static shell properties facilitates the design of refraction-based lenses [101, 65].

Elastic shells provide rich scattering properties, mainly due to their ability to support highly dispersive flexural waves as described in the previous chapter. Waves scattered from flexural resonances in a SC interact with the propagating Bloch waves forming what are called quasi-band gaps in the band diagram [48]. These asymetric quasi-band gaps can occur at sub-wavelength frequencies. If the flexural resonance frequency is tuned to fall inside the first BG, narrow transmission peaks appear due to coherent scattering. These narrow transmission bands within the BG were used by Khelif et al. [45] to create a narrow pass band filter and later by Pennec et al. [76] for demultiplexing an incident wave. Also, Kosevich et al. [48] observed that the asymmetric profile of the transmission spectrum near the flexural resonance resembles the Fano [21] resonance due to the interference of a discrete autoionized state with a continuum. Kosevich et al. [48] concluded that the BG bandwidth increases when a flexural resonance falls within it.

Another important characteristic of the band diagram for SCs is the presence of antisymmetric (AS) bands. As the name suggests, these modes are polarized in the direction perpendicular to the incident wave. Modes oriented along the incident direction are referred to as symmetric (S) modes. Sanchez-Perez et al. [89] denoted antisymmetric modes in a symmetrically insonified (normal incidence) square array as *deaf*. This term arose from the fact that their experiment was carried out in air at audible frequencies. The experimental transmission data was compared to the band diagram, obtained with the plane wave expansion method, to show that an axisymmetric mode is not excited by a normal plane wave onto an array of effectively rigid scatterers. Later, Hsiao et al. [41] compared the band structure of steel circular cylinders in water, which was obtained using the periodic-boundary finite element method, to the transmission

simulations as a way of separating out the deaf modes.

In order to fully understand any band structure of a SC one needs to consider not only the propagating, but also the evanescent waves. One way to obtain the evanescent component of the bands is using the extended plane wave expansion method. Romero-Garcia et al. [85] formulated the extended plane wave expansion method and introduced the supercell approximation for SCs with defects as a way to study wave localization. Laude et al. [52] analyzed the band structure of symmetric (circular) and semi-symmetric (semi-circular) inclusions in square and hexagonal arrays. They used generalized Fresnel formulas to argue that antisymmetric modes cannot be excited if the symmetry of the array is preserved. In a thorough analysis of the connection between propagating and evanescent bands, Romero-Garcia et al. [87] point out that the transfer of symmetry from one band to the other is via an evanescent mode. Similarly, repelled bands are connected by an evanescent band. In all of these references it is clear that the deaf modes are coupled to the propagating mode at the boundaries of the band gap, either in real or evanescent regions. However, Botey et al. [7] recently showed for photonic crystals that one can "unlock" evanescent modes from the band gap boundaries resulting in evanescent beams escaping the photonic crystal. The beam forming is caused by the negative group velocity of the unlocked mode constituting negative diffraction. The idea of unlocking evanescent modes is here extended to acoustics where the flexural mode of an elastic shell is the proposed mechanism to unlock an AS mode from the BG boundaries and exhibit perpendicular propagation.

6.1 Quadrupole local resonance in a sonic crystal

The $n = 2$ flexural mode is a constant volume mode (top left of Figure 6.1) that when excited by an incident wave transfers acoustic energy to a normal direction via the quadrupole scattering pattern. The displacement of this mode resembles the Poisson effect in solids, with conceptually similar repercussions, and is here referred to as the *acoustic Poisson-like effect*. As shown in Chapter 5, low order flexural modes are subsonic, scattering an evanescent wave that does not propagate into the far-field. However, in SCs where the lattice constant is on the order of the decay length of the

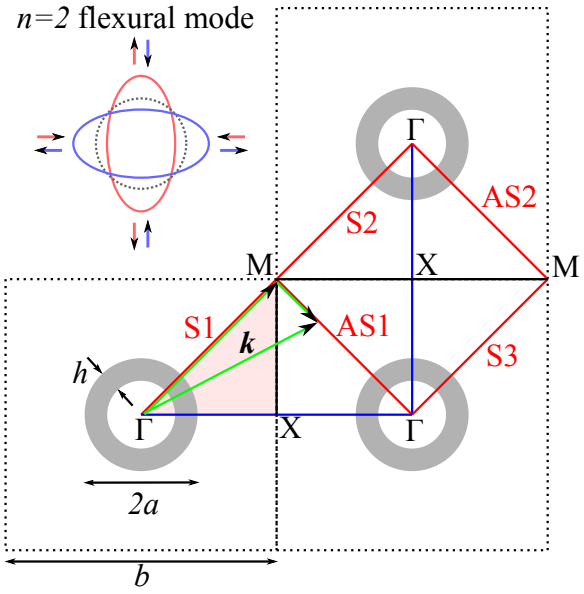

Figure 6.1: The square unit cells marked by dashed lines consist of a shell in water. The first six irreducible Brillouin zones have perimeters ΓXM. The k-vector shown extends into the second Brillouin zone and its projections onto the first and second ΓM axes are labeled S1 and AS1, respectively. The $n = 2$ flexural mode of an elastic shell is also illustrated.

evanescent mode, there is significant interaction between the incident wave and the flexural waves on adjacent shells. The orientation of the scattered quadrupole depends on the direction of incidence. In particular, a perpendicular wave front can emerge if the shells are spaced so that all scattered quadrupoles are in phase (i.e. when the spacing is close to the wavelength) at normal incidence. This is the central idea of the acoustic Poisson-like effect lens.

Consider a SC with a square unit cell of side length b containing a circular elastic shell of outer radius a, thickness h, density ρ_s, shear modulus μ_s, Poisson's ratio ν_s, in water ($\rho = 1000$ kg/m^3, $K = 2.25$ GPa) shown in Figure 6.1. The material, radius and thickness of the shell are selected such that

- the effective bulk modulus of the shell is equal to that of water $K_{eff} = K$, which eliminates the monopolar response,
- the effective density is matched to water $\rho_{eff} = \rho$, removing the sub-wavelength dipolar response and making the SC neutrally buoyant,

- the $n = 2$ flexural resonance is near 20kHz, the designated frequency of interest.

The shell's effective density (see equation (2.13)) has been found to be $\rho_{eff} = \rho_s(2h/a - (h/a)^2)$ and the effective bulk modulus follows from plane strain elasticity as $K_{eff} = \mu_s\big(2(1-\nu_s)\frac{\rho_s}{\rho_{eff}} - 1\big)^{-1}$ (see equation (2.9)).

A thick acrylic shell ($a = 1$ cm, $h = 0.62$ cm) with density, Young's modulus and Poisson's ratio $\rho_s = 1190$ kg/m^3, $E_s = 2(1+\nu_s)\mu_s = 3.2$ GPa, $\nu_s = 0.35$, satisfies these three criteria (see Table 2.2) and has the $n = 2$ flexural resonance at 15678 Hz. The scattered wave from this flexural resonance propagates into the far-field as shown in Figure 3.1 around $ka = 0.7$. Because this acrylic shell is very thick, the bandwidth of the resonance is large. Therefore, this shell introduces a "strong" quadrupole resonance in the SC.

The coherent scattering postulated earlier is expected to occur near the first ΓM BG, but also in the second ΓX BG which will not be considered here. The lattice constant $b = 4.78$ cm is selected so that the $n = 2$ resonance coincides with the first BG in the ΓM direction (see Figure 6.1). The wavelength associated with this BG is $\lambda = \sqrt{2}b$ with a frequency $f = c/(\sqrt{2}b) = 22172$Hz. This shell spacing corresponds to a low filling fraction of $f_s = 0.14$. This value of b is chosen as a balance between

- minimizing the distance from the $n = 2$ resonance to the first ΓM BG,
- minimizing the spacing between shells so as to increase the interaction of scattered waves.

A consequence of having such a low filling fraction is that the transmission through the array is high even in the BG.

6.2 Band diagram

It is important to understand the band structure of a typical SC with inelastic (rigid) scatterers before analyzing the more complicated case of elastic shells. Consider the same square array as described in Section 6.1, but with rigid cylinders of radius $a = 1$ cm and spacing $b = 4.78$ cm in water. The band diagram for this array in Figure 6.2

was obtained using the periodic boundary finite element method in COMSOL. The

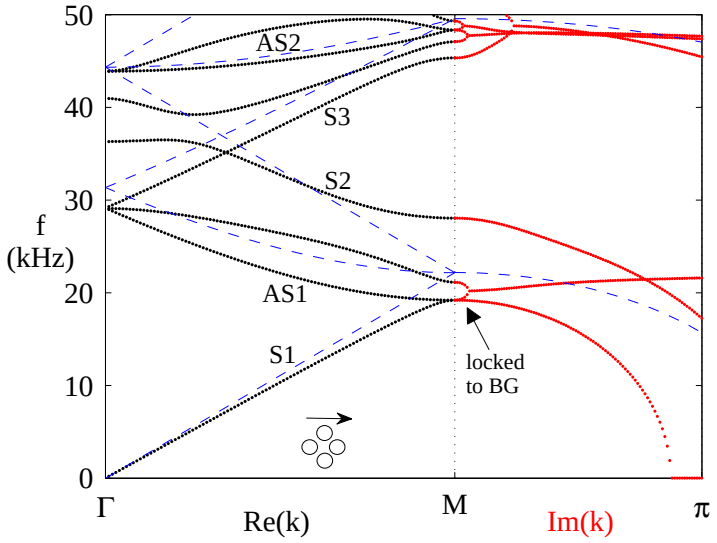

Figure 6.2: Band diagram for a unit cell with a rigid cylinder in water along ΓM direction.

horizontal axis represents the reduced wave vector $\hat{k} = kb \in [0, \sqrt{2}\pi]$ along the ΓM direction and the eigenfrequencies are plotted on the vertical axis in kHz. The origin of each band follows from Figure 6.1, which shows three adjacent unit cells as well as the first six irreducible Brillouin Zones (BZs) of the square array. Also shown in that schematic are the first three symmetric BZ boundaries in red (labeled S1, S2, S3) corresponding to propagation in the (1,1) direction and the first two antisymmetric BZ boundaries (labeled AS1, AS2) corresponding to projected wave vectors in the (1,-1) direction.

Plotted over the rigid cylinder bands (shown with dots) in Figure 6.2 are the bands for the water-only unit cell (shown with dashed lines). It is important to include a homogeneous square unit cell of water with artificial periodic boundary conditions to understand the structure of AS modes. These water-only bands can be thought of as the fundamental or "starting" bands for any SC and can be easily expressed via the geometry of Figure 6.1. Bands S1 and S2 are linear following $f = \frac{c}{2\pi b}\hat{k}$, whereas the AS1 band is $f = \frac{c}{2\pi b}\left(2\pi^2 + (\sqrt{2}\pi - \hat{k})^2\right)^{1/2}$, the AS2 band is $f = \frac{c}{2\pi b}\left(8\pi^2 + \hat{k}^2\right)^{1/2}$, the S3 band is $f = \frac{c}{2\pi b}\left(2\pi^2 + (\sqrt{2}\pi + \hat{k})^2\right)^{1/2}$. It is now clear, that the nonlinearity of some

bands is due to the artificial discretization of space by the triangular irreducible BZ and the projection of the wave vector onto the boundary of an opposing BZ (see green k vector in Figure 6.1).

Even at a filling fraction of $f_s = 0.014$, the rigid cylinder completely changes the band diagram as compared to the water-only case. The S1 and S2 bands at point M split due to Bragg scattering forming a large BG. The two bands inside of the BG (20 to 30 kHz) are the two AS1 modes which differ in phase. One of the AS modes remains locked to the lower BG boundary. These AS modes are not excited in arrays of axisymmetric scatterers. In order to excite the AS mode, the scatterer has to be non-axisymmetric [52], which breaks the geometrical symmetry of the unit cell. Another way to break the unit cell symmetry is with a non-axisymmetrically vibrating scatterer such as the $n = 2$ flexural mode of a shell shown in Figure 6.1.

Also shown on the right of Figure 6.2 are the evanescent bands (in red) which are plotted by fixing the real value of $\hat{k} \rightarrow \sqrt{2}\pi + i\hat{k}$. Each evanescent band approaches zero with increasing wavenumber. More importantly, these bands present a know feature that the deaf AS modes are always locked to the BG boundaries, either directly or by an evanescent band. This is apparent at point M in Figure 6.2 around 20 kHz.

Figure 6.3a shows the band diagram for the same unit cell but with a thick acrylic shell instead. Although this band diagram looks complicated, the bands for the shell-water cell are nearly identical to the basis bands for the water-only cell (dashed lines) with the addition of the $n = 2$ and $n = 3$ flexural bands of the shell. This similarity is due to the tuning of the shell to have the quasi-static properties of water, making the SC acoustically transparent. The shell's matched impedance and index also decreases the bandwidth of the first ΓM BG around 22 kHz. The two $n = 2$ flexural modes near 16 kHz differ in their orientation, one is oriented with the corners and the other with the faces of the square unit cell shown in plots (c) and (d) of Figure 6.3, respectively. The former mode interferes with the S1 symmetric mode resulting in the veering of the bands. The flexural mode oriented with the faces is not directly excited, but rather couples to one of the AS1 modes via an evanescent band (pointed out with a pair of arrows). The flexural mode represents a local resonance and is thus independent of the

periodicity of the host medium. The coupling of a flexural mode to the AS1 band is what unlocks this band from the BG boundaries transferring the incident wave energy to a perpendicular direction. A magnified view of the BG is shown in Figure 6.3b, where the unlocked AS1 band is displayed with a thick line and the other AS1 band remains locked to the lower BG boundary by another evanescent band.

6.3 Redirection of incident energy by 90°

A simulation of a Gaussian beam incident onto the bottom of the array 8 cells deep by 41 cell wide with a frequency of 22350 Hz is shown in Figure 6.4(a). The absolute pressure field shows very strong beams projecting symmetrically from the sides of the array. There is a pressure magnification at the sides of the array as compared to the incident wave, but this can be attributed to the aspect ratio of the array. Also shown in Figure 6.4(b) is the same simulation but at a higher frequency of 27000 Hz, where the beam passes unabated through the array due to the tuning described earlier.

On the right of Figure 6.3b is the energy balance for this array. The transmission and reflection coefficients are obtained by integrating the intensity $\boldsymbol{I}$ over the four sides of the array yielding energy $E = \int \boldsymbol{I} \cdot \boldsymbol{n} \, \mathrm{d}L$ and leading to definitions of the transmission from the side $T_{\text{side}} = E_{\text{left}}/E_{\text{inc}}$, transmission from the back $T = E_{\text{top}}/E_{\text{inc}}$ and reflection from the front $R = 1 - T - 2T_{\text{side}}$. The sideways transmission T_{side} is centered about the BG since it depends on the coherent scattering of shell-borne flexural waves which occurs when the wavelength is on the order of the lattice constant. Therefore this acoustic Poisson-like effect is evident even for a mono-layer of shells, but strengthens with multiple layers. The peak sideways transmission for this array is 46 percent at 22350 Hz.

6.4 Discussion of the results

For comparison purposes Figure 6.5 presents the ΓX band diagram for the shell-water unit cell. By the same arguments as for the first ΓM BG, the $n = 2$ flexural mode

couples to the AS1 band in the second ΓX BG near 30 kHz at $\hat{k} = 0$, but this coupling is so weak that it is only visible at very large imaginary values of the wavenumber. This coupling can be strengthened by increasing the lattice constant, thus lowering the second BG closer to the $n = 2$ band.

Also, the distinction between this acoustic Poisson-like effect and near-zero-index material (NZIM) has to be made. As the name suggests, acoustic NZIM are materials in which either the frequency-dependent density or compressibility go to zero, or both. Chen et al. [14] point out that a NZIM depends on the accidental degeneracy of modes at the center of the BZ (Γ point) where linear dispersion is key. There is evidence that an acoustic NZIM can bend waves when confined in a waveguide [22, 113], but not in the free field as shown here. These materials have also seen cloaking applications [23, 83, 110, 113, 14] because conceptually they stretch the wavelength to infinity making an enclosed object appear small to an incident wave. On the contrary, the acoustic Poisson-like effect is based on an unlocked mode within the BG. Therefore it is not based on refraction, but diffraction and cannot be accurately modelled as an effective acoustic medium, such as a NZIM, precisely due to the field demonstrated in Figure 6.4.

As for the acoustic Poisson-like effect, it is conceivable that 100 percent transmission from the sides of the array can be achieved by increasing the filling fraction and further decreasing the spacing between the first ΓM BG and the flexural mode. This Poisson-like effect is to be present in many other crystals which can support similar $n = 2$ vibrations such as hollow/solid cylinders/spheres embedded in fluid or elastic materials or even non-axisymmetric scatterers on plates for flexural waves. One could even envision this effect for electromagnetic waves in carbon nanotube (CNT) forests, since CNTs do exhibit an $n = 2$ vibrational mode [84].

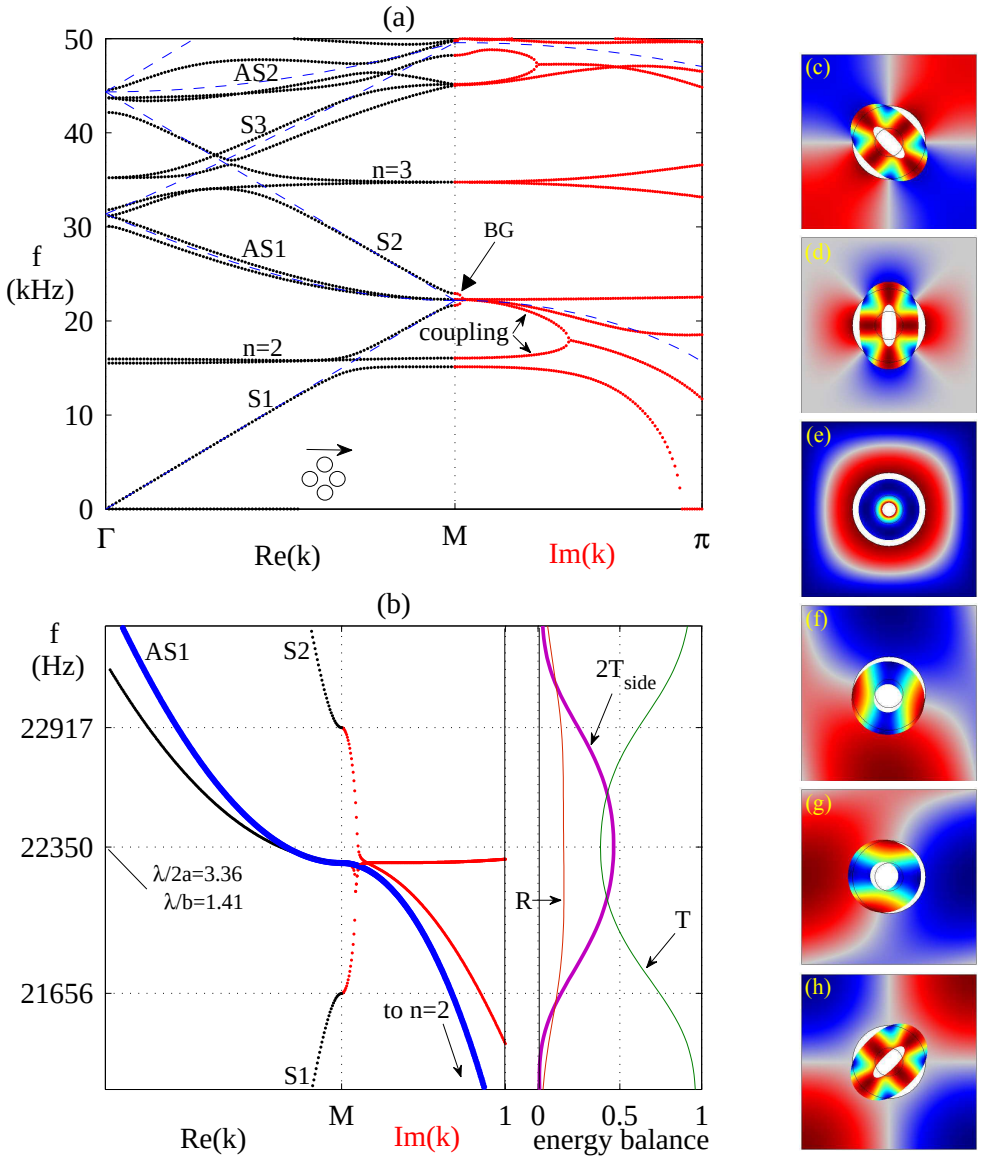

Figure 6.3: (a) Band diagram for unit cell with an acrylic shell along ΓM direction; the dashed lines are the bands for a water-only unit cell. (b) Magnified view of the first BG. The thick curve (blue) is the AS mode which is unlocked from the BG boundaries and locks to the $n = 2$ band. The three adjacent curves on the right show the fraction of the incident energy that goes out of the sides of a finite array T_{side}, the back of the array T and the reflected energy R. The array is 8 shells deep in the direction of incidence and 41 shells wide. (c)-(h) First six modes along the line M in Figure 6.3a, corresponding to $\hat{k} = \sqrt{2}\pi$ in the (1,1) direction. The total pressure and displacement of the shell are shown, emphasizing the mode shapes. The frequencies in plots (c)-(h) are 15123, 16046, 21656, 22275, 22275 and 22917 Hz, respectively. The thick band (blue) in Figure 6.3b at point M is mode (g), which locks to flexural mode (d).

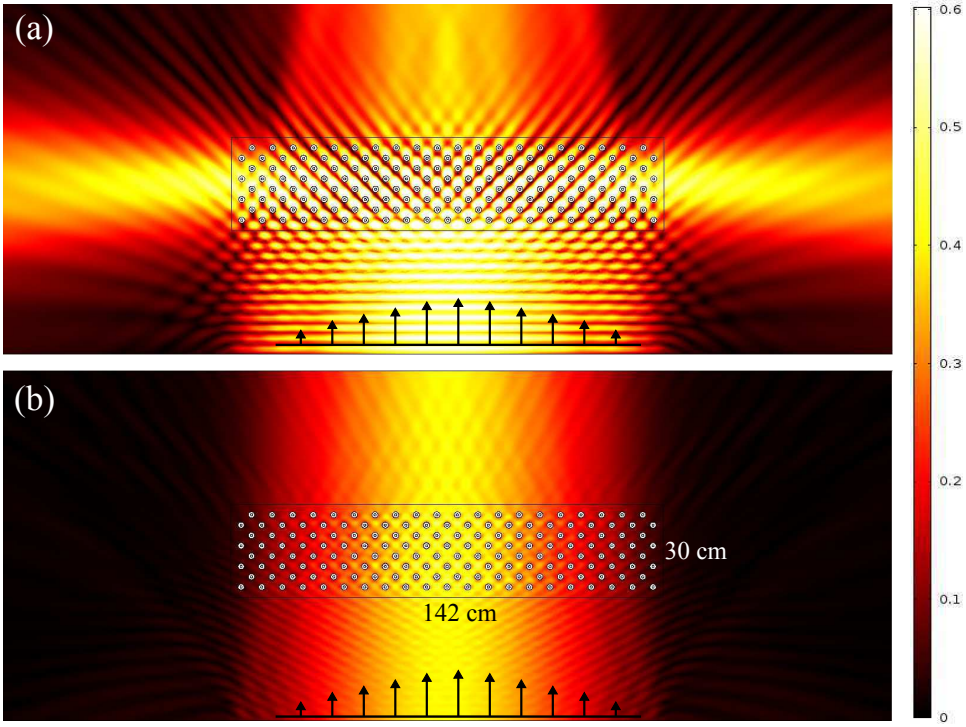

Figure 6.4: Absolute pressure field for a Gaussian beam incident upon an 8×41 array of acrylic shells in water. Plots (a) and (b) are at 22350 Hz and 27000 Hz, respectively.

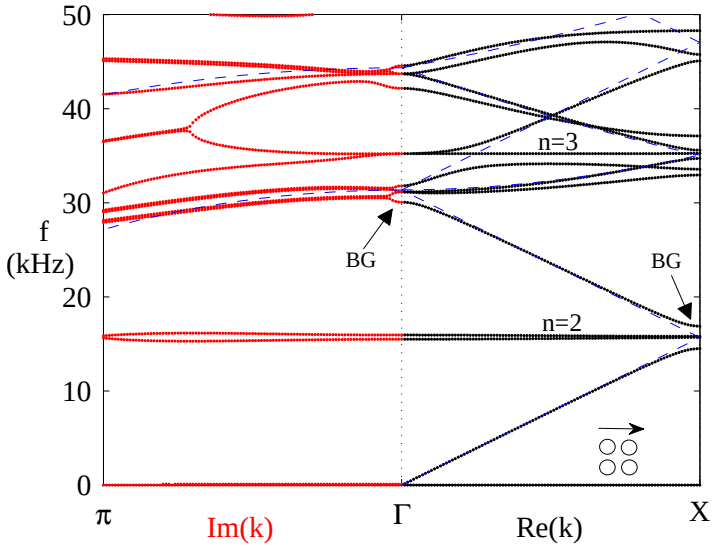

Figure 6.5: Band diagram for a unit cell with an acrylic shell along ΓX direction.

Chapter 7

Effect of shear on an acoustic cloak of the pentamode type

This chapter analyzes the effect of a non-zero shear modulus on the performance of an acoustic cloak of the pentamode type (PM). It begins by describing a perfect pentamode material with an example of a cylindrical PM cloak. However, a structural material for underwater applications must be able to support itself, therefore the shear modulus will not be zero. It is shown how the inclusion of the shear modulus μ alters the constitutive relations. The aim is to explicitly show μ in the general equilibrium equations which can vary throughout the domain of the cloak.

The two scale method [94] will be employed to obtain the desired form of the governing equations. To facilitate this, a second, fast scale ξ will be defined. The change of variables will be performed to yield the equations in terms of X and ξ. To observe the behaviour of the cloak for small values of μ, the shear modulus will be formulated in terms of a perturbation parameter ε. After asymptomatically expanding the displacement vector $\boldsymbol{u}$, the same order terms in ε will be grouped together as they must satisfy the equilibrium equations for all ε. The result is a progressive set of equations to solve for the $\boldsymbol{u}^{(i)}$, where the superscript (i) indicates the order of ε. As an example, the effect of shear on the performance of a 2D rectalinear PM cloak will be investigated.

7.1 An elastic pentamode material mimics water

If an acoustic cloak is to serve its purpose it must mimic the background fluid thereby rendering the cloaked object "invisible". Following the discussion in [71], the properties of the cloak must satisfy three fundamental conditions

- matched impedances at the interface with the background fluid such that there is no reflection,

- equal travel times,
- satisfy Snell-Descartes' Law of refraction.

In order to satisfy these three conditions one must have three degrees of freedom in the design of the cloak. The hardship is that for an isotropic fluid one can only specify the density ρ and the bulk modulus K. Therefore to add another degree of freedom, the isotropic condition needs to be relaxed on either the mass or the stiffness properties of the cloaking fluid. Using anisotropic mass is referred to as inertial cloaking [73], while anisotropic stiffness is facilitated by PM materials.

The general stress-strain relation for a PM material has the form

$$\boldsymbol{\sigma} = K(\boldsymbol{Q} : \boldsymbol{\varepsilon})\boldsymbol{Q}, \quad \text{with} \quad \boldsymbol{\nabla} \cdot \boldsymbol{Q} = 0. \tag{7.1}$$

where $\boldsymbol{Q}$ is a second order tensor yet to be specified and K is the bulk modulus. In mathematical terms, a PM material is a material for which the 6 by 6 elasticity matrix (Voigt notation) has five zero eigenvalues [70]. Aside from isotropic fluids, it has been shown that such materials can be created from solids with specific micro structures [67].

Following the standard recipe for determining the properties of the cloak, the governing equations will be transformed from a PM solid to an acoustic fluid. This will yield the effective density and stiffness of the cloak. The transformation relates the undeformed variable $\boldsymbol{X} \in \Omega$ with the deformed variable $\boldsymbol{x} \in \omega$ by the deformation gradient defined as

$$\boldsymbol{F} = \frac{\partial \boldsymbol{x}(\boldsymbol{X})}{\partial \boldsymbol{X}} = \boldsymbol{V}\boldsymbol{R}, \tag{7.2}$$

where $\boldsymbol{V}$ is the left stretch tensor and $\boldsymbol{R}$ is the rotation. The components of the deformation gradient $\boldsymbol{F}$ are

$$F_{ij} = \frac{\partial x_i}{\partial X_j} \tag{7.3}$$

and its determinant, which is the volume change, will be denoted as

$$\Lambda = \det(\boldsymbol{F}) = \frac{dv}{dV}. \tag{7.4}$$

The scalar and transformed wave equations are

$$\begin{aligned} \ddot{p} - \frac{K_0}{\rho_0}\nabla^2_{\boldsymbol{X}} p = 0, \qquad \boldsymbol{X} \in \Omega, \\ \ddot{p} - K\nabla_{\boldsymbol{x}} \cdot (\boldsymbol{\rho}^{-1}\nabla_{\boldsymbol{x}} p) = 0, \qquad \boldsymbol{x} \in \omega. \end{aligned} \tag{7.5}$$

Comparing the two equations yields the following relationships for the properties of the cloak.

$$K = K_0\Lambda \quad \text{and} \quad \boldsymbol{\rho} = \rho_0\Lambda\boldsymbol{V}^{-2}. \tag{7.6}$$

Similarly, for a PM material with properties dictated by the tensor $\boldsymbol{Q}$, the relationship between densities and bulk moduli can be shown to be

$$K = K_0\Lambda \quad \text{and} \quad \boldsymbol{\rho} = \rho_0\Lambda\boldsymbol{Q}\boldsymbol{V}^{-2}\boldsymbol{Q}. \tag{7.7}$$

It is now obvious that

the standard a

coustic equations correspond to $\boldsymbol{Q} = \boldsymbol{I}$. It is also possible to design PM cloaks from other PM materials, in which case the properties of the cloak become

$$K = K_0\Lambda \quad \text{and} \quad \boldsymbol{\rho} = \Lambda\boldsymbol{Q}\boldsymbol{F}^{-T}\boldsymbol{Q}_{\boldsymbol{0}}^{-1}\boldsymbol{\rho_0}\boldsymbol{Q}_{\boldsymbol{0}}^{-1}\boldsymbol{F}^{-1}\boldsymbol{Q}, \tag{7.8}$$

where $\boldsymbol{Q_0}$ is the tensor characterizing the elasticity tensor of the initial PM material and $\boldsymbol{\rho_0}$ is its density tensor.

To completely define the transformation for a pentamode material, both the deformation gradient $\boldsymbol{F}$ and the material tensor $\boldsymbol{Q}$ must be specified. This way of transforming the equations of motion can be generalized by the gauge transformation $\boldsymbol{U} = \boldsymbol{G}^T\boldsymbol{u}$ relating the displacement in the undeformed configuration $\boldsymbol{U} \in \Omega$ to that in the deformed configuration $\boldsymbol{u} \in \omega$. The essential property is that the Lagrangian is invariant under a gauge transformation. It has been shown [71] that the tensor $\boldsymbol{G}$ is related to the tensor $\boldsymbol{Q}$ by

$$\boldsymbol{G}^T = \Lambda\boldsymbol{F}^{-1}\boldsymbol{Q}. \tag{7.9}$$

For the transformation to be fully defined one needs to specify at least two out of the three tensors $\boldsymbol{F}$, $\boldsymbol{Q}$, and $\boldsymbol{G}$. The following table summarizes the possible scenarios.

Consider a PM material for which the tensor $\boldsymbol{Q}$ is defined as

$$\boldsymbol{Q} = \Lambda^{-1}\boldsymbol{V}. \tag{7.10}$$

Known	Unknown
$\boldsymbol{F}(\boldsymbol{x}), \boldsymbol{Q}(\boldsymbol{x})$	$\boldsymbol{G}(\boldsymbol{x})$
$\boldsymbol{F}(\boldsymbol{x}), \boldsymbol{G}(\boldsymbol{x})$	$\boldsymbol{Q}(\boldsymbol{x})$

Table 7.1: Combinations of tensors required for transformation (7.9).

Since the rotation tensor is equal to $\boldsymbol{R} = \boldsymbol{I}$, from equation (7.2) the left stretch tensor is $\boldsymbol{V} = \boldsymbol{F}$ and $\boldsymbol{Q}$ becomes

$$\boldsymbol{Q} = \Lambda^{-1}\boldsymbol{F}. \tag{7.11}$$

The gauge transformation corresponding to this choice of $\boldsymbol{F}$ and $\boldsymbol{Q}$ is obtained by substituting (7.11) into equation (7.9).

$$\boldsymbol{G}^T = \boldsymbol{I}. \tag{7.12}$$

This result suggests that the transformed displacements, $\boldsymbol{u}$, will equal the physical displacements, $\boldsymbol{U}$. The particular form of equation (7.10) is chosen because it simplifies equations (7.7). Substituting equation (7.10) into (7.7) yields

$$K = K_0\Lambda \quad \text{and} \quad \boldsymbol{\rho} = \rho_0\Lambda^{-1}\boldsymbol{I}. \tag{7.13}$$

7.1.1 Example: A cylindrical PM cloak

In this subsection, the required properties of a cylindrical PM cloak are determined. The polar coordinates in the undeformed configuration are (r, θ) with unit vectors $(\vec{e_r}, \vec{e_\theta})$. The radial position of a point in the undeformed and deformed configurations, respectively, is given by the vectors

$$\vec{X} = R\vec{e_r} \quad \text{and} \quad \vec{x} = r\vec{e_r}. \tag{7.14}$$

Note that the radial direction is kept the same. We will denote the derivative of r as $\frac{dr}{dR} = r'$. Using this notation, the deformation gradient, as derived in Appendix B, is given by

$$\boldsymbol{F} = r'\vec{e_r}\vec{e_r} + \frac{r}{R}\vec{e_\theta}\vec{e_\theta}, \text{ or in matrix form } \quad \Big[\boldsymbol{F}\Big] = \begin{bmatrix} r' & 0 \\ 0 & \frac{r}{R} \end{bmatrix}, \tag{7.15}$$

and its determinant is equal to

$$\det(\boldsymbol{F}) = \Lambda = \frac{rr'}{R}. \tag{7.16}$$

Substituting the value of Λ from equation (7.16) into equation (7.13)

$$K = K_0 \frac{rr'}{R} \quad \text{and} \quad \rho_r = \rho_\theta = \rho_0 \frac{R}{rr'}. \tag{7.17}$$

We can now determine the elasticity tensor, $\boldsymbol{C}$, for this material. The general form of $\boldsymbol{C}$ is

$$\boldsymbol{C} = K\boldsymbol{Q} \otimes \boldsymbol{Q}. \tag{7.18}$$

Substituting $\boldsymbol{Q} = \Lambda^{-1}\boldsymbol{F}$ into equation (7.18), $\boldsymbol{C}$ becomes

$$\boldsymbol{C} = K_0 \Lambda^{-1} \boldsymbol{F} \otimes \boldsymbol{F}. \tag{7.19}$$

Using equations (7.15) and (7.16), we can write equation (7.19) as

$$\begin{aligned}\boldsymbol{C} &= \frac{K_0}{\frac{rr'}{R}} \left[(r')^2 \vec{e_r}\vec{e_r}\vec{e_r}\vec{e_r} + \left(\frac{r}{R}\right)(r') \vec{e_r}\vec{e_r}\vec{e_\theta}\vec{e_\theta} + \left(\frac{r}{R}\right)(r') \vec{e_\theta}\vec{e_\theta}\vec{e_r}\vec{e_r} + \left(\frac{r}{R}\right)^2 \vec{e_\theta}\vec{e_\theta}\vec{e_\theta}\vec{e_\theta} \right] \\ &= K_0 \left[\left(\frac{Rr'}{r}\right) \vec{e_r}\vec{e_r}\vec{e_r}\vec{e_r} + \vec{e_r}\vec{e_r}\vec{e_\theta}\vec{e_\theta} + \vec{e_\theta}\vec{e_\theta}\vec{e_r}\vec{e_r} + \left(\frac{r}{Rr'}\right) \vec{e_\theta}\vec{e_\theta}\vec{e_\theta}\vec{e_\theta} \right].\end{aligned} \tag{7.20}$$

Voigt notation is used to express the components of the elasticity tensor in matrix form. The indices of the elasticity tensor are redefined such that $ij \to I$ and $kl \to J$. This change in notation is illustrated below.

$$\begin{array}{rccccccc} ij = & 11 & 22 & 33 & 23,32 & 13,31 & 12,21 \\ & \Downarrow & \Downarrow & \Downarrow & \Downarrow & \Downarrow & \Downarrow & \Downarrow \\ I = & 1 & 2 & 3 & 4 & 5 & 6 \end{array} \tag{7.21}$$

This matrix becomes

$$\Big[\boldsymbol{C}\Big] = \begin{bmatrix} C_{11} & C_{12} & 0 & 0 & 0 & 0 \\ C_{12} & C_{22} & 0 & 0 & 0 & 0 \\ 0 & 0 & 0 & 0 & 0 & 0 \\ 0 & 0 & 0 & 0 & 0 & 0 \\ 0 & 0 & 0 & 0 & 0 & 0 \\ 0 & 0 & 0 & 0 & 0 & 2C_{66} \end{bmatrix} = K_0 \begin{bmatrix} \frac{Rr'}{r} & 1 & 0 & 0 & 0 & 0 \\ 1 & \frac{r}{Rr'} & 0 & 0 & 0 & 0 \\ 0 & 0 & 0 & 0 & 0 & 0 \\ 0 & 0 & 0 & 0 & 0 & 0 \\ 0 & 0 & 0 & 0 & 0 & 0 \\ 0 & 0 & 0 & 0 & 0 & 0 \end{bmatrix}. \tag{7.22}$$

There is no shear in a perfect PM material, thus the $2C_{66}$ term vanishes. As a matter of fact, only one of the six eigenvalues of $[\boldsymbol{C}]$ is non-zero. The eigenvalues, C_i^0, of the elasticity matrix for this pentamode material are

$$C_i^0 = \begin{cases} K_0 \left(\frac{Rr'}{r} + \frac{r}{Rr'} \right) & i = 1 \\ 0 & i = 2, 3, 4, 5, 6. \end{cases} \tag{7.23}$$

The aim is to specify the material properties so that a rigid cylinder of radius a in water covered by a PM layer of outer radius b looks like a smaller cylinder of radius a' surrounded by a layer of water of thickness $b - a'$. This can be achieved with a linear transformation is $R \to r = AR - B$, where the constants are

$$A = \frac{b - a'}{b - a}, \quad B = b\frac{a - a'}{b - a}. \tag{7.24}$$

Substituting into matrix (7.22) yields

$$C_{11} = C_{22}^{-1} = \frac{AR}{AR - B} = \frac{r}{r + B}. \tag{7.25}$$

7.2 General equations with shear

Consider the general equilibrium equations with shear present. The equation is similar to Navier's equation of elastodynamics except that the shear modulus will not be assumed a constant. The components of the elasticity tensor are given by

$$C_{ijkl} = KQ_{ij}Q_{kl} + \mu(\delta_{ik}\delta_{jl} + \delta_{il}\delta_{jk}), \tag{7.26}$$

where K is the position dependent bulk modulus of the PM cloak at zero shear and μ is the shear modulus. An important point to make is that K behaves like Lame's first constant λ, but since the shear modulus affects the bulk modulus, μ must be added to the diagonal elements of the elasticity matrix as is done in (7.26). The equilibrium equations are

$$\left(C_{ijkl}u_{k,l}\right)_{,j} + \rho\omega^2 u_i = 0. \tag{7.27}$$

Substituting (7.26) into above yields

$$\left(C_{ijkl}^{PM}u_{k,l}\right)_{,j} + \rho\omega^2 u_i + \left(\mu\left(u_{i,j} + u_{j,i}\right)\right)_{,j} = 0. \tag{7.28}$$

We know that without shear, the PM cloak "works" (recovers the scalar wave equation when transformed back to physical coordinates), so lets investigate how the last term contributes to its performance. Distributing the derivative on the last term gives

$$\left(\mu\left(u_{i,j}+u_{j,i}\right)\right)_{,j}=\mu\left(\frac{\partial^2 u_i}{\partial x_j\partial x_j}+\frac{\partial^2 u_j}{\partial x_i\partial x_j}\right)+\frac{\partial\mu}{\partial x_j}\left(\frac{\partial u_i}{\partial x_j}+\frac{\partial u_j}{\partial x_i}\right). \tag{7.29}$$

Equation (7.29) is written in terms of the transformed space coordinates, x_i . Instead, we would like to rewrite it in terms of the physical coordinates X (the slow scale) as well as the fast scale coordinates ξ, where ξ is defined as

$$\boldsymbol{\xi}=\frac{\boldsymbol{x}}{\varepsilon}, \tag{7.30}$$

and ε is the perturbation parameter, yet to be defined. We can now apply equation (7.30) to transform the shear term (7.28) from $\boldsymbol{x}$ to $\boldsymbol{X}$ and $\boldsymbol{\xi}$ coordinates. Note that $\frac{\partial\xi_i}{\partial x_j}=\frac{1}{\varepsilon}\delta_{ij}$ and $\frac{\partial X_k}{\partial x_j}=F^{-1}_{kj}$. The first derivative is related as

$$\frac{\partial}{\partial x_j}=F^{-1}_{kj}\frac{\partial}{\partial X_k}+\frac{1}{\varepsilon}\frac{\partial}{\partial\xi_j}, \tag{7.31}$$

and with some work it can be shown that the second derivative is

$$\begin{aligned}\frac{\partial^2}{\partial x_i\partial x_j}=&F^{-1}_{ni}\frac{\partial(F^{-1}_{kj})}{\partial X_n}\frac{\partial}{\partial X_k}+F^{-1}_{ni}F^{-1}_{kj}\frac{\partial^2}{\partial X_n\partial X_k}+\frac{1}{\varepsilon}F^{-1}_{ni}\frac{\partial^2}{\partial X_n\partial\xi_j}\\&+\frac{1}{\varepsilon}\frac{\partial(F^{-1}_{kj})}{\partial\xi_i}\frac{\partial}{\partial X_k}+\frac{1}{\varepsilon}F^{-1}_{kj}\frac{\partial^2}{\partial\xi_i\partial X_k}+\frac{1}{\varepsilon^2}\frac{\partial^2}{\partial\xi_i\partial\xi_j}\\=&\frac{1}{\varepsilon^2}\frac{\partial^2}{\partial\xi_i\partial\xi_j}+\frac{1}{\varepsilon}\left(F^{-1}_{ni}\frac{\partial^2}{\partial X_n\partial\xi_j}+F^{-1}_{kj}\frac{\partial^2}{\partial\xi_i\partial X_k}+\frac{\partial(F^{-1}_{kj})}{\partial\xi_i}\frac{\partial}{\partial X_k}\right)\\&+F^{-1}_{ni}\left(\frac{\partial(F^{-1}_{kj})}{\partial X_n}\frac{\partial}{\partial X_k}+F^{-1}_{kj}\frac{\partial^2}{\partial X_n\partial X_k}\right).\end{aligned} \tag{7.32}$$

and since the deformation gradient (Jacobian of the transformation function) varies on the scale of X, $\frac{\partial F_{ij}}{\partial\xi_i}=0$, and we get

$$\begin{aligned}\frac{\partial^2}{\partial x_i\partial x_j}=&\frac{1}{\varepsilon^2}\frac{\partial^2}{\partial\xi_i\partial\xi_j}+\frac{1}{\varepsilon}\left(F^{-1}_{ni}\frac{\partial^2}{\partial X_n\partial\xi_j}+F^{-1}_{kj}\frac{\partial^2}{\partial\xi_i\partial X_k}\right)\\&+F^{-1}_{ni}\left(\frac{\partial(F^{-1}_{kj})}{\partial X_n}\frac{\partial}{\partial X_k}+F^{-1}_{kj}\frac{\partial^2}{\partial X_n\partial X_k}\right).\end{aligned} \tag{7.33}$$

Applying the derivative relations (7.31) and (7.33) to the shear term in (7.29) yields

$$\begin{aligned}
&\left(\mu\left(u_{i,j}+u_{j,i}\right)\right)_{,j} = \\
&\frac{\mu}{\varepsilon^2}\left(\frac{\partial^2 u_i}{\partial\xi_j\partial\xi_j}+\frac{\partial^2 u_j}{\partial\xi_i\partial\xi_j}\right)+\frac{\mu}{\varepsilon}\left(2F_{kj}^{-1}\frac{\partial^2 u_i}{\partial X_k\partial\xi_j}+F_{ni}^{-1}\frac{\partial^2 u_j}{\partial X_n\partial\xi_j}+F_{kj}^{-1}\frac{\partial^2 u_j}{\partial X_k\partial\xi_i}\right) \\
&+\mu\Bigg(F_{nj}^{-1}\frac{\partial(F_{kj}^{-1})}{\partial X_n}\frac{\partial u_i}{\partial X_k}+F_{ni}^{-1}\frac{\partial(F_{kj}^{-1})}{\partial X_n}\frac{\partial u_j}{\partial X_k} \\
&+F_{nj}^{-1}F_{kj}^{-1}\frac{\partial^2 u_i}{\partial X_n\partial X_k}+F_{ni}^{-1}F_{kj}^{-1}\frac{\partial^2 u_j}{\partial X_n\partial X_k}\Bigg) \\
&+\frac{1}{\varepsilon}\left(\frac{\partial\mu}{\partial x_j}\right)\left(\frac{\partial u_i}{\partial\xi_j}+\frac{\partial u_j}{\partial\xi_i}\right)+\left(\frac{\partial\mu}{\partial x_j}\right)\left(F_{kj}^{-1}\frac{\partial u_i}{\partial X_k}+F_{ki}^{-1}\frac{\partial u_j}{\partial X_k}\right).
\end{aligned} \tag{7.34}$$

Note that the shear modulus μ is a physical property of the cloak and is therefore a function of the physical coordinates $\boldsymbol{X}$. Since we are interested in analysing the equilibrium equations for small values of μ, let us define it as follows

$$\mu = \varepsilon^2\bar{\mu}(\boldsymbol{X}), \tag{7.35}$$

where ε is the perturbation parameter such that $\varepsilon \ll 1$. We can now relate the derivative of μ, $\frac{\partial\mu}{\partial x_j}$, as follows

$$\frac{\partial\mu}{\partial x_j} = F_{kj}^{-1}\frac{\partial\mu}{\partial X_k} = \varepsilon^2 F_{kj}^{-1}\frac{\partial\bar{\mu}(\boldsymbol{X})}{\partial X_k}. \tag{7.36}$$

Substituting equation (7.36) into equation (7.34) yields the shear term as

$$\begin{aligned}
&\left(\mu\left(u_{i,j}+u_{j,i}\right)\right)_{,j} = \\
&\bar{\mu}\left(\frac{\partial^2 u_i}{\partial\xi_j\partial\xi_j}+\frac{\partial^2 u_j}{\partial\xi_i\partial\xi_j}\right)+\varepsilon\bar{\mu}\left(2F_{kj}^{-1}\frac{\partial^2 u_i}{\partial X_k\partial\xi_j}+F_{ni}^{-1}\frac{\partial^2 u_j}{\partial X_n\partial\xi_j}+F_{kj}^{-1}\frac{\partial^2 u_j}{\partial X_k\partial\xi_i}\right) \\
&+\varepsilon^2\bar{\mu}\Bigg(F_{nj}^{-1}\frac{\partial(F_{kj}^{-1})}{\partial X_n}\frac{\partial u_i}{\partial X_k}+F_{ni}^{-1}\frac{\partial(F_{kj}^{-1})}{\partial X_n}\frac{\partial u_j}{\partial X_k} \\
&+F_{nj}^{-1}F_{kj}^{-1}\frac{\partial^2 u_i}{\partial X_n\partial X_k}+F_{ni}^{-1}F_{kj}^{-1}\frac{\partial^2 u_j}{\partial X_n\partial X_k}\Bigg) \\
&+\varepsilon\left(F_{kj}^{-1}\frac{\partial\bar{\mu}}{\partial X_k}\right)\left(\frac{\partial u_i}{\partial\xi_j}+\frac{\partial u_j}{\partial\xi_i}\right)+\varepsilon^2\left(F_{mj}^{-1}\frac{\partial\bar{\mu}}{\partial X_m}\right)\left(F_{kj}^{-1}\frac{\partial u_i}{\partial X_k}+F_{ki}^{-1}\frac{\partial u_j}{\partial X_k}\right).
\end{aligned} \tag{7.37}$$

At this point we can expand the displacements as a series in ε leading to

$$u_i(\boldsymbol{X},\boldsymbol{\xi}) = u_i^{(0)}(\boldsymbol{X},\boldsymbol{\xi})+\varepsilon u_i^{(1)}(\boldsymbol{X},\boldsymbol{\xi})+\varepsilon^2 u_i^{(2)}(\boldsymbol{X},\boldsymbol{\xi})+\ldots \tag{7.38}$$

as well as the shear contribution

$$\left(\mu\left(u_{i,j}+u_{j,i}\right)\right)_{,j} = s^{(0)}+\varepsilon s^{(1)}+\varepsilon^2 s^{(2)}+\ldots \tag{7.39}$$

Substituting expansion (7.38) into the shear term (7.37) yields the zeroth order term $s^{(0)}$ as

$$s^{(0)} = \bar{\mu}\left(\frac{\partial^2 u_i^{(0)}}{\partial\xi_j\partial\xi_j} + \frac{\partial^2 u_j^{(0)}}{\partial\xi_i\partial\xi_j}\right), \tag{7.40}$$

the first order term $s^{(1)}$ as

$$\begin{aligned} s^{(1)} = {} & \bar{\mu}\left(\frac{\partial^2 u_i^{(1)}}{\partial\xi_j\partial\xi_j} + \frac{\partial^2 u_j^{(1)}}{\partial\xi_i\partial\xi_j}\right) + F_{kj}^{-1}\frac{\partial\bar{\mu}}{\partial X_k}\left(\frac{\partial u_i^{(0)}}{\partial\xi_j} + \frac{\partial u_j^{(0)}}{\partial\xi_i}\right) \\ & + \bar{\mu}\left(2F_{kj}^{-1}\frac{\partial^2 u_i^{(0)}}{\partial X_k\partial\xi_j} + F_{ni}^{-1}\frac{\partial^2 u_j^{(0)}}{\partial X_n\partial\xi_j} + F_{kj}^{-1}\frac{\partial^2 u_j^{(0)}}{\partial X_k\partial\xi_i}\right), \end{aligned} \tag{7.41}$$

and the second order term $s^{(2)}$ as

$$\begin{aligned} s^{(2)} = {} & \bar{\mu}\left(\frac{\partial^2 u_i^{(2)}}{\partial\xi_j\partial\xi_j} + \frac{\partial^2 u_j^{(2)}}{\partial\xi_i\partial\xi_j}\right) + F_{kj}^{-1}\frac{\partial\bar{\mu}}{\partial X_k}\left(\frac{\partial u_i^{(1)}}{\partial\xi_j} + \frac{\partial u_j^{(1)}}{\partial\xi_i}\right) \\ & + \bar{\mu}\left(2F_{kj}^{-1}\frac{\partial^2 u_i^{(1)}}{\partial X_k\partial\xi_j} + F_{ni}^{-1}\frac{\partial^2 u_j^{(1)}}{\partial X_n\partial\xi_j} + F_{kj}^{-1}\frac{\partial^2 u_j^{(1)}}{\partial X_k\partial\xi_i}\right) \\ & + \bar{\mu}\left(F_{nj}^{-1}\frac{\partial(F_{kj}^{-1})}{\partial X_n}\frac{\partial u_i^{(0)}}{\partial X_k} + F_{ni}^{-1}\frac{\partial(F_{kj}^{-1})}{\partial X_n}\frac{\partial u_j^{(0)}}{\partial X_k}\right. \\ & \left. + F_{nj}^{-1}F_{kj}^{-1}\frac{\partial^2 u_i^{(0)}}{\partial X_n\partial X_k} + F_{ni}^{-1}F_{kj}^{-1}\frac{\partial^2 u_j^{(0)}}{\partial X_n\partial X_k}\right) \\ & + F_{mj}^{-1}\frac{\partial\bar{\mu}}{\partial X_m}\left(F_{kj}^{-1}\frac{\partial u_i^{(0)}}{\partial X_k} + F_{ki}^{-1}\frac{\partial u_j^{(0)}}{\partial X_k}\right). \end{aligned} \tag{7.42}$$

7.3 Helmholtz's decomposition

According to Helmholtz's theory, a vector field can be decomposed into the sum of a curl free vector field ϕ and a divergence free vector field ψ if it is smooth and decays fast. This allows us to express the displacements $\boldsymbol{u}^{(0)}$ as

$$\boldsymbol{u}^{(0)}(\boldsymbol{X},\boldsymbol{\xi}) = \boldsymbol{u}^{(0L)}(\boldsymbol{X}) + \boldsymbol{u}^{(0T)}(\boldsymbol{\xi}), \tag{7.43}$$

where the longitudinal and transverse components are defined as

$$\boldsymbol{u}^{(0L)} = \nabla_{\boldsymbol{X}}\phi(\boldsymbol{X}) \quad \text{and} \quad \boldsymbol{u}^{(0T)} = \nabla_{\boldsymbol{\xi}} \wedge \psi(\boldsymbol{\xi}). \tag{7.44}$$

Consequently, the components of the displacement vector are

$$u_i^{(0)} = \frac{\partial\phi(\boldsymbol{X})}{\partial X_i} + e_{ij3}\frac{\partial\psi(\boldsymbol{\xi})}{\partial\xi_j}, \tag{7.45}$$

which in 2D gives

$$u_1^{(0)} = \frac{\partial \phi(\boldsymbol{X})}{\partial X_1} + \frac{\partial \psi(\boldsymbol{\xi})}{\partial \xi_2} \quad \text{and} \quad u_2^{(0)} = \frac{\partial \phi(\boldsymbol{X})}{\partial X_2} - \frac{\partial \psi(\boldsymbol{\xi})}{\partial \xi_1}. \tag{7.46}$$

7.3.1 Zeroth order equation

Substituting the displacement (7.45) into the zeroth order shear contribution (7.40) yields

$$s^{(0)} = \bar{\mu} \left(e_{in3} \frac{\partial^3 \psi}{\partial \xi_n \partial \xi_j \partial \xi_j} + e_{jk3} \frac{\partial^3 \psi}{\partial \xi_k \partial \xi_i \partial \xi_j} \right). \tag{7.47}$$

In 2D Cartesian coordinates the above equation becomes

$$s^{(0)} = \bar{\mu} \left(\frac{\partial}{\partial \xi_2} \nabla_\xi^2(\psi) \vec{e_1} - \frac{\partial}{\partial \xi_1} \nabla_\xi^2(\psi) \vec{e_2} \right). \tag{7.48}$$

Substituting back into equation (7.28) yields the $O(1)$ equilibrium equation as

$$\begin{aligned} &\left(F_{jn}^{-1} \frac{\partial}{\partial X_n} \left(C_{ijkl}^{PM} F_{jm}^{-1} \frac{\partial^2 \phi}{\partial X_m \partial X_k} \right) + \rho \omega^2 \frac{\partial \phi}{\partial X_i} \right) \vec{e_i} \\ &\qquad + \frac{\partial}{\partial \xi_2} \left(\bar{\mu} \nabla_\xi^2(\psi) + \rho \omega^2 \psi \right) \vec{e_1} - \frac{\partial}{\partial \xi_1} \left(\bar{\mu} \nabla_\xi^2(\psi) + \rho \omega^2 \psi \right) \vec{e_2} = 0, \end{aligned} \tag{7.49}$$

where we have assumed that μ and ρ are not functions of ξ. For a pentamode material without shear the equilibrium equation in the physical coordinates simplifies to the scalar acoustic wave equation, therefore equation (7.49) will take on the following form

$$\begin{aligned} &\frac{\partial}{\partial X_i} \left(K_0 \nabla_X^2(\phi) + \rho_0 \omega^2 \phi \right) \vec{e_i} \\ &\qquad + \frac{\partial}{\partial \xi_2} \left(\mu_0 \nabla_\xi^2(\psi) + \rho_0 \omega^2 \psi \right) \vec{e_1} - \frac{\partial}{\partial \xi_1} \left(\mu_0 \nabla_\xi^2(\psi) + \rho_0 \omega^2 \psi \right) \vec{e_2} = 0, \end{aligned} \tag{7.50}$$

where $\mu_0 = \rho^{-1} \rho_0 \bar{\mu} =$, ρ_0 is the density of the background fluid, and K_0 is its bulk modulus. This yields the equations for the longitudinal and transverse displacement potentials, respectively, as

$$\begin{aligned} K_0 \nabla_X^2(\phi) + \rho_0 \omega^2 \phi &= \text{constant}, \\ \mu_0 \nabla_\xi^2(\psi) + \rho_0 \omega^2 \psi &= \text{constant}. \end{aligned} \tag{7.51}$$

7.3.2 First order equation

We can also decompose the second term in the expansion (7.38), by defining two new potential functions, $\phi^{(1)}$ and $\psi^{(1)}$ as

$$u_i^{(1)} = \frac{\partial \phi^{(1)}(\boldsymbol{X})}{\partial X_i} + e_{ij3}\frac{\partial \psi^{(1)}(\boldsymbol{\xi})}{\partial \xi_j} \tag{7.52}$$

Substituting equations (7.45) and (7.52) into the first order equation (7.41) yields

$$\begin{aligned} s^{(1)} = \bar{\mu}&\left[\frac{\partial}{\partial \xi_2}\nabla_\xi^2(\psi^{(1)})\vec{e_1} - \frac{\partial}{\partial \xi_1}\nabla_\xi^2(\psi^{(1)})\vec{e_2}\right] \\ &+ F_{kj}^{-1}\frac{\partial \bar{\mu}}{\partial X_k}\left[\left(\frac{\partial^2\psi^{(0)}}{\partial \xi_j \partial \xi_2} - \frac{\partial^2\psi^{(0)}}{\partial \xi_1^2}\delta_{j2} + \frac{\partial^2\psi^{(0)}}{\partial \xi_1 \partial \xi_2}\delta_{j1}\right)\vec{e_1}\right. \\ &\left.+ \left(-\frac{\partial^2\psi^{(0)}}{\partial \xi_j \partial \xi_1} - \frac{\partial^2\psi^{(0)}}{\partial \xi_1 \partial \xi_2}\delta_{j2} + \frac{\partial^2\psi^{(0)}}{\partial \xi_2^2}\delta_{j1}\right)\vec{e_2}\right], \end{aligned} \tag{7.53}$$

where all of the cross derivatives disappear since both ϕ and ψ depend only on one of the variables. If we assume that the shear modulus is $\mu = \mu(X_1)$ and that the deformation gradient is diagonal, $F_{ij} = 0 \ \forall \ i \neq j$, then equation (7.53) simplifies to

$$\begin{aligned} s^{(1)} = &\left[\bar{\mu}\frac{\partial}{\partial \xi_2}\nabla_\xi^2(\psi^{(1)}) + 2F_{11}^{-1}\frac{\partial \bar{\mu}}{\partial X_1}\frac{\partial^2\psi^{(0)}}{\partial \xi_1 \partial \xi_2}\right]\vec{e_1} \\ &+ \left[-\bar{\mu}\frac{\partial}{\partial \xi_1}\nabla_\xi^2(\psi^{(1)}) + F_{11}^{-1}\frac{\partial \bar{\mu}}{\partial X_1}\left(-\frac{\partial^2\psi^{(0)}}{\partial \xi_1^2} + \frac{\partial^2\psi^{(0)}}{\partial \xi_2^2}\right)\right]\vec{e_2}. \end{aligned} \tag{7.54}$$

Substituting the above result back into equation (7.28) yields

$$\begin{aligned} &\frac{\partial}{\partial X_i}\left[K_0\nabla_X^2(\phi^{(1)}) + \rho_0\omega^2\phi^{(1)}\right]\vec{e_i} \\ &+ \left[\frac{\partial}{\partial \xi_2}\left(\mu_0\nabla_\xi^2(\psi^{(1)}) + \rho_0\omega^2\psi^{(1)}\right) + 2\rho^{-1}\rho_0 F_{11}^{-1}\frac{\partial \bar{\mu}}{\partial X_1}\frac{\partial^2\psi^{(0)}}{\partial \xi_1 \partial \xi_2}\right]\vec{e_1} \\ &- \left[\frac{\partial}{\partial \xi_1}\left(\mu_0\nabla_\xi^2(\psi^{(1)}) + \rho_0\omega^2\psi^{(1)}\right) + \rho^{-1}\rho_0 F_{11}^{-1}\frac{\partial \bar{\mu}}{\partial X_1}\left(\frac{\partial^2\psi^{(0)}}{\partial \xi_1^2} - \frac{\partial^2\psi^{(0)}}{\partial \xi_2^2}\right)\right]\vec{e_2} = 0, \end{aligned} \tag{7.55}$$

which gives the following three equations to be solved for the functions $\phi^{(1)}$ and $\psi^{(1)}$.

$$\begin{aligned} &K_0\nabla_X^2(\phi^{(1)}) + \rho_0\omega^2\phi^{(1)} = \text{constant}, \\ &\frac{\partial}{\partial \xi_2}\left(\mu_0\nabla_\xi^2(\psi^{(1)}) + \rho_0\omega^2\psi^{(1)}\right) = -2\rho^{-1}\rho_0 F_{11}^{-1}\frac{\partial \bar{\mu}}{\partial X_1}\frac{\partial^2\psi^{(0)}}{\partial \xi_1 \partial \xi_2}, \\ &\frac{\partial}{\partial \xi_1}\left(\mu_0\nabla_\xi^2(\psi^{(1)}) + \rho_0\omega^2\psi^{(1)}\right) = -\rho^{-1}\rho_0 F_{11}^{-1}\frac{\partial \bar{\mu}}{\partial X_1}\left(\frac{\partial^2\psi^{(0)}}{\partial \xi_1^2} - \frac{\partial^2\psi^{(0)}}{\partial \xi_2^2}\right). \end{aligned} \tag{7.56}$$

Note that the functions $\phi^{(0)}$ and $\psi^{(0)}$ are solutions of equation (7.51). Furthermore, if $\frac{\partial}{\partial x_2} = \frac{\partial}{\partial X_2} \to \frac{\partial}{\partial \xi_2} = 0$, then equations (7.56) simplify to

$$\begin{aligned} &K_0 \nabla_X^2(\phi^{(1)}) + \rho_0 \omega^2 \phi^{(1)} = \text{constant}, \\ &\mu_0 \nabla_\xi^2(\psi^{(1)}) + \rho_0 \omega^2 \psi^{(1)} = -\rho^{-1} \rho_0 F_{11}^{-1} \frac{\partial \bar{\mu}}{\partial X_1} \frac{\partial \psi^{(0)}}{\partial \xi_1} + \text{constant}. \end{aligned} \tag{7.57}$$

7.3.3 Second order equation

It can be shown that the equilibrium equation of order ε^2 takes the following form

$$\begin{aligned} &\frac{\partial}{\partial X_i} \left[K_0 \nabla_X^2(\phi^{(2)}) + \rho_0 \omega^2 \phi^{(2)} \right] \vec{e_i} \\ &+ \left[\frac{\partial}{\partial \xi_2} \left(\mu_0 \nabla_\xi^2(\psi^{(2)}) + \rho_0 \omega^2 \psi^{(2)} \right) + 2\rho^{-1} \rho_0 F_{11}^{-1} \frac{\partial \bar{\mu}}{\partial X_1} \frac{\partial^2 \psi^{(1)}}{\partial \xi_1 \partial \xi_2} \right] \vec{e_1} \\ &- \left[\frac{\partial}{\partial \xi_1} \left(\mu_0 \nabla_\xi^2(\psi^{(2)}) + \rho_0 \omega^2 \psi^{(2)} \right) + \rho^{-1} \rho_0 F_{11}^{-1} \frac{\partial \bar{\mu}}{\partial X_1} \left(\frac{\partial^2 \psi^{(1)}}{\partial \xi_1^2} - \frac{\partial^2 \psi^{(1)}}{\partial \xi_2^2} \right) \right] \vec{e_2} \\ &+ \mu_0 \Bigg(F_{nj}^{-1} \frac{\partial (F_{kj}^{-1})}{\partial X_n} \frac{\partial^2 \phi^{(0)}}{\partial X_k \partial X_i} + F_{ni}^{-1} \frac{\partial (F_{kj}^{-1})}{\partial X_n} \frac{\partial^2 \phi^{(0)}}{\partial X_k \partial X_j} \\ &+ F_{nj}^{-1} F_{kj}^{-1} \frac{\partial^3 \phi^{(0)}}{\partial X_n \partial X_k \partial X_i} + F_{ni}^{-1} F_{kj}^{-1} \frac{\partial^3 \phi^{(0)}}{\partial X_n \partial X_k \partial X_j} \Bigg) \vec{e_i} \\ &+ \rho^{-1} \rho_0 F_{mj}^{-1} \frac{\partial \bar{\mu}}{\partial X_m} \left(F_{kj}^{-1} \frac{\partial^2 \phi^{(0)}}{\partial X_k \partial X_i} + F_{ki}^{-1} \frac{\partial^2 \phi^{(0)}}{\partial X_k \partial X_j} \right) \vec{e_i} \end{aligned} \tag{7.58}$$

The above is satisfied if

$$\begin{aligned} &\frac{\partial}{\partial X_i} \left(K_0 \nabla_X^2(\phi^{(2)}) + \rho_0 \omega^2 \phi^{(2)} \right) = f_i(\boldsymbol{X}) \\ &\frac{\partial}{\partial \xi_2} \left(\mu_0 \nabla_\xi^2(\psi^{(2)}) + \rho_0 \omega^2 \psi^{(2)} \right) = g(\boldsymbol{X}, \boldsymbol{\xi}) \\ &\frac{\partial}{\partial \xi_1} \left(\mu_0 \nabla_\xi^2(\psi^{(2)}) + \rho_0 \omega^2 \psi^{(2)} \right) = h(\boldsymbol{X}, \boldsymbol{\xi}) \end{aligned} \tag{7.59}$$

where

$$
\begin{aligned}
f_i(\boldsymbol{X}) = -\mu_0 \Bigg(& F^{-1}_{nj} \frac{\partial (F^{-1}_{kj})}{\partial X_n} \frac{\partial^2 \phi^{(0)}}{\partial X_k \partial X_i} + F^{-1}_{ni} \frac{\partial (F^{-1}_{kj})}{\partial X_n} \frac{\partial^2 \phi^{(0)}}{\partial X_k \partial X_j} \\
& + F^{-1}_{nj} F^{-1}_{kj} \frac{\partial^3 \phi^{(0)}}{\partial X_n \partial X_k \partial X_i} + F^{-1}_{ni} F^{-1}_{kj} \frac{\partial^3 \phi^{(0)}}{\partial X_n \partial X_k \partial X_j} \Bigg) \\
& - \rho^{-1} \rho_0 F^{-1}_{mj} \frac{\partial \bar{\mu}}{\partial X_m} \left(F^{-1}_{kj} \frac{\partial^2 \phi^{(0)}}{\partial X_k \partial X_i} + F^{-1}_{ki} \frac{\partial^2 \phi^{(0)}}{\partial X_k \partial X_j} \right), \qquad (7.60) \\
g(\boldsymbol{X}, \boldsymbol{\xi}) = & -2\rho^{-1} \rho_0 F^{-1}_{11} \frac{\partial \bar{\mu}}{\partial X_1} \frac{\partial^2 \psi^{(1)}}{\partial \xi_1 \partial \xi_2}, \\
h(\boldsymbol{X}, \boldsymbol{\xi}) = & -\rho^{-1} \rho_0 F^{-1}_{11} \frac{\partial \bar{\mu}}{\partial X_1} \left(\frac{\partial^2 \psi^{(1)}}{\partial \xi_1^2} - \frac{\partial^2 \psi^{(1)}}{\partial \xi_2^2} \right).
\end{aligned}
$$

As a result, equations (7.51), (7.56) and (7.59) form a set to be solved for the six potentials $\phi^{(0)}, \phi^{(1)}, \phi^{(2)}, \psi^{(0)}, \psi^{(1)}, \psi^{(2)}$ illuminating the contribution of shear up to order ε^2.

7.4 Effect of shear on a 2D rectilinear PM cloak

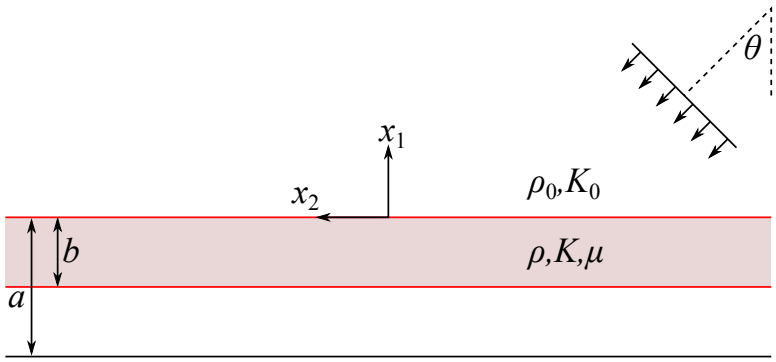

Figure 7.1: 2D PM cloak with a non-zero shear modulus.

Consider the PM slab of thickness b at a distance $(a - b)$ from a rigid surface as shown in Figure 7.1. The transformation to necessary to cloak the region below the slab yields the deformation gradient

$$
\boldsymbol{F} = \begin{bmatrix} x' & 0 \\ 0 & 1 \end{bmatrix}, \qquad (7.61)
$$

where $x' = \frac{dx_1}{dX_1} = \frac{b}{a}$ for this example and the (x_1, x_2) and (X_1, X_2) coordinate systems are coincident. Using equation (7.19), the elasticity tensor is defined as $\boldsymbol{C}^{PM} =$

$K_0\Lambda^{-1}\boldsymbol{F}\otimes\boldsymbol{F}$, where the non-zero components are

$$\begin{aligned} C_{11}^{PM} &= K_0 x' + 2\mu, \\ C_{12}^{PM} &= C_{21}^{PM} = K_0, \\ C_{22}^{PM} &= K_0\frac{1}{x'} + 2\mu. \end{aligned} \tag{7.62}$$

Note that a shear modulus has been included in the diagonal terms. The required isotropic density follows from equation (7.13)

$$\rho_{x_1} = \rho_{x_2} = \rho = \frac{\rho_0}{x'}. \tag{7.63}$$

In order to solve equations (7.51), (7.56) and (7.59) for this example, the boundary conditions need to be specified. To apply the boundary conditions, the normal and shear stresses need to be expressed in terms of the potential functions ϕ and ψ in the (x_1,x_2) coordinates.

7.4.1 Perturbed normal stress

Using (7.62), the normal stress in the x_1 direction at a point $\boldsymbol{x_0}$ is given by

$$\begin{aligned} \sigma_{11}\Big|_{\boldsymbol{x}=\boldsymbol{x_0}} &= C_{11}^{PM}\frac{\partial u_1}{\partial x_1} + C_{12}^{PM}\frac{\partial u_2}{\partial x_2} + 2\mu\frac{\partial u_1}{\partial x_1}\Big|_{\boldsymbol{x}=\boldsymbol{x_0}}, \\ &= K_0 x'\frac{\partial u_1}{\partial x_1} + K_0\frac{\partial u_2}{\partial x_2} + 2\mu\frac{\partial u_1}{\partial x_1}\Big|_{\boldsymbol{x}=\boldsymbol{x_0}}. \end{aligned} \tag{7.64}$$

Substituting the shear expression (7.35) into above as well as changing variables according to (7.31) yields

$$\begin{aligned} \sigma_{11}\Big|_{\boldsymbol{x}=\boldsymbol{x_0}} = \frac{1}{\varepsilon}\left(K_0 x'\frac{\partial u_1}{\partial \xi_1} + K_0\frac{\partial u_2}{\partial \xi_2}\right) + \left(K_0 x' F_{1k}^{-1}\frac{\partial u_1}{\partial X_k} + K_0 F_{2m}^{-1}\frac{\partial u_2}{\partial X_m}\right) \\ + \varepsilon\left(2\bar{\mu}\frac{\partial u_1}{\partial \xi_1}\right) + \varepsilon^2\left(2\bar{\mu}F_{1n}^{-1}\frac{\partial u_1}{\partial X_n}\right)\Big|_{\boldsymbol{x}=\boldsymbol{x_0}}. \end{aligned} \tag{7.65}$$

At this stage, to simplify the analysis assume the following dependence on the transverse variables.

$$\frac{\partial()}{\partial X_2} = ik_2(), \quad \frac{\partial()}{\partial \xi_2} = i\varepsilon k_2(), \tag{7.66}$$

where k_2 is the wavevector in the x_2 direction. Then, decomposing the displacements in terms of the potential functions $\phi(X_1, X_2)$ and $\psi(\xi_1, \xi_2)$ yields

$$\begin{aligned} u_1^{(i)} &= \frac{\partial \phi^{(i)}}{\partial X_1} + \frac{\partial \psi^{(i)}}{\partial \xi_2} = \frac{\partial \phi^{(i)}}{\partial X_1} + i\varepsilon k_2 \psi^{(i)}, \\ u_2^{(i)} &= \frac{\partial \phi^{(i)}}{\partial X_2} - \frac{\partial \psi^{(i)}}{\partial \xi_1} = ik_2 \phi^{(i)} - \frac{\partial \psi^{(i)}}{\partial \xi_1}, \end{aligned} \tag{7.67}$$

where the superscript (i) denotes the order of ε from expansion (7.38). Substituting equations (7.67) into equation (7.65) and combining terms of the same order of ε yields the components of the normal stress as

$$\begin{aligned} O(1) \rightarrow & K_0(x' - 1) ik_2 \frac{\partial \psi^{(0)}}{\partial \xi_1} + k_0 \left(\frac{\partial^2 \phi^{(0)}}{\partial {X_1}^2} - k_2^2 \phi^{(0)} \right) \Bigg|_{\boldsymbol{x}=\boldsymbol{x_0}}, \\ O(\varepsilon) \rightarrow & K_0(x' - 1) ik_2 \frac{\partial \psi^{(1)}}{\partial \xi_1} + k_0 \left(\frac{\partial^2 \phi^{(1)}}{\partial {X_1}^2} - k_2^2 \phi^{(1)} \right) \Bigg|_{\boldsymbol{x}=\boldsymbol{x_0}}, \\ O(\varepsilon^2) \rightarrow & K_0(x' - 1) ik_2 \frac{\partial \psi^{(2)}}{\partial \xi_1} + k_0 \left(\frac{\partial^2 \phi^{(2)}}{\partial {X_1}^2} - k_2^2 \phi^{(2)} \right) \\ & + 2\bar{\mu} \left(ik_2 \frac{\partial \psi^{(0)}}{\partial \xi_1} + F_{11}^{-1} \frac{\partial^2 \phi^{(0)}}{\partial {X_1}^2} \right) \Bigg|_{\boldsymbol{x}=\boldsymbol{x_0}}. \end{aligned} \tag{7.68}$$

7.4.2 Perturbed shear stress

Now using (7.62), the shear stress at some point $\boldsymbol{x_0}$ within the cloak is given by

$$\sigma_{12}\Big|_{\boldsymbol{x}=\boldsymbol{x_0}} = 2C_{66}\varepsilon_{12}\Big|_{\boldsymbol{x}=\boldsymbol{x_0}} = \mu \left(\frac{\partial u_2}{\partial x_1} + \frac{\partial u_1}{\partial x_2} \right) \Bigg|_{\boldsymbol{x}=\boldsymbol{x_0}}. \tag{7.69}$$

Changing variables according to (7.31) and using definition (7.35) yields

$$\sigma_{12}\Big|_{\boldsymbol{x}=\boldsymbol{x_0}} = \varepsilon\bar{\mu} \left(\frac{\partial u_2}{\partial \xi_1} + \frac{\partial u_1}{\partial \xi_2} \right) + \varepsilon^2 \bar{\mu} \left(F_{1k}^{-1} \frac{\partial u_2}{\partial X_k} + F_{2k}^{-1} \frac{\partial u_1}{\partial X_k} \right) \Bigg|_{\boldsymbol{x}=\boldsymbol{x_0}}. \tag{7.70}$$

If we now decompose the displacements as was done in the previous section (equation (7.67)), we get the following expressions for the shear stress expansion in ε

$$\begin{aligned} O(\varepsilon) &\rightarrow -\bar{\mu} \frac{\partial^2 \psi^{(0)}}{\partial {\xi_1}^2} \Bigg|_{\boldsymbol{x}=\boldsymbol{x_0}}, \\ O(\varepsilon^2) &\rightarrow -\bar{\mu} \frac{\partial^2 \psi^{(1)}}{\partial {\xi_1}^2} + \bar{\mu} \left(F_{11}^{-1} + 1 \right) ik_2 \frac{\partial \phi^{(0)}}{\partial X_1} \Bigg|_{\boldsymbol{x}=\boldsymbol{x_0}}, \\ O(\varepsilon^3) &\rightarrow -\bar{\mu} \frac{\partial^2 \psi^{(2)}}{\partial {\xi_1}^2} + \bar{\mu} \left(F_{11}^{-1} + 1 \right) ik_2 \frac{\partial \phi^{(1)}}{\partial X_1} - \bar{\mu} k_2^2 \psi^{(0)} \Bigg|_{\boldsymbol{x}=\boldsymbol{x_0}}. \end{aligned} \tag{7.71}$$

There is no shear stress term of order $O(1)$, which is expected.

7.4.3 Boundary conditions and potentials

In this section the potential functions that satisfy equations (7.51) in the domain of Figure 7.1 will be determined. The incident plane wave, which is defined by the angle θ, has the following potential function

$$\begin{aligned}\phi_i(x_1,x_2) &= A_0 \mathrm{e}^{ik(-x_1\sin(\theta)+x_2\cos(\theta))} \\ &= A_0 \mathrm{e}^{i(-k_1x_1+k_2x_2)}, \quad x_1>0, \;\; -\infty<x_2<\infty,\end{aligned} \tag{7.72}$$

where $k_1 = k\cos(\theta)$, $k_2 = k\sin(\theta)$, $k=\frac{\omega}{c_0}$, and $c_0=\sqrt{\frac{K_0}{\rho_0}}$. Similarly the reflected wave is defined by

$$\phi_s(x_1,x_2) = R\mathrm{e}^{i(k_1x_1+k_2x_2)}, \quad x_1>0, \;\; -\infty<x_2<\infty, \tag{7.73}$$

where R is a yet to be determined constant. Therefore the potential above the cloaked region is given as the sum of incident and reflected wave potentials.

$$\phi = \phi_i + \phi_s, \quad x_1>0. \tag{7.74}$$

The pressure distribution above the cloak is given by

$$\begin{aligned}p_i+p_s &= K_0\boldsymbol{\nabla}_x^2\left(\phi_i+\phi_s\right), \quad x_1>0, \\ &= -K_0k^2\left(\phi_i+\phi_s\right), \quad x_1>0.\end{aligned} \tag{7.75}$$

We are interested in determining the potential field inside the cloak. To do so let us assume that the potential functions in 2D Cartesian coordinates have the following form

$$\begin{aligned}\phi(X_1,X_2) &= \left(A_1\mathrm{e}^{i\gamma_1X_1}+A_2\mathrm{e}^{-i\gamma_1X_1}\right)\mathrm{e}^{ik_2X_2}, \quad 0<X_1<-a, \;\; -\infty<X_2<\infty, \\ \psi(\xi_1,\xi_2) &= \left(B_1\mathrm{e}^{i\beta_1\xi_1}+B_2\mathrm{e}^{-i\beta_1\xi_1}\right)\mathrm{e}^{ik_2\varepsilon\xi_2}, \quad 0<\varepsilon\xi_1<-b, \;\; -\infty<\varepsilon\xi_2<\infty.\end{aligned} \tag{7.76}$$

Therefore the variation of ψ with ξ_2, $\frac{\partial\psi}{\partial\xi_2}=i\varepsilon k_2\psi$, is of higher order ε than its variation with ξ_1. Consequently, the zeroth order equilibrium equations (7.51) have the form

$$\begin{aligned}K_0\nabla_X^2(\phi)+\rho_0\omega^2\phi &= \text{constant}, \\ \mu_0\frac{\partial^2\psi}{\partial{\xi_1}^2}+\rho_0\omega^2\psi &= \text{constant}.\end{aligned} \tag{7.77}$$

The wave numbers are determined by substituting expressions (7.76) back into equations (7.77), which gives

$$\begin{aligned} K_0(-\gamma_1^2 - k_2^2) + \rho_0\omega^2 = 0 \quad &\Longrightarrow \quad \gamma_1 = \sqrt{\frac{\rho_0\omega^2}{K_0} - k_2^2} \quad \Longrightarrow \quad \gamma_1 = k\cos(\theta) = k_1, \\ \mu_0(-\beta_1^2) + \rho_0\omega^2 = 0 \quad &\Longrightarrow \quad \beta_1 = \sqrt{\frac{\rho_0\omega^2}{\mu_0}} \quad \Longrightarrow \quad \beta_1 = k\sqrt{\frac{K_0}{\mu_0}}. \end{aligned} \tag{7.78}$$

From equations (7.73) and (7.75), wee see that this problem has five unknown constants: A_1, A_2, B_1, B_2, and R. Therefore we need at least five boundary conditions to solve for them. At $x_1, X_1 = 0$, the boundary conditions are

$$\begin{aligned} \sigma_{11}\Big|_{x_1=0} &= -(p_i + p_s)\Big|_{x_1=0}, \\ \sigma_{12}\Big|_{x_1=0} &= 0, \\ u_1\Big|_{x_1=0^-} &= u_1\Big|_{x_1=0^+}. \end{aligned} \tag{7.79}$$

The bottom surface of the slab at $x_1 = -b, X_1 = -a$ will be taken as rigid, this yields the following boundary conditions

$$\begin{aligned} u_1\Big|_{x_1=-b} &= 0, \\ u_2\Big|_{x_1=-b} &= 0. \end{aligned} \tag{7.80}$$

Lets take a closer look a the first boundary condition on σ_{11}. Expanding the right hand side in terms of ε yields

$$\sigma_{11} = -(p_i + p_s) + 0 \cdot \varepsilon + 0 \cdot \varepsilon^2 + ..., \tag{7.81}$$

where $p_i + p_s = -K_0 k^2 (\phi_i + \phi_s)$. Comparing equation (7.81) with equation (7.68) gives

the following boundary conditions

$$
\begin{aligned}
&K_0\left(\frac{b}{a}-1\right)ik_2\frac{\partial\psi^{(0)}}{\partial\xi_1}+K_0\left(\frac{\partial^2\phi^{(0)}}{\partial {X_1}^2}-k_2^2\phi^{(0)}\right)\Bigg|_{\xi_1=0,X_1=0}=-K_0k^2\left(\phi_i^{(0)}+\phi_s^{(0)}\right)\Big|_{x_1=0},\\
&K_0\left(\frac{b}{a}-1\right)ik_2\frac{\partial\psi^{(1)}}{\partial\xi_1}+K_0\left(\frac{\partial^2\phi^{(1)}}{\partial {X_1}^2}-k_2^2\phi^{(1)}\right)\Bigg|_{\xi_1=0,X_1=0}=-K_0k^2\phi_s^{(1)}\Big|_{x_1=0},\\
&K_0\left(\frac{b}{a}-1\right)ik_2\frac{\partial\psi^{(2)}}{\partial\xi_1}+K_0\left(\frac{\partial^2\phi^{(2)}}{\partial {X_1}^2}-k_2^2\phi^{(2)}\right)\\
&+2\bar{\mu}\left(ik_2\frac{\partial\psi^{(0)}}{\partial\xi_1}+F_{11}^{-1}\frac{\partial^2\phi^{(0)}}{\partial {X_1}^2}\right)\Bigg|_{\xi_1=0,X_1=0}=-K_0k^2\phi_s^{(2)}\Big|_{x_1=0},
\end{aligned}
\tag{7.82}
$$

where $x'=\frac{b}{a}$ has been used. Applying the same procedure to σ_{12} gives us

$$
\begin{aligned}
&-\bar{\mu}\frac{\partial^2\psi^{(0)}}{\partial {\xi_1}^2}\Big|_{\xi_1=0}=0,\\
&-\bar{\mu}\frac{\partial^2\psi^{(1)}}{\partial {\xi_1}^2}+\bar{\mu}\left(\frac{a}{b}+1\right)ik_2\frac{\partial\phi^{(0)}}{\partial X_1}\Big|_{\xi_1=0,X_1=0}=0,\\
&-\bar{\mu}\frac{\partial^2\psi^{(2)}}{\partial {\xi_1}^2}+\bar{\mu}\left(\frac{a}{b}+1\right)ik_2\frac{\partial\phi^{(1)}}{\partial X_1}-\bar{\mu}k_2^2\psi^{(0)}\Big|_{\xi_1=0,X_1=0}=0,
\end{aligned}
\tag{7.83}
$$

The three boundary conditions on the displacements must also be decomposed in orders of ε. The condition $u_1\Big|_{x_1=0^-}=u_1\Big|_{x_1=0^+}$ becomes

$$
\begin{aligned}
&\frac{\partial\phi^{(0)}}{\partial X_1}\Big|_{X_1=0}=\frac{\partial}{\partial x_1}\left(\phi_i^{(0)}+\phi_s^{(0)}\right)\Big|_{x_1=0},\\
&\frac{\partial\phi^{(1)}}{\partial X_1}+ik_2\psi^{(0)}\Big|_{\xi_1=0,X_1=0}=\frac{\partial\phi_s^{(1)}}{\partial x_1}\Big|_{x_1=0},\\
&\frac{\partial\phi^{(2)}}{\partial X_1}+ik_2\psi^{(1)}\Big|_{\xi_1=0,X_1=0}=\frac{\partial\phi_s^{(2)}}{\partial x_1}\Big|_{x_1=0},
\end{aligned}
\tag{7.84}
$$

The boundary condition $u_1\Big|_{\xi_1=-b/\varepsilon,X_1=-a}=0$ takes the form

$$
\begin{aligned}
&\frac{\partial\phi^{(0)}}{\partial X_1}\Big|_{X_1=-a}=0,\\
&\frac{\partial\phi^{(1)}}{\partial X_1}+ik_2\psi^{(0)}\Big|_{\xi_1=-b/\varepsilon,X_1=-a}=0,\\
&\frac{\partial\phi^{(2)}}{\partial X_1}+ik_2\psi^{(1)}\Big|_{\xi_1=-b/\varepsilon,X_1=-a}=0,
\end{aligned}
\tag{7.85}
$$

Lastly, the condition $u_2\Big|_{\xi_1=-b/\varepsilon,X_1=-a} = 0$

$$\begin{aligned}
ik_2\phi^{(0)} - \frac{\partial\psi^{(0)}}{\partial\xi_1}\Big|_{\xi_1=-b/\varepsilon,X_1=-a} &= 0,\\
ik_2\phi^{(1)} - \frac{\partial\psi^{(1)}}{\partial\xi_1}\Big|_{\xi_1=-b/\varepsilon,X_1=-a} &= 0,\\
ik_2\phi^{(2)} - \frac{\partial\psi^{(2)}}{\partial\xi_1}\Big|_{\xi_1=-b/\varepsilon,X_1=-a} &= 0,
\end{aligned} \tag{7.86}$$

7.4.4 Zeroth order solution in ε

Substituting equations (7.76) into equation (7.82), (7.83), (7.84), (7.85), and (7.86) yields the following five equations.

$$\begin{aligned}
-K_0\left(\frac{b}{a}-1\right)k_2\beta_1(B_1-B_2)\mathrm{e}^{i\varepsilon k_2\xi_2} - K_0\left(\gamma_1^2+k_2^2\right)(A_1+A_2)\mathrm{e}^{ik_2X_2} &= -K_0k^2\left(A_0+R\right)\mathrm{e}^{ik_2x_2},\\
\bar{\mu}\beta_1^2(B_1+B_2)\mathrm{e}^{ik_2\varepsilon\xi_2} &= 0,\\
i\gamma_1(A_1-A_2)\mathrm{e}^{ik_2X_2} &= ik_1(-A_0+R)\mathrm{e}^{ik_2x_2},\\
i\gamma_1(A_1\mathrm{e}^{-i\gamma_1a}-A_2\mathrm{e}^{i\gamma_1a})\mathrm{e}^{ik_2X_2} &= 0,\\
ik_2(A_1\mathrm{e}^{-i\gamma_1a}+A_2\mathrm{e}^{i\gamma_1a})\mathrm{e}^{ik_2X_2} - i\beta_1(B_1\mathrm{e}^{-i\beta_1\frac{b}{\varepsilon}}-B_2\mathrm{e}^{i\beta_1\frac{b}{\varepsilon}})\mathrm{e}^{ik_2\varepsilon\xi_2} &= 0,
\end{aligned} \tag{7.87}$$

However, from the deformation gradient (7.61) and definition (7.30) we see that

$$X_2 = x_2 = \varepsilon\xi_2, \tag{7.88}$$

which allows us to cancel the exponential terms in equations (7.87). Also note that $\gamma_1^2+k_2^2=k^2$ and $\gamma_1=k_1$. After some simplification, the resulting set of equations is

$$\begin{aligned}
-k^2(A_1+A_2) - \left(\frac{b}{a}-1\right)k_2\beta_1(B_1-B_2) + k^2R &= -k^2A_0,\\
B_1+B_2 &= 0,\\
A_1-A_2-R &= -A_0,\\
A_1\mathrm{e}^{-i\gamma_1a}-A_2\mathrm{e}^{i\gamma_1a} &= 0,\\
k_2(A_1\mathrm{e}^{-i\gamma_1a}+A_2\mathrm{e}^{i\gamma_1a}) - \beta_1(B_1\mathrm{e}^{-i\beta_1\frac{b}{\varepsilon}}-B_2\mathrm{e}^{i\beta_1\frac{b}{\varepsilon}}) &= 0,
\end{aligned} \tag{7.89}$$

Putting the above equations in matrix form yields

$$\begin{bmatrix} -k^2 & -k^2 & -\left(\frac{b}{a}-1\right)k_2\beta_1 & \left(\frac{b}{a}-1\right)k_2\beta_1 & k^2 \\ 0 & 0 & 1 & 1 & 0 \\ 1 & -1 & 0 & 0 & -1 \\ \mathrm{e}^{-i\gamma_1 a} & -\mathrm{e}^{i\gamma_1 a} & 0 & 0 & 0 \\ k_2\mathrm{e}^{-i\gamma_1 a} & k_2\mathrm{e}^{i\gamma_1 a} & -\beta_1\mathrm{e}^{-i\beta_1\frac{b}{\varepsilon}} & \beta_1\mathrm{e}^{i\beta_1\frac{b}{\varepsilon}} & 0 \end{bmatrix} \begin{bmatrix} A_1 \\ A_2 \\ B_1 \\ B_2 \\ R \end{bmatrix} = A_0 \begin{bmatrix} -k^2 \\ 0 \\ -1 \\ 0 \\ 0 \end{bmatrix}, \tag{7.90}$$

$$[D][a] = [b],$$

where the determinant of the matrix of coefficients is

$$\det[D] = 4\beta_1 \left(\cos(\beta_1 \frac{b}{\varepsilon})\mathrm{e}^{-ik_1 a} + \left(\frac{b}{a} - 1\right)\sin^2(\theta) \right). \tag{7.91}$$

We can see that the matrix of coefficients looses rank if the following equations are simultaneously satisfied

$$\begin{aligned} \cos\left(\beta_1 \frac{b}{\varepsilon}\right) + \left(\frac{b}{a} - 1\right)\sin^2(\theta)\cos(k_1 a) = 0, \\ \sin(k_1 a) = 0. \end{aligned} \tag{7.92}$$

From the second equation in (7.92) we have that $k_1 a = n\pi \quad \forall n = 0, 1, 2....$ Substituting this into the first equation in (7.92) gives

$$\varepsilon = \frac{\beta_1 b}{\arccos\left(\left(1 - \frac{b}{a}\right)\sin^2(\theta)\right) + 2\pi n} \quad \forall n = 0, 1, 2... \tag{7.93}$$

where we have only allowed positive values for ε. If, for example, $a = 2b = 1$ and the incident wave is at a 45 degree angle, then condition (7.93) becomes

$$\varepsilon = \beta_1 \left(\frac{1}{2}\arccos\left(\frac{1}{4}\right) + 2\pi n \right)^{-1} \approx \frac{\beta_1}{2.6362 + 2\pi n}, \tag{7.94}$$

Solving matrix equation (7.90) gives the coefficients as

$$\begin{aligned}
\frac{A_1}{A_0} &= \frac{\cos(\beta_1 \frac{b}{\varepsilon}) \mathrm{e}^{ik_1 2a}}{\cos(\beta_1 \frac{b}{\varepsilon}) + \left(\frac{b}{a} - 1\right) \sin^2(\theta) \mathrm{e}^{ik_1 a}}, \\
\frac{A_2}{A_0} &= \frac{\cos(\beta_1 \frac{b}{\varepsilon})}{\cos(\beta_1 \frac{b}{\varepsilon}) + \left(\frac{b}{a} - 1\right) \sin^2(\theta) \mathrm{e}^{ik_1 a}}, \\
\frac{B_1}{A_0} &= \frac{\sqrt{\frac{\mu_0}{K_0}} \sin(\theta) \mathrm{e}^{ik_1 a}}{\cos(\beta_1 \frac{b}{\varepsilon}) + \left(\frac{b}{a} - 1\right) \sin^2(\theta) \mathrm{e}^{ik_1 a}}, \\
\frac{B_2}{A_0} &= \frac{-\sqrt{\frac{\mu_0}{K_0}} \sin(\theta) \mathrm{e}^{ik_1 a}}{\cos(\beta_1 \frac{b}{\varepsilon}) + \left(\frac{b}{a} - 1\right) \sin^2(\theta) \mathrm{e}^{ik_1 a}}, \\
\frac{R}{A_0} &= \frac{\cos(\beta_1 \frac{b}{\varepsilon}) \mathrm{e}^{ik_1 2a} + \left(\frac{b}{a} - 1\right) \sin^2(\theta) \mathrm{e}^{ik_1 a}}{\cos(\beta_1 \frac{b}{\varepsilon}) + \left(\frac{b}{a} - 1\right) \sin^2(\theta) \mathrm{e}^{ik_1 a}}.
\end{aligned} \tag{7.95}$$

Note that the denominator of the coefficients is the determinant of the coefficient matrix and therefore has singular values.

In order to check the validity of equations (7.95) we need to show that the coefficients approach the shear-free solution as ε tends to zero. If no shear is present, we only need to solve for the constants A_1, A_2, and R so that the second and fifth boundary conditions will not be used. The resulting matrix equation is

$$\begin{bmatrix} -1 & -1 & 1 \\ 1 & -1 & -1 \\ \mathrm{e}^{-i\gamma_1 a} & -\mathrm{e}^{i\gamma_1 a} & 0 \end{bmatrix} \begin{bmatrix} A_1 \\ A_2 \\ R \end{bmatrix} = A_0 \begin{bmatrix} -1 \\ -1 \\ 0 \end{bmatrix}. \tag{7.96}$$

The shear-free solution becomes

$$\begin{aligned}
\frac{A_1}{A_0} &= \mathrm{e}^{i\gamma_1 2a}, \\
\frac{A_2}{A_0} &= 1, \\
\frac{R}{A_0} &= \mathrm{e}^{i\gamma_1 2a}.
\end{aligned} \tag{7.97}$$

7.4.5 First order solution in ε

The first order equilibrium equation has the form

$$\begin{aligned} x_1 \quad &\rightarrow \quad \frac{\partial}{\partial X_1}\left(\nabla_X^2(\phi^{(1)}) + \rho_0\omega^2\phi^{(1)}\right) + ik_2\left(\mu_0\frac{\partial^2\psi^{(0)}}{\partial {\xi_1}^2} + \rho_0\omega^2\psi^{(0)}\right) = 0, \\ x_2 \quad &\rightarrow \quad \frac{\partial}{\partial X_2}\left(\nabla_X^2(\phi^{(1)}) + \rho_0\omega^2\phi^{(1)}\right) - \frac{\partial}{\partial \xi_1}\left(\mu_0\frac{\partial^2\psi^{(1)}}{\partial {\xi_1}^2} + \rho_0\omega^2\psi^{(1)}\right) \\ &\qquad\qquad - F_{11}^{-1}\frac{\partial\bar{\mu}}{\partial X_1}\rho_0\rho^{-1}\frac{\partial^2\psi^{(}0)}{\partial {\xi_1}^2} = 0. \end{aligned} \tag{7.98}$$

Note that the shear term in the x_1 equation is already satisfied by the zeroth order solution. Therefore the equations for $\phi^{(1)}$ and $\psi^{(1)}$ are

$$\begin{aligned} &K_0\nabla_X^2(\phi^{(1)}) + \rho_0\omega^2\phi^{(1)} = 0, \\ &\frac{\partial}{\partial\xi_1}\left(\mu_0\frac{\partial^2\psi^{(1)}}{\partial {\xi_1}^2} + \rho_0\omega^2\psi^{(1)}\right) = -\frac{\partial}{\partial\xi_1}\left(F_{11}^{-1}\frac{\partial\bar{\mu}}{\partial X_1}\rho_0\rho^{-1}\frac{\partial\psi^{(0)}}{\partial\xi_1}\right). \end{aligned} \tag{7.99}$$

The solution for $\phi^{(1)}$ is

$$\phi^{(1)}(X_1, X_2) = \left(A_1^{(1)}\mathrm{e}^{i\gamma_1 X_1} + A_2^{(1)}\mathrm{e}^{-i\gamma_1 X_1}\right)\mathrm{e}^{ik_2X_2}, \quad \gamma_1 = k_1. \tag{7.100}$$

As we have done before, the following dependence on ξ_2 will be assumed, $\psi^{(i)} = \bar{\psi}^{(i)}(\xi_1)\mathrm{e}^{i\varepsilon k_2\xi_2}$. This allows us to rewrite the equilibrium equation for $\psi^{(1)}$ as

$$\frac{d^2\bar{\psi}^{(1)}}{d{\xi_1}^2} + \beta_1^2\bar{\psi}^{(1)} = -\left(\frac{a}{b}\frac{1}{\bar{\mu}}\frac{\partial\bar{\mu}}{\partial X_1}\right)i\beta_1\left(B_1^{(0)}\mathrm{e}^{i\beta_1\xi_1} - B_2^{(0)}\mathrm{e}^{-i\beta_1\xi_1}\right) + \text{constant}, \tag{7.101}$$

where $\beta_1 = \sqrt{\frac{\rho_0\omega^2}{\mu_0}}$, $\mu_0 = \rho^{-1}\rho_0\bar{\mu}$, $F_{11}^{-1} = \frac{a}{b}$, and $\psi^{(0)}$ is given by equation (7.76). Taking the constant as zero, the solution for $\psi^{(1)}$ is the sum of the homogeneous and particular solutions as

$$\begin{aligned} \psi^{(1)}(\xi_1, \xi_2) = &\left(B_1^{(1)}\mathrm{e}^{i\beta_1\xi_1} + B_2^{(1)}\mathrm{e}^{-i\beta_1\xi_1}\right)\mathrm{e}^{i\varepsilon k_2\xi_2} \\ &+ q(X_1)\left(D_1(\xi_1)\mathrm{e}^{i\beta_1\xi_1} + D_2(\xi_1)\mathrm{e}^{-i\beta_1\xi_1}\right)\mathrm{e}^{i\varepsilon k_2\xi_2}. \end{aligned} \tag{7.102}$$

with

$$\begin{aligned} q(X_1) =& \frac{1}{4i\beta_1}\frac{a}{b}\frac{1}{\bar{\mu}}\frac{\partial\bar{\mu}}{\partial X_1}, \\ D_1(\xi_1) =& \left(B_1^{(0)} - B_2^{(0)} - 2i\beta_1 B_1^{(0)}\xi_1\right), \\ D_2(\xi_1) =& \left(B_1^{(0)} - B_2^{(0)} - 2i\beta_1 B_2^{(0)}\xi_1\right). \end{aligned} \tag{7.103}$$

Let us also expand the reflection coefficient in powers of ε as

$$R = R^{(0)} + \varepsilon R^{(1)} + \varepsilon^2 R^{(2)} + ... \tag{7.104}$$

which gives the reflected wave of order ε as

$$\phi_s^{(1)}(x_1, x_2) = R^{(1)} \mathrm{e}^{i(k_1 x_1 + k_2 x_2)}, \quad x_1 > 0, \ \ -\infty < x_2 < \infty, \tag{7.105}$$

Once again, the problem is to determine the five constant coefficients, which are: $A_1^{(1)}$, $A_2^{(1)}$, $B_1^{(1)}$, $B_2^{(1)}$, and $R^{(1)}$. The five boundary conditions on the solution of order ε are

$$\begin{aligned}
K_0 \left(\frac{b}{a} - 1\right) ik_2 \frac{\partial \psi^{(1)}}{\partial \xi_1} + K_0 \left(\frac{\partial^2 \phi^{(1)}}{\partial {X_1}^2} - k_2^2 \phi^{(1)}\right)\Bigg|_{\xi_1=0, X_1=0} &= -K_0 k^2 \phi_s^{(1)}\Big|_{x_1=0}, \\
-\bar{\mu} \frac{\partial^2 \psi^{(1)}}{\partial {\xi_1}^2} + \bar{\mu} \left(\frac{a}{b} + 1\right) ik_2 \frac{\partial \phi^{(0)}}{\partial X_1}\Bigg|_{\xi_1=0, X_1=0} &= 0, \\
\frac{\partial \phi^{(1)}}{\partial X_1} + ik_2 \psi^{(0)}\Big|_{\xi_1=0, X_1=0} &= \frac{\partial \phi_s^{(1)}}{\partial x_1}\Big|_{x_1=0}, \\
\frac{\partial \phi^{(1)}}{\partial X_1} + ik_2 \psi^{(0)}\Big|_{\xi_1=-b/\varepsilon, X_1=-a} &= 0, \\
ik_2 \phi^{(1)} - \frac{\partial \psi^{(1)}}{\partial \xi_1}\Big|_{\xi_1=-b/\varepsilon, X_1=-a} &= 0,
\end{aligned} \tag{7.106}$$

Substituting equations (7.76), (7.100), (7.102), (7.105) into above and simplifying yields

$$\begin{aligned}
\left(\frac{b}{a} - 1\right) ik_2 \left(i\beta_1 \left(B_1^{(1)} + B_2^{(1)}\right) - 2q(0) i\beta_1 \left(B_1^{(0)} + B_2^{(0)}\right)\right) & \\
-k^2 \left(A_1^{(1)} + A_2^{(1)}\right) &= -k^2 R^{(1)}, \\
\beta_1^2 \left(B_1^{(1)} + B_2^{(1)}\right) + 2q(0)\beta_1^2 \left(-B_1^{(0)} + B_2^{(0)}\right) - \left(\frac{a}{b} + 1\right) k_1 k_2 \left(A_1^{(0)} - A_2^{(0)}\right) &= 0, \\
ik_1 \left(A_1^{(1)} - A_2^{(1)}\right) + ik_2 \left(B_1^{(0)} + B_2^{(0)}\right) &= ik_1 R^{(1)}, \\
ik_1 \left(A_1^{(1)} \mathrm{e}^{-ik_1 a} - A_2^{(1)} \mathrm{e}^{ik_1 a}\right) + ik_2 \left(B_1^{(0)} \mathrm{e}^{-i\beta_1 \frac{b}{\varepsilon}} + B_2^{(0)} \mathrm{e}^{i\beta_1 \frac{b}{\varepsilon}}\right) &= 0, \\
ik_2 \left(A_1^{(1)} \mathrm{e}^{-ik_1 a} + A_2^{(1)} \mathrm{e}^{ik_1 a}\right) - i\beta_1 \left(B_1^{(1)} \mathrm{e}^{-i\beta_1 \frac{b}{\varepsilon}} - B_2^{(1)} \mathrm{e}^{i\beta_1 \frac{b}{\varepsilon}}\right) & \\
-q(-a) i\beta_1 \Big[\left(-B_1^{(0)} - B_2^{(0)} + 2i\beta_1 B_1^{(0)} \frac{b}{\varepsilon}\right) \mathrm{e}^{-i\beta_1 \frac{b}{\varepsilon}} & \\
+ \left(-B_1^{(0)} - B_2^{(0)} - 2i\beta_1 B_2^{(0)} \frac{b}{\varepsilon}\right) \mathrm{e}^{i\beta_1 \frac{b}{\varepsilon}} \Big] &= 0,
\end{aligned} \tag{7.107}$$

Rearranging the above equations yields

$$\begin{aligned}
-k^2 A_1^{(1)} - k^2 A_2^{(1)} - \left(\frac{b}{a} - 1\right)\beta_1 k_2 B_1^{(1)} - \left(\frac{b}{a} - 1\right)\beta_1 k_2 B_2^{(1)} + k^2 R^{(1)} = \\
-2\left(\frac{b}{a} - 1\right) q(0)\beta_1 k_2 \left(B_1^{(0)} + B_2^{(0)}\right), \\
\beta_1^2 B_1^{(1)} + \beta_1^2 B_2^{(1)} = \\
\left(\frac{a}{b} + 1\right) k_1 k_2 \left(A_1^{(0)} - A_2^{(0)}\right) + 2q(0)\beta_1^2 \left(B_1^{(0)} - B_2^{(0)}\right), \\
k_1 A_1^{(1)} - k_1 A_2^{(1)} - k_1 R^{(1)} = \\
-k_2 \left(B_1^{(0)} + B_2^{(0)}\right), \\
k_1 \mathrm{e}^{-ik_1 a} A_1^{(1)} - k_1 \mathrm{e}^{ik_1 a} A_2^{(1)} = \\
-k_2 \left(B_1^{(0)} \mathrm{e}^{-i\beta_1 \frac{b}{\varepsilon}} + B_2^{(0)} \mathrm{e}^{i\beta_1 \frac{b}{\varepsilon}}\right), \\
k_2 \mathrm{e}^{-ik_1 a} A_1^{(1)} + k_2 \mathrm{e}^{ik_1 a} A_2^{(1)} - \beta_1 \mathrm{e}^{-i\beta_1 \frac{b}{\varepsilon}} B_1^{(1)} + \beta_1 \mathrm{e}^{i\beta_1 \frac{b}{\varepsilon}} B_2^{(1)} = \\
q(-a)\beta_1 \left[\left(-B_1^{(0)} - B_2^{(0)} + 2i\beta_1 B_1^{(0)} \frac{b}{\varepsilon}\right) \mathrm{e}^{-i\beta_1 \frac{b}{\varepsilon}} + \left(-B_1^{(0)} - B_2^{(0)} - 2i\beta_1 B_2^{(0)} \frac{b}{\varepsilon}\right) \mathrm{e}^{i\beta_1 \frac{b}{\varepsilon}}\right],
\end{aligned} \tag{7.108}$$

Putting equation (7.108) in matrix form yields

$$\begin{bmatrix}
-k^2 & -k^2 & -\left(\frac{b}{a} - 1\right) k_2 \beta_1 & \left(\frac{b}{a} - 1\right) k_2 \beta_1 & k^2 \\
0 & 0 & \beta_1^2 & \beta_1^2 & 0 \\
k_1 & -k_1 & 0 & 0 & -k_1 \\
k_1 \mathrm{e}^{-ik_1 a} & -k_1 \mathrm{e}^{ik_1 a} & 0 & 0 & 0 \\
k_2 \mathrm{e}^{-i\gamma_1 a} & k_2 \mathrm{e}^{i\gamma_1 a} & -\beta_1 \mathrm{e}^{-i\beta_1 \frac{b}{\varepsilon}} & \beta_1 \mathrm{e}^{i\beta_1 \frac{b}{\varepsilon}} & 0
\end{bmatrix}
\begin{bmatrix} A_1^{(1)} \\ A_2^{(1)} \\ B_1^{(1)} \\ B_2^{(1)} \\ R^{(1)} \end{bmatrix} =$$

$$\begin{bmatrix}
0 & 0 & -2\left(\frac{b}{a} - 1\right) q(0) k_2 \beta_1 & -2\left(\frac{b}{a} - 1\right) q(0) k_2 \beta_1 & 0 \\
\left(\frac{a}{b} + 1\right) k_1 k_2 & -\left(\frac{a}{b} + 1\right) k_1 k_2 & 2q(0)\beta_1^2 & -2q(0)\beta_1^2 & 0 \\
0 & 0 & -k_2 & -k_2 & 0 \\
0 & 0 & -k_2 \mathrm{e}^{-i\beta_1 \frac{b}{\varepsilon}} & -k_2 \mathrm{e}^{i\beta_1 \frac{b}{\varepsilon}} & 0 \\
0 & 0 & q(-a)\beta_1 \eta_1 & q(-a)\beta_1 \eta_2 & 0
\end{bmatrix}
\begin{bmatrix} A_1^{(0)} \\ A_2^{(0)} \\ B_1^{(0)} \\ B_2^{(0)} \\ R^{(0)} \end{bmatrix}, \tag{7.109}$$

where $\eta_1 = \left(-1 + 2i\beta_1 \frac{b}{\varepsilon}\right) \mathrm{e}^{-i\beta_1 \frac{b}{\varepsilon}} - \mathrm{e}^{i\beta_1 \frac{b}{\varepsilon}}$, $\eta_2 = -\mathrm{e}^{-i\beta_1 \frac{b}{\varepsilon}} - \left(1 + 2i\beta_1 \frac{b}{\varepsilon}\right) \mathrm{e}^{i\beta_1 \frac{b}{\varepsilon}}$, $q(0) = \frac{1}{4i\beta_1} \frac{a}{b} \left(\frac{1}{\bar{\mu}} \frac{\partial \bar{\mu}}{\partial X_1}\right)\Big|_{X_1=0}$, and $q(-a) = \frac{1}{4i\beta_1} \frac{a}{b} \left(\frac{1}{\bar{\mu}} \frac{\partial \bar{\mu}}{\partial X_1}\right)\Big|_{X_1=-a}$. If the shear modulus does not vary with X_1, matrices (7.109) simplify to

$$\begin{bmatrix} -k^2 & -k^2 & -\left(\frac{b}{a}-1\right)k_2\beta_1 & \left(\frac{b}{a}-1\right)k_2\beta_1 & k^2 \\ 0 & 0 & \beta_1^2 & \beta_1^2 & 0 \\ k_1 & -k_1 & 0 & 0 & -k_1 \\ k_1\mathrm{e}^{-ik_1a} & -k_1\mathrm{e}^{ik_1a} & 0 & 0 & 0 \\ k_2\mathrm{e}^{-i\gamma_1 a} & k_2\mathrm{e}^{i\gamma_1 a} & -\beta_1\mathrm{e}^{-i\beta_1\frac{b}{\varepsilon}} & \beta_1\mathrm{e}^{i\beta_1\frac{b}{\varepsilon}} & 0 \end{bmatrix} \begin{bmatrix} A_1^{(1)} \\ A_2^{(1)} \\ B_1^{(1)} \\ B_2^{(1)} \\ R^{(1)} \end{bmatrix} = \\ \begin{bmatrix} 0 & 0 & 0 & 0 & 0 \\ \left(\frac{a}{b}+1\right)k_1k_2 & -\left(\frac{a}{b}+1\right)k_1k_2 & 0 & 0 & 0 \\ 0 & 0 & -k_2 & -k_2 & 0 \\ 0 & 0 & -k_2\mathrm{e}^{-i\beta_1\frac{b}{\varepsilon}} & -k_2\mathrm{e}^{i\beta_1\frac{b}{\varepsilon}} & 0 \\ 0 & 0 & 0 & 0 & 0 \end{bmatrix} \begin{bmatrix} A_1^{(0)} \\ A_2^{(0)} \\ B_1^{(0)} \\ B_2^{(0)} \\ R^{(0)} \end{bmatrix}, \tag{7.110}$$

7.5 Discussion of the results

As an example, consider a slab of thickness $b/a = 0.5$. The background fluid is water with density $\rho_0 = 1000$ kg/m^3 and bulk modulus $K_0 = 2.25$ GPa. A plane wave is incident onto the slab at an angle $\theta = 45°$. Figure 7.2 shows the amplitude and phase of the complex valued reflection coefficient $R^{(0)}$ as a function of ε.

The amplitude of the reflection coefficient is $|R^{(0)}| = 1$, which is consistent with scattering from a rigid surface. However, the added shear affects the phase of the reflected wave. Furthermore, this phase frequently oscillates because of the slow shear wave contribution via terms such as $\mathrm{e}^{i\beta_1 b/\epsilon}$ in equation (7.90).

The first order contribution to the reflection coefficient $\varepsilon R^{(1)}$ is shown in Figure 7.3 as a function of increasing shear modulus ε. At first glance, the magnitude $|R^{(1)}| > 0$ seems to violate energy conservation. However, this is only the second term in the expansion $R = R^{(0)} + \varepsilon R^{(1)} + \ldots$ and thus the second order term $|R^{(2)}| < 0$ of same order. By this argument, we conclude that the reflection coefficient is

$$R = 1 + O(\varepsilon^2). \tag{7.111}$$

The phase of $R^{(1)}$ oscillates rapidly. This suggests that such a PM surface cloak will not perform as designed because the incident and scattered waves will not be in phase.

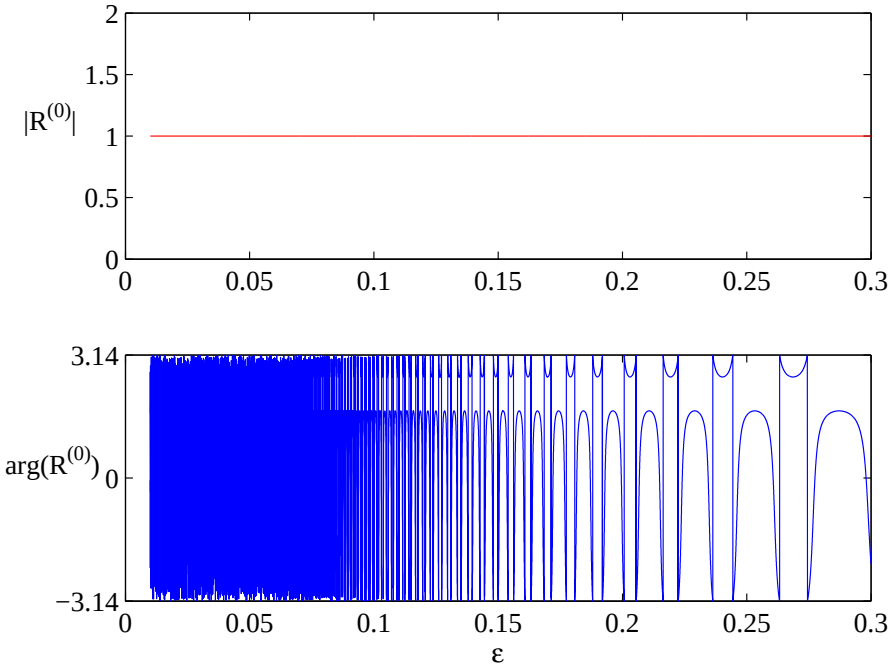

Figure 7.2: The zeroth order reflection coefficient $R^{(0)}$ as a function of increasing shear modulus.

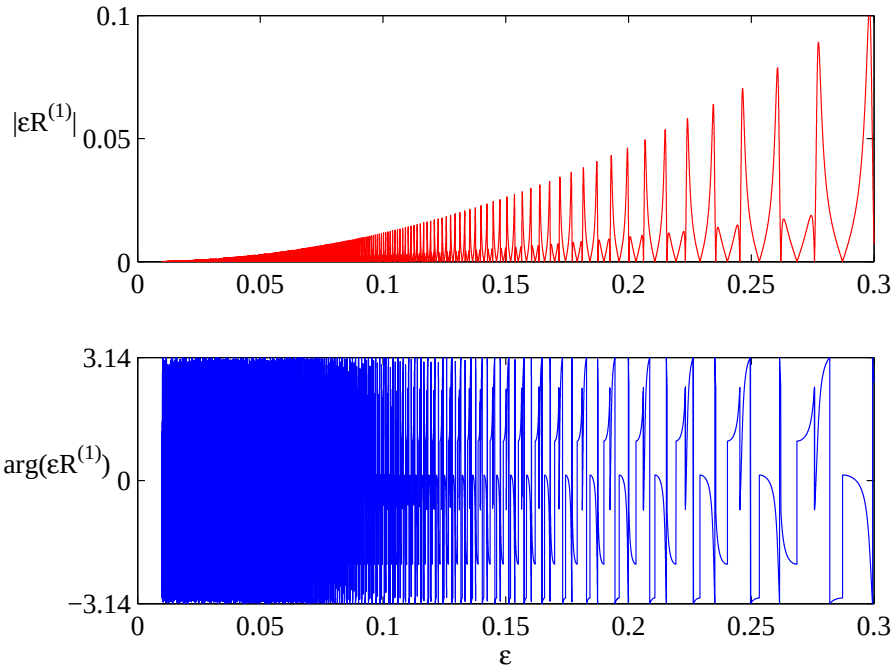

Figure 7.3: The first order reflection coefficient $R^{(1)}$ as a function of increasing shear modulus.

Chapter 8

Conclusions

8.1 Summary of accomplishments

This Dissertation presents the following developments

1. Acoustically transparent elastic shells at quasi-static frequencies,
2. A closed form solution to an elastic shell loaded by an axisymmetric distribution of internal springs,
3. A high transmission acoustic lens based on a varying index of refraction,
4. An analytical expression for the width of the flexural resonance of an elastic shell,
5. An analytical expression for split of the flexural resonance of due to two nearby elastic shells,
6. The novel acoustic Poisson-like effect.

It has been shown that an elastic shell can be tuned through its geometric and constitutive parameters to exhibit prescribed effective acoustic properties. Another method for acoustically tuning shells is with an internal substructure. A closed form solution has been developed for scattering from an elastic shell with an internal axisymmetric distribution of point spring forces coupled by a central mass. The solution is unique in that it separates into as many sub-solutions as there are loading points. Furthermore, the subsonic flexural waves excited in the shell by the attachment of stiffeners are suppressed by including a sufficiently large number of such stiffeners. One application of this is an acoustically transparent shell with the possibility of housing an internal

payload. Another application is refraction-based wave steering as demonstrated by the cylindrical-to-plane wave lens. Two different designs of this lens are outlined.

The second half of the Dissertation investigates the interaction of flexural-borne waves on nearby shells. An asymptotic expression for the width of the flexural resonance of a thin shell is derived from first principle. This is then used with the theory of multiple scattering to derive an analytical expression for the shift of this frequency when two shells are nearby. This shift is remarkably accurate when compared with finite element simulations. Postulating coherent scattering of waves from the lowest flexural resonance in an array leads to the discovery of the acoustic Poisson-like effect. This effect redirects an incident acoustic wave by 90° in an otherwise acoustically transparent sonic crystal. An unresponsive "deaf" antisymmetric mode locked to band gap boundaries is unlocked by matching Bragg scattering with a quadrupole flexural resonance of the shell. The dynamic effect causes normal unidirectional wave motion to strongly couple to perpendicular motion, analogous to the quasi-static Poisson effect in solids. The Poisson-like effect is demonstrated using the first flexural resonance of an acrylic shell. This represent a new type of material which cannot be accurately described as an effective acoustic medium. The study concludes with an analysis of a non-zero shear modulus in a pentamode cloak via the two-scale method with the shear modulus as the perturbation parameter.

8.2 Testing and future work

Preliminary experiments confirm the decrease in scattering from an aluminum shell with an acrylic insert in water as compared to the empty shell. Figure 8.1a shows the acrylic with a steel central rod which was manufactured with rapid prototyping as a proof of concept. The shell that was tested contains a machined acrylic rod as shown in Figure 8.1b. During the initial testing phase it was discovered that a low-viscosity adhesive has to be used to bond the shell to the insert so that there is no rattling. However, because tuned shells have to be tested at low frequencies the goal of future experiments would be to minimize noise.

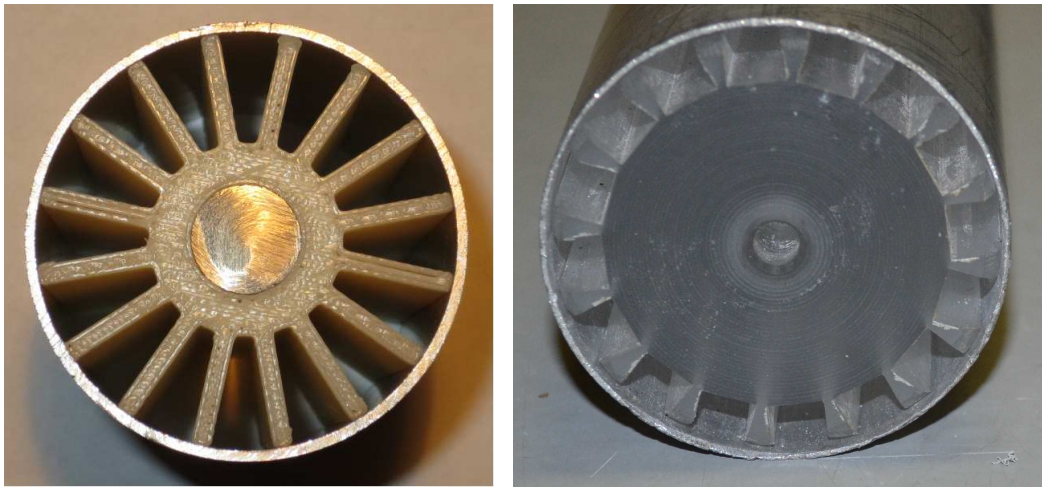

(a) (b)

Figure 8.1: Acoustically transparent aluminum shells from different manufacturing methods. Plot (a) shows the ABS substructure via rapid prototyping with an inserted steel rod. Plot (b) shows the substructure machined from an acrylic rod (courtesy Michael Haberman of UT Austin).

The cylindrical-to-plane wave lens of empty elastic shells is also currently being constructed at The University of Texas at Austin ARL. A source which can perform well at the operating frequency of 22 kHz is far too large to fit in the designed lens. As a result, the positions of source and hydrophone will be switched, which should yield the same results via reciprocity. Those results will be presented in forthcoming paper.

Much work could be done on extending the design possibilities of the metamaterials described herein. The possibility of azimuthally varying the stiffness of the internally tuned shell is particularly interesting. An array of such shells would theoretically behave as an anisotropic fluid. The utility of the resonance of the internal substructure deserves considerable attention as well.

The acoustic Poisson-like effect could also be extended to include other wave media such as phononic crystals and plates. The effect is based on the natural cohesion of a quadruple resonance in a square array. The intriguing question is whether a hexapole local resonance in a hexagonal array would yield similarly exciting results. Furthermore, a particular local resonance can be introduced through the design of an internal substructure to be placed in the shells.

On a different note, non-linear acoustic lenses have been shown to produce sonic bullets [98]. The non-linearity is a consequence of wave propagation through rows of spheres in contact. The simulation of the contact could be simplified by such numerical techniques as described in Ref. [100]. There, a compact form for the Green's function for symmetric loading of an elastic sphere is derived. As an extension, the contact of spherical elastic shells could also yield unique results.

Appendix A

3DOF model of a finite sized internal mass

One spring

We use Lagrange's equations for the Lagrangian $L = L(x, y, \phi, \dot{x}, \dot{y}, \dot{\phi}) \equiv T - V$, where $T = \frac{1}{2}m(\dot{x}^2 + \dot{y}^2) + \frac{1}{2}I\dot{\phi}^2$ is the kinetic energy, and assuming that the spring is linear, $V = \frac{\kappa}{2}(l - l_0)^2$, where l, l_0 are the stretched and un-stretched lengths of the spring. For a spring oriented at angle θ_1 with respect to the positive x-axis (refer to Figure 3.3), the spring length is given by

$$l^2 = \big|a(\cos\theta_1, \sin\theta_1) + (w\cos\theta_1 - v\sin\theta_1, w\sin\theta_1 + v\cos\theta_1) \\ - (x, y) - b(\cos(\theta_1 + \phi), \sin(\theta_1 + \phi))\big|^2. \tag{A.1}$$

The Euler-Lagrange equation for x, $\frac{\partial L}{\partial x} - \frac{d}{dt}\frac{\partial L}{\partial \dot{x}} = 0$, is fully nonlinear and can be cast in the following form

$$m\ddot{x} = -\kappa(l - l_0)\frac{\partial l}{\partial x} \quad \Rightarrow \quad m\ddot{x} = -\kappa\frac{(l^2 - l_0^2)}{2l(l + l_0)}\frac{\partial l^2}{\partial x}, \tag{A.2}$$

where $\partial l^2/\partial x$ follows from (A.1). Similar equations for $\ddot{y}$ and $\ddot{\phi}$ can be found from the respective Euler-Lagrange equations.

Linearization

Equations for $\ddot{x}$, $\ddot{y}$ and $\ddot{\phi}$ such as equation (A.2) form a set of coupled nonlinear ordinary differential equations. In order to get the linear equations we need only the terms linear in x, y, ϕ and w, v, or equivalently, linear in $l^2 - l_0^2$. Hence,

$$m\ddot{x} \approx \frac{-\kappa}{4l_0^2}\left.\frac{\partial l^2}{\partial x}\right|_0 (l^2 - l_0^2), \quad m\ddot{y} \approx \frac{-\kappa}{4l_0^2}\left.\frac{\partial l^2}{\partial y}\right|_0 (l^2 - l_0^2), \quad I\ddot{\phi} \approx \frac{-\kappa}{4l_0^2}\left.\frac{\partial l^2}{\partial \phi}\right|_0 (l^2 - l_0^2), \tag{A.3}$$

where $|_0$ indicates the unstretched value ($x = y = \phi = 0, w = v = 0$). Equation (A.1) implies

$$l_0 = a - b, \quad \left.\frac{\partial l^2}{\partial x}\right|_0 = -2l_0 \cos\theta_1, \quad \left.\frac{\partial l^2}{\partial y}\right|_0 = -2l_0 \sin\theta_1, \quad \left.\frac{\partial l^2}{\partial \phi}\right|_0 = 0 \tag{A.4}$$

and

$$\begin{aligned} l^2 - l_0^2 &\approx \left.\frac{\partial l^2}{\partial x}\right|_0 x + \left.\frac{\partial l^2}{\partial y}\right|_0 y + \left.\frac{\partial l^2}{\partial \phi}\right|_0 \phi + \left.\frac{\partial l^2}{\partial w}\right|_0 w + \left.\frac{\partial l^2}{\partial v}\right|_0 v \\ &= -2l_0(x\cos\theta_1 + y\sin\theta_1) + 2l_0 w. \end{aligned}$$

The linearized equations are therefore

$$\begin{aligned} m\big(\ddot{x},\, \ddot{y}\big) &= -\kappa(x\cos\theta_1 + y\sin\theta_1 - w)\,\big(\cos\theta_1,\, \sin\theta_1\big), \\ I\ddot{\phi} &= 0. \end{aligned} \tag{A.5}$$

The contribution of the rotation angle ϕ of the internal mass to the spring force is nonlinear and does not appear in this linear formulation. As an aside, this will be demostrated by determining the equation of rotational motion of the mass $I\ddot{\phi} = r \times F$ with all other displacements constrained: $x = 0$, $y = 0$, $v = 0$ and $w = 0$. For small displacements $\phi \ll 1$, the vector r, which defines the position of the force vector $F = \kappa\frac{|l|-|l_0|}{|l|}l$, is $r = (b, b\phi)$. The deformed spring length vector is $l = (a - b, -b\phi)$ yielding a spring extension of $|l| - |l_0| = (a-b)\sqrt{1 + b^2\phi^2/(a-b)^2} - (a-b)$. Using the binomial theorem for the square root, we get $(|l| - |l_0|)/|l| \approx \frac{1}{2}b^2\phi^2/(a-b)^2$. Lastly, the cross product is $r \times l = -ab\phi$ giving a moment on the mass $r \times F = -\frac{1}{2}\kappa a(b\phi)^3/(a-b)^2$. This demonstrates that due to the geometry of this problem, the contribution of the rotation angle ϕ to the spring force is proportional to ϕ^2 and the contribution to the moment is proportional to ϕ^3. Thus, in the linearized equations (A.5), we obtain $\phi = 0$.

J springs

The equations of motion in the presence of J springs are

$$\begin{aligned} m\big(\ddot{x},\, \ddot{y}\big) &= -\kappa\sum_{j=1}^{J}(x\cos\theta_j + y\sin\theta_j - w(\theta_j))\,\big(\cos\theta_j,\, \sin\theta_j\big), \\ I\ddot{\phi} &= 0. \end{aligned} \tag{A.6}$$

Again, $\phi = 0$. For time harmonic motion ($x \to x\mathrm{e}^{-i\omega t}, \ldots$) the equations for x and y follow from (A.6) as

$$\begin{pmatrix} 2\tau^2 - J - C & -S \\ -S & 2\tau^2 - J + C \end{pmatrix} \begin{pmatrix} x \\ y \end{pmatrix} = -2 \sum_{j=1}^{J} w(\theta_j) \begin{pmatrix} \cos\theta_j \\ \sin\theta_j \end{pmatrix}, \tag{A.7}$$

where (see (3.28)) $\tau^2 = \frac{m\omega^2}{\kappa}$ and

$$C + iS = \sum_{j=1}^{J} \mathrm{e}^{i2\theta_j}. \tag{A.8}$$

Solving for x and y,

$$\begin{pmatrix} x \\ y \end{pmatrix} = \frac{-2}{(2\tau^2 - J)^2 - C^2 - S^2} \sum_{j=1}^{J} w(\theta_j) \begin{pmatrix} 2\tau^2 - J + C & S \\ S & 2\tau^2 - J - C \end{pmatrix} \begin{pmatrix} \cos\theta_j \\ \sin\theta_j \end{pmatrix}. \tag{A.9}$$

For $J > 1$ we assume that the angles $\{\theta_j\}$ are uniformly distributed, i.e. $\theta_{j+1} = \theta_j + 2\pi/J$. Hence $C + iS = 0$ for all values of J except $J = 1, 2$, in which cases $C + iS = J\mathrm{e}^{i2\theta_1}$. Solving (A.9) for the displacements then yields

$$\begin{pmatrix} x \\ y \end{pmatrix} = \frac{-1}{\tau^2 - H_J} \sum_{j=1}^{J} w(\theta_j) \begin{pmatrix} \cos\theta_j \\ \sin\theta_j \end{pmatrix}, \quad H_J = \begin{cases} J, & J = 1, 2, \\ \frac{J}{2}, & J \geq 3. \end{cases} \tag{A.10}$$

Radial force

The radial component of the force per unit area on the shell is

$$f(\theta) = \frac{\kappa}{a} \sum_{j=1}^{J} (x\cos\theta_j + y\sin\theta_j - w(\theta_j))\delta(\theta - \theta_j), \tag{A.11}$$

where $\delta(\theta)$ is the Dirac delta function. The azimuthal component of the force is negligible. Substituting (A.10) into (A.11) yields

$$f(\theta) = -\frac{\kappa}{a}\Big(\frac{1}{\tau^2 - H_J}\Big) \sum_{j=1}^{J} \Big[\sum_{m=1}^{J} w(\theta_m)\cos(\theta_j - \theta_m) + \Big(\tau^2 - H_J\Big) w(\theta_j) \Big] \delta(\theta - \theta_j), \tag{A.12}$$

where H_J is defined in (A.10). The specific form of the radial force per unit length on the shell due to a single spring, a diametrical pair of springs, and for $J \geq 3$ uniformly distributed springs are given in equation (3.27).

Net force

Expanding the radial force in equation (A.12) in azimuthal modes (see (3.29)) for a single spring ($J = 1$) at angle θ_1 yields the modal force

$$f_n = -\frac{\kappa}{2\pi a}\left(\frac{\tau^2}{\tau^2 - 1}\right) w(\theta_1)\mathrm{e}^{-in\theta_1}. \tag{A.13}$$

Similarly, for $J = 2$ springs oriented at θ_1 and $\theta_2 = \theta_1 + \pi$ the modal force has the form

$$f_n = -\frac{\kappa}{2\pi a}\sum_{j=1}^{2} w(\theta_j)\mathrm{e}^{-in\theta_j} \times \begin{cases} \frac{\tau^2}{\tau^2-2} & \text{for odd } n, \\ 1 & \text{for even } n, \end{cases} \tag{A.14a}$$

$$= -\frac{\kappa}{2\pi a}\mathrm{e}^{-in\theta_1} \times \begin{cases} \frac{\tau^2}{\tau^2-2}\left(w(\theta_1) - w(\theta_1+\pi)\right) & \text{for odd } n, \\ w(\theta_1) + w(\theta_1+\pi) & \text{for even } n, \end{cases} \tag{A.14b}$$

Now consider the case $J \geq 3$, equation (A.12) with $H_J = J/2$. In order to express the radial force as a Fourier series, first rewrite it as

$$f(\theta) = -\frac{\kappa}{2\pi a}\Big(\frac{1}{\tau^2 - \frac{J}{2}}\Big)\sum_{n=-\infty}^{\infty}\sum_{j=1}^{J} w(\theta_j)\mathrm{e}^{in(\theta-\theta_j)}\left[\tau^2 - \frac{J}{2} + \sum_{m=1}^{J}\cos(\theta_j - \theta_m)\mathrm{e}^{in(\theta_j-\theta_m)}\right]. \tag{A.15}$$

Hence, referring to (3.29),

$$f_n = -\frac{\kappa}{2\pi a}\Big(\frac{1}{\tau^2 - \frac{J}{2}}\Big)\sum_{j=1}^{J} w(\theta_j)\mathrm{e}^{-in\theta_j}\left[\tau^2 - \frac{J}{2} + \sum_{m=1}^{J}\cos(\theta_m - \theta_j)\mathrm{e}^{-in(\theta_m-\theta_j)}\right]. \tag{A.16}$$

Consider first the term

$$\sum_{j=1}^{J} w(\theta_j)\mathrm{e}^{in\theta_j} = \sum_{m=-\infty}^{\infty} W_m \sum_{j=1}^{J}\mathrm{e}^{i(m-n)\theta_j} = \sum_{m=-\infty}^{\infty} W_m \hat{S}_{m-n}, \tag{A.17}$$

where

$$\hat{S}_p = \sum_{j=1}^{J}\mathrm{e}^{ip\theta_j} = \sum_{j=1}^{J}\mathrm{e}^{ij\theta_p}. \tag{A.18}$$

For $p = 0 \bmod J$, $p \in \mathbb{Z}$, we have $\mathrm{e}^{i\theta_p} = 1$ and hence $\hat{S}_p = J$. Otherwise $\mathrm{e}^{i\theta_p} \neq 1$ and therefore $\hat{S}_p = (\mathrm{e}^{iJ\theta_p} - 1)/(1 - \mathrm{e}^{-i\theta_p}) = 0$. In conclusion,

$$\sum_{j=1}^{J} w(\theta_j)\mathrm{e}^{-in\theta_j} = J\sum_{m=-\infty}^{\infty} W_{n+mJ}. \tag{A.19}$$

The modal force in (A.15) contains the summation

$$2\sum_{m=1}^{J}\cos(\theta_m-\theta_j)\mathrm{e}^{-in(\theta_m-\theta_j)}=2\sum_{m=1}^{J}\cos\theta_m\mathrm{e}^{-in\theta_m}=\hat{S}_{1-n}+\hat{S}_{1+n}, \tag{A.20}$$

see (A.18). Thus

$$\sum_{m=1}^{J}\cos(\theta_m-\theta_j)\mathrm{e}^{-in(\theta_m-\theta_j)}=\begin{cases}\frac{J}{2}, & n=\pm1 \bmod J,\\ 0, & \text{otherwise,}\end{cases} \tag{A.21}$$

where the notation $n=\pm1 \bmod J$ is defined in equation (3.25).

Substituting results (A.19) and (A.21) into equation (A.15) yields the modal force on the shell for $J\geq 3$ springs as

$$f_n=-\frac{J\kappa}{2\pi a}\sum_{m=-\infty}^{\infty}W_{n+mJ}\times\begin{cases}\frac{\tau^2}{\tau^2-\frac{J}{2}}, & n=\pm1 \bmod J,\\ 1, & \text{otherwise.}\end{cases} \tag{A.22}$$

Appendix B

Deformation gradient $\boldsymbol{F}$ in cylindrical coordinates

The radial position of a particle in the deformed and undeformed coordinate systems is, respectively,

$$\begin{aligned} \vec{X} &= R\vec{e_r}, \\ \vec{x} &= r\vec{e_r}. \end{aligned} \tag{B.1}$$

The angular position variable, θ, remains the same in magnitude and direction as seen from both frames of reference. Solving the above equations for $\vec{e_r}$ and combining yields

$$\vec{x} = \frac{r}{R}\vec{X}. \tag{B.2}$$

The deformation gradient is defined as $\boldsymbol{F} = \frac{\partial \boldsymbol{x}}{\partial \boldsymbol{X}} = \frac{\partial x_i}{\partial X_j}\vec{e_i}\vec{e_j}$. Applying to equation (B.2) yields

$$\frac{\partial x_i}{\partial X_j} = \frac{r}{R}\delta_{ij} + X_i\frac{\partial(\frac{r}{R})}{\partial X_j}. \tag{B.3}$$

Using the chain rule the last term can be rewritten as

$$X_i\frac{\partial(\frac{r}{R})}{\partial X_j} = X_i\frac{\partial R}{\partial X_j}\frac{1}{R}\left(\frac{\partial r}{\partial R} - \frac{r}{R}\right). \tag{B.4}$$

To determine $\frac{\partial R}{\partial X_j}$ we can simply differentiate the inner product of $\vec{\boldsymbol{X}}$ with itself.

$$\begin{aligned} \vec{\boldsymbol{X}}\cdot\vec{\boldsymbol{X}} &= X_jX_j = R^2, \\ \frac{\partial}{\partial X_j}(\vec{\boldsymbol{X}}\cdot\vec{\boldsymbol{X}}) &= 2X_j = 2R\frac{\partial R}{\partial X_j}, \\ \frac{\partial R}{\partial X_j} &= \frac{1}{R}X_j. \end{aligned} \tag{B.5}$$

Substituting this result into equation (B.3) gives

$$F_{ij} = \frac{r}{R}\delta_{ij} + X_iX_j\frac{1}{R^2}\left(\frac{\partial r}{\partial R} - \frac{r}{R}\right). \tag{B.6}$$

Here we need to note that the components of X_i are

$$X_i = \begin{cases} R & i = 1 \\ 0 & i = \text{else.} \end{cases} \tag{B.7}$$

and therefore the deformation tensor $\boldsymbol{F}$ becomes

$$\boldsymbol{F} = \frac{\partial r}{\partial R}\vec{e_r}\vec{e_r} + \frac{r}{R}\vec{e_\theta}\vec{e_\theta}. \tag{B.8}$$

References

[1] M. Abramowitz and I. Stegun. *Handbook of Mathematical Functions with Formulas, Graphs, and Mathematical Tables*. Dover, New York, 1974.

[2] J. D. Achenbach, J. Bjarnason, and T. Igusa. Effect of a vibrating substructure on acoustic radiation from a cylindrical shell. *J. Vib. Acoust.*, 114(3):312–318, 1992.

[3] A. Baillard, J.-M. Conoir, D. Décultot, G. Maze, A. Klauson, and J. Metsaveer. Acoustic scattering from fluid-loaded stiffened cylindrical shell: Analysis using elasticity theory. *J. Acoust. Soc. Am.*, 107(6):3208–3216, 2000.

[4] J. Bjarnason, J. D. Achenbach, and T. Igusa. Acoustic radiation from a cylindrical shell with an internal plate. *Wave Motion*, 15:23–41, 1992.

[5] J. Bjarnason, T. Igusa, S.-H. Choi, and J. D. Achenbach. The effect of substructures on the acoustic radiation from axisymmetric shells of finite length. *J. Acoust. Soc. Am.*, 96(1):246–255, 1994.

[6] H. H. Bleich and M. L. Baron. Free and forced vibration of an infinitely long cylindrical shell in an infinite acoustic medium. *ASME J. of Appl. Mech.*, 21:167–177, 1954.

[7] M. Botey, Y.-C. Cheng, V. Romero-Garcia, R. Picó, R. Herrero, V. Sánchez-Morcillo, and K. Staliunas. Unlocked evanescent waves in periodic structures. *Opt. Lett.*, 38(11):1890, 2013.

[8] C. E. Bradley. Acoustic bloch wave propagation in a periodic waveguide. Technical report, Technical Report of Applied Research Laboratories, Report No. ARL-TR-91-19, The University of Texas at Austin, 1991.

[9] L. Brillouin. *Wave Propagation in Periodic Structures*. Dover, New York, 1953.

[10] J. A. Bucaro, A. J. Romano, A. Sarkissian, D. M. Photiadis, and B. H. Houston. Local admittance model for acoustic scattering form a cylindrical shell with many internal oscillators. *J. Acoust. Soc. Am.*, 103(4):1867–1873, 1998.

[11] L.-W. Cai, D. K. Dacol, D. C. Calvo, and G. J. Orris. Acoustical scattering by arrays of cylinders in waveguides. *J. Acoust. Soc. Am.*, 122(3):1340–1351, 2007.

[12] H. Chen and C. T. Chan. Acoustic cloaking in three dimensions using acoustic metamaterials. *Appl. Phys. Lett.*, 91(18):183518+, 2007.

[13] Y. Chen and Z. Ye. Acoustic attenuation by two-dimensional arrays of rigid cylinders. *Phys. Rev. Lett.*, 87(18):184301, 2001.

[14] Z.-G. Chen, X. Ni, Y. Wu, C. He, X.-C. Sun, L.-Y. Zheng, M.-H. Lu, and Y.-F. Chen. Accidental degeneracy of double dirac cones in a phononic crystal. *Sci. Rep.*, 4:4613, 2014.

[15] A. Climente, D. Torrent, and J. Sánchez-Dehesa. Sound focusing by gradient index sonic lenses. *Appl. Phys. Lett.*, 97:104103, 2010.

[16] G. Coupry and C. Soize. Hydroelasticity and the field radiated by a slender elastic body into an unbounded fluid. *J. Sound. Vib.*, 96(2):261–273, 1984.

[17] S. A. Cummer and D. Schurig. One path to acoustic cloaking. *New J. Phys.*, 9(3):45+, 2007.

[18] J. M. Cuschieri and D. Feit. Acoustic scattering from fluid-loaded cylindrical shell with discontinuities: Double plate bulkhead. *J. Acoust. Soc. Am.*, 98(1):339–352, 1995.

[19] J. M. Cuschieri and D. Feit. Acoustic scattering from fluid-loaded cylindrical shell with discontinuities: Single plate bulkhead. *J. Acoust. Soc. Am.*, 98(1):320–338, 1995.

[20] M. El-Raheb and P. Wagner. Acoustic radiation from a shell with internal structures. *J. Acoust. Soc. Am.*, 85(6):2452–2460, 1989.

[21] U. Fano. Effects of configuration interaction on intensities and phase shifts. *Phys. Rev.*, 124(6):1866–1878, Dec 1961.

[22] X. H. Fengming Liu and C. T. Chan. Dirac cones at k=0 in acoustic crystals and zero refractive index acoustic materials. *Appl. Phys. Lett.*, 100:071911, 2012.

[23] X. H. Fengming Liu, Yun Lai and C. T. Chan. Dirac cones at k=0 in phononic crystals. *Phys. Rev. B*, 84:224113, 2011.

[24] K. Forsberg. A review of analytical methods used to determine the modal characteristics of cylindrical shells. Technical report, NASA Contract Report 613, 1966.

[25] K. C. Galloway, J. E. Clark, and D. E. Koditschek. Variable stiffness legs for robust, efficient, and stable dynamic running. *J. Mechanisms Robotics*, 5(1):011009, 2013.

[26] Z. Gao, J. Fang, Y. Zhang, and L. Jiang. Band structure research of a 2d honeycomb lattice phononic crystal. *Int. J. Electrochem. Sci.*, 8:7918–7925, 2013.

[27] G. C. Gaunaurd, H. Huang, and W. Wertman. Acoustic scattering by elastic spherical shells that have multiple massive internal components attached by compliant mounts. *J. Acoust. Soc. Am.*, 94(5):2924–2935, 1993.

[28] C. Goffaux and J. Sánchez-Dehesa. Two-dimensional phononic crystals studied using a variational method: Application to lattices of locally resonant materials. *Phys. Rev. B*, 72(9):099903, 2003.

[29] C. Goffaux, J. Sánchez-Dehesa, A. L. Yeyati, P. Lambin, A. Khelif, J. O. Vasseur, and B. Djafari-Rouhani. Evidence of fano-like interference phenomena in locally resonant materials. *Phys. Rev. Lett.*, 88(22):225502, 2002.

[30] C. Goffaux and J. P. Vigneron. Theoretical study of a tunable phononic band gap system. *Phys. Rev. B*, 64(7):075118, 2001.

[31] M. D. Guild, A. Alù, and M. R. Haberman. Cloaking of an acoustic sensor using scattering cancellation. *Appl. Phys. Lett.*, 105(2):023510+, July 2014.

[32] M. D. Guild, M. R. Haberman, and A. Alù. Plasmonic-type acoustic cloak made of a bilaminate shell. *Phys. Rev. B*, 86(10):104302+, Sept. 2012.

[33] Y. P. Guo. Sound scattering from an internally loaded cylindrical shell. *J. Acoust. Soc. Am.*, 91(2):926–938, 1992.

[34] Y. P. Guo. Sound scattering from cylindrical shells with internal elastic plates. *J. Acoust. Soc. Am.*, 93(4):1936–1946, 1993.

[35] Y. P. Guo. Sound scattering by bulkheads in cylindrical shells. *J. Acoust. Soc. Am.*, 95(5):2550–2559, 1994.

[36] Y. P. Guo. Acoustic scattering from cylindrical shells with deck-type internal plate at oblique incidence. *J. Acoust. Soc. Am.*, 99(5):13, 1996.

[37] M. R. Haberman, M. D. Guild, and A. Alù. Acoustic cloaking with plasmonic shells. In R. V. Craster and S. Guenneau, editors, *Acoustic Metamaterials*, volume 166 of *Springer Series in Materials Science*, pages 241–265. Springer, 2013.

[38] M. A. Heckl and L. S. Mulholland. Some recent developments in the theory of acoustic transmission in tube bundles. *J. Sound. Vib.*, 179(1):37–62, 1995.

[39] J. M. Ho. Structural and acoustic response of mass-spring loaded cylindrical shells: Spectral formulation and ray synthesis. *J. Acoust. Soc. Am.*, 99(2):659–671, 1996.

[40] G. H. Houston, J. A. Bucaro, and D. M. Photiadis. Broadband acoustic scattering from a ribbed shell. *J. Acoust. Soc. Am.*, 95(5):2785–2790, 1994.

[41] F.-L. Hsiao, A. Khelif, H. Moubchir, A. Choujaa, C.-C. Chen, and V. Laude. Complete band gaps and deaf bands of triangular and honeycomb water-steel phononic crystals. *J. Appl. Phys.*, 101(4):044903, 2007.

[42] M. I. Hussein, M. J. Leamy, and M. Ruzzene. Dynamics of Phononic Materials and Structures: Historical Origins, Recent Progress, and Future Outlook. *Appl. Mech. Rev.*, 66(4):040802+, 2014.

[43] S. John. Strong localization of photons in certain disordered dielectric superlattices. *Phys. Rev. Lett.*, 58(23):2486–2489, Jun 1987.

[44] M. C. Junger and D. Feit. *Sound, Structures, and Their Interaction.* MIT Press, Cambridge, MA, 1986.

[45] A. Khelif, P. A. Deymier, B. Djafari-Rouhani, J. O. Vasseur, and L. Dobrzynski. Two-dimensional phononic crystal with tunable narrow pass band: Application to a waveguide with selective frequency. *J. Appl. Phys.*, 94(3):1308, 2003.

[46] A. Klauson, G. Maze, and J. Metsaveer. Acoustic scattering by a submerged cylindrical shell stiffened by an internal lengthwise rib. *J. Acoust. Soc. Am.*, 96(3):1575–1581, 1994.

[47] A. Klauson and J. Metsaveer. Sound scattering by a cylindrical shell reinforced by lengthwise ribs and walls. *J. Acoust. Soc. Am.*, 91(4):1834–1843, 1992.

[48] Y. Kosevich, C. Goffaux, and J. Sánchez-Dehesa. Fano-like resonance phenomena by flexural shell modes in sound transmission through two-dimensional periodic arrays of thin-walled hollow cylinders. *Phys. Rev. B*, 74(1), Jul 2006.

[49] A. Krynkin, O. Umnova, A. Y. B. Chong, S. Taherzadeh, and K. Attenborough. Predictions and measurements of sound transmission through a periodic array of elastic shells in air. *J. Acoust. Soc. Am.*, 128(6):34963506, 2010.

[50] A. Krynkin, O. Umnova, S. Taherzadeh, and K. Attenborough. Analytical approximations for low frequency band gaps in periodic arrays of elastic shells. *J. Acoust. Soc. Am.*, 133:781–791, 2013.

[51] L. D. Landau and E. M. Lifshitz. *Theory of Elasticity*. Pergamon Press, 1970.

[52] V. Laude, R. P. Moiseyenko, S. Benchabane, and N. F. Declercq. Bloch wave deafness and modal conversion at a phononic crystal boundary. *AIP Adv.*, 1(4):041402, 2011.

[53] C. N. Layman, T. P. Martin, K. M. Moore, D. C. Calvo, and G. J. Orris. Designing acoustic transformation devices using fluid homogenization of an elastic substructure. *Appl. Phys. Lett.*, 99:163503+, 2011.

[54] A. Leissa. *Vibration of Shells*. ASA, Woodbury, NY, 1993.

[55] U. Leonhardt. Optical conformal mapping. *Science*, 312(5781):1777–1780, June 2006.

[56] S. Lethuillier, J. M. Conoir, P. Pareige, and J. L. Izbicki. Resonant acoustic scattering by a finite linear grating of elastic shells. *Ultrasonics*, 41:655–662, 2003.

[57] J. Li and J. B. Pendry. Hiding under the carpet: A new strategy for cloaking. *Phys. Rev. Lett.*, 101(20):203901+, 2008.

[58] S.-C. S. Lin, T. J. Huang, J.-H. Sun, and T.-T. Wu. Gradient-index phononic crystals. *Phys. Rev. B*, 79:094302, 2009.

[59] S.-C. S. Lin, B. R. Tittmann, and T. J. Huang. Design of acoustic beam aperture modifier using gradient-index phononic. *J. Appl. Phys.*, 111:123510, 2012.

[60] S.-C. S. Lin, B. R. Tittmann, J.-H. Sun, T.-T. Wu, and T. J. Huang. Acoustic beamwidth compressor using gradient-index phononic crystals. *J. Phys. D: Appl. Phys*, 42:185502, 2009.

[61] Y. T. Liu and K. S. Thorne. Thermoelastic noise and homogeneous thermal noise in finite sized gravitational-wavetest masses. *Phys. Rev. D*, 62:122002, 2000.

[62] R. C. Loftman and D. B. Bliss. Scattering from fluid-loaded cylindrical shell with periodic circumferential constraints using analytical/numerical matching. *J. Acoust. Soc. Am.*, 106(3):1271–1283, 1999.

[63] A. Martin, M. Kadic, R. Schittny, T. Bückmann, and M. Wegener. Phonon band structures of three-dimensional pentamode metamaterials. *Phys. Rev. B*, 86:155116+, 2012.

[64] P. A. Martin. *Multiple Scattering: Interaction of Time-harmonic Waves with N Obstacles*. Cambridge University Press, New York, 2006.

[65] T. P. Martin, C. N. Layman, K. M. Moore, and G. J. Orris. Elastic shells with high-contrast material properties as acoustic metamaterial components. *Phys. Rev. B*, 85(16):161103+, 2012.

[66] G. W. Milton, M. Briane, and J. R. Willis. On cloaking for elasticity and physical equations with a transformation invariant form. *New J. Phys.*, 8:248–267, 2006.

[67] G. W. Milton and A. V. Cherkaev. Which elasticity tensors are realizable? *J. Eng. Mat. Tech.*, 117(4):483–493, 1995.

[68] T. Miyashita. Sonic crystals and sonic wave-guides. *Meas. Sci. Technol.*, 16:R47–R63, 2005.

[69] M.Rahm, S. A. Cummer, D. Schurig, J. B. Pendry, and D. R. Smith. Optical design of reflectionless complex media by finite embedded coordinate transformations. *Phys. Rev. Lett.*, 100:063903, 2008.

[70] A. N. Norris. Acoustic cloaking theory. *Proc. R. Soc. A*, 464:2411–2434, 2008.

[71] A. N. Norris. Acoustic metafluids. *J. Acoust. Soc. Am.*, 125(2):839–849, 2009.

[72] A. N. Norris. Comment on "Design of acoustic devices with isotropic material via conformal transformation" [Appl. Phys. Lett. 97, 044101 (2010)]. *Appl. Phys. Lett.*, 100:066101, 2012.

[73] A. N. Norris and A. J. Nagy. Acoustic metafluids made from three acoustic fluids. *J. Acoust. Soc. Am.*, 128(4):1606–1616, 2010.

[74] A. N. Norris and D. A. Rebinsky. Acoustic coupling to membrane waves on elastic shells. *J. Acoust. Soc. Am.*, 95:1809–1829, 1994.

[75] J. B. Pendry, D. Schurig, and D. R. Smith. Controlling electromagnetic fields. *Science*, 312(5781):1780–1782, 2006.

[76] Y. Pennec, B. Djafari-Rouhani, J. Vasseur, A. Khelif, and P. Deymier. Tunable filtering and demultiplexing in phononic crystals with hollow cylinders. *Phys. Rev. E*, 69(4), Apr 2004.

[77] D. M. Photiadis, J. A. Bucaro, and B. H. Houston. The effect of internal oscillators on the acoustic response of a submerged shell. *J. Acoust. Soc. Am.*, 101(2):895–899, 1997.

[78] D. M. Photiadis, J. A. Bucaro, and G. H. Houston. Scattering from flexural waves on a ribbed cylindrical shell. *J. Acoust. Soc. Am.*, 95(5):2785–2790, 1994.

[79] D. M. Photiadis, B. H. Houston, E. G. Williams, and J. A. Bucaro. Resonant response of complex shell structures. *J. Acoust. Soc. Am.*, 108(3):1027–1035, 2000.

[80] A. D. Pierce, V. W. Sparrow, and D. A. Russell. Fundamental structural-acoustic idealizations for structures with fuzzy internals. *J. Vib. Acoust.*, 117(3A):339–348, 1995.

[81] B.-I. Popa and S. A. Cummer. Homogeneous and compact acoustic ground cloaks. *Phys. Rev. B*, 83(22):224304+, Jun 2011.

[82] B. I. Popa, L. Zigoneanu, and S. A. Cummer. Experimental acoustic ground cloak in air. *Phys. Rev. Lett.*, 106:253901+, 2011.

[83] Y. C. Qi Wei and X. jun Liu. Acoustic total transmission and total reflection in zero-index metamaterials with defects. *Appl. Phys. Lett.*, 102:174104, 2013.

[84] A. M. Rao, E. Richter, S. Bandow, B. Chase, P. C. Eklund, K. A. Williams, S. Fang, K. R. Subbaswamy, M. Menon, A. Thess, R. E. Smalley, G. Dresselhaus, and M. S. Dresselhaus. Diameter-selective raman scattering from vibrational modes in carbon nanotubes. *Science*, 275(5297):187–191, 1997.

[85] V. Romero-Garciá, L. M. Garcia-Raffi, and J. V. Sánchez-Pérez. Evanescent waves and deaf bands in sonic crystals. *AIP Adv.*, 1(4):041601, 2011.

[86] V. Romero-Garcia, C. Lagarrigue, J.-P. Groby, O. Richoux, and V. Tournat. Tunable acoustic waveguides in periodic arrays made of rigid square-rod scatterers: theory and experimental ealization. *J. Phys. D: Appl. Phys.*, 46:305108, 2013.

[87] V. Romero-Garciá, J. O. Vasseur, L. M. Garcia-Raffi, and A.-C. Hladky-Hennion. Theoretical and experimental evidence of level repulsion states and evanescent modes in sonic crystal stubbed waveguides. *New J. Phys.*, 14(2):023049, Feb 2012.

[88] M. L. Rumerman. Contribution of membrane wave reradiation to scattering from finite cylindrical steel shells in water. *J. Acoust. Soc. Am.*, 93(1):55–65, 1993.

[89] J. Sánchez-Pérez, D. Caballero, R. Mártinez-Sala, C. Rubio, J. Sánchez-Dehesa, F. Meseguer, J. Llinares, and F. Gálvez. Sound attenuation by a two-dimensional array of rigid cylinders. *Phys. Rev. Lett.*, 80(24):5325–5328, Jun 1998.

[90] D. Schurig, J. J. Mock, B. J. Justice, S. A. Cummer, J. B. Pendry, A. F. Starr, and D. R. Smith. Metamaterial electromagnetic cloak at microwave frequencies. *Science*, 314(5801):977–980, 2006.

[91] J. F. M. Scott. The free modes of propagation of an infinite fluid-loaded thin cylindrical shell. *J. Sound. Vib.*, 125(2):41–280, 1988.

[92] E. A. Skelton. Acoustic scattering by a disc constraining an infinite fluid-loaded cylindrical shell. *J. Sound. Vib.*, 148(2):243–264, 1991.

[93] I. Sliwa and M. Krawczyk. Phononic band gap width control through structural and material parameters in two-dimensional phononic crystals. *Acta. Phys. Pol. A*, 108(6):943–957, 2005.

[94] J. Smith and P. Verrier. The effect of shear on acoustic cloaking. *Proc. R. Soc. A*, 467(2132):2291–2309, 2011.

[95] S. G. L. Smith and A. M. J. Davis. The split ring resonator. *Proc. R. Soc. A*, 466:3117–3134, 2010.

[96] S. Sodagar, F. Honarvar, and A. N. Sinclair. Multiple scattering of an obliquely incident plane acoustic wave from a grating of immersed cylindrical shells. *Applied Acoustics*, 72:1–10, 2011.

[97] R. Solecki and R. J. Conant. *Advanced Mechanics of Materials*. New York: Oxford University Press, 2003.

[98] A. Spadoni and C. Daraio. Generation and control of sound bullets with a nonlinear acoustic lens. *Proc. Nat. Acad. Sci.*, 107(16):7230–7234, 2010.

[99] M. Strasberg and D. Feit. Vibration damping of large structures induced by attached small resonant structures. *J. Acoust. Soc. Am.*, 99(1):335–344, 1996.

[100] A. S. Titovich and A. N. Norris. Green's function for symmetric loading of an elastic sphere with application to contact problems. *J. Mech. Mater. Struct.*, 7(7):701–719, 2012.

[101] A. S. Titovich and A. N. Norris. Tunable cylindrical shell as an element in acoustic metamaterial. *J. Acoust. Soc. Am.*, 136(4):1601–1609, Oct 2014.

[102] A. S. Titovich and A. N. Norris. Acoustic scattering from a cylindrical shell with an internal mass attached by multiple springs. *J. Sound. Vib.*, 228:134–153, March 2015.

[103] D. Torrent, A. Håkansson, F. Cervera, and J. Sánchez-Dehesa. Homogenization of two-dimensional clusters of rigid rods in air. *Phys. Rev. Lett.*, 96:204302, 2006.

[104] D. Torrent and J. Sánchez-Dehesa. Acoustic metamaterials for new two-dimensional sonic devices. *New J. Phys.*, 9(9):323+, September 2007.

[105] D. Torrent and J. Sánchez-Dehesa. Acoustic cloaking in two dimensions: a feasible approach. *New J. Phys.*, 10(6):063015+, 2008.

[106] M. Tran-Van-Nhieu. Scattering from a ribbed finite cylindrical shell. *J. Acoust. Soc. Am.*, 110(6):2858–2866, 2001.

[107] M. Tran-Van-Nhieu. Scattering from a ribbed finite cylindrical shell with internal axisymmetric oscillators. *J. Acoust. Soc. Am.*, 112(2):2, 2002.

[108] Y. Urzhumov, F. Ghezzo, J. Hunt, and D. R. Smith. Acoustic cloaking transformations from attainable material properties. *New J. Phys.*, 12(7):073014, Jul 2010.

[109] J. Valentine, J. Li, T. Zentgraf, G. Bartal, and X. Zhang. An optical cloak made of dielectrics. *Nature Mater.*, 8(7):568–571, April 2009.

[110] Z. Wang, F. Yang, L. Liu, M. Kang, and F. Liu. Total transmission and total reflection of acoustic wave by zero index metamaterials loaded with general solid defects. *J. Appl. Phys.*, 114:194502, 2013.

[111] E. Yablonovitch. Inhibited spontaneous emission in solid-state physics and electronics. *Phys. Rev. Lett.*, 58(20):2059–2062, May 1987.

[112] K.-P. Yu, T.-N. Chen, X.-P. Wang, and A.-A. Zhou. Large band gaps in two-dimensional phononic crystal composed of periodic cross-boards in air. *Phys. Scr*, 86:045402, 2012.

[113] L.-Y. Zheng, Y. Wu, X. Ni, Z.-G. Chen, M.-H. Lu, and Y.-F. Chen. Acoustic cloaking by a near-zero-index phononic crystal. *Appl. Phys. Lett.*, 104:161904, 2014.

[114] L. Zigoneanu, B.-I. Popa, and S. A. Cummer. Three-dimensional broadband omnidirectional acoustic ground cloak. *Nature Mater.*, 13(4):352–355, Mar 2014.